Ultraviolet Light Emitting Diodes and Bio-Aerosol Sensing

by

Kristina M. Davitt

B. Sc. Queen's University, 2001

Sc. M. Brown University, 2004

A dissertation submitted in partial fulfillment of the

requirements for the degree of Doctor of Philosophy in the

Division of Engineering at Brown University

PROVIDENCE, RHODE ISLAND

May 2006

This dissertation by Kristina May Davitt is accepted in its present form

by the Division of Engineering as satisfying the

dissertation requirement for the degree of Doctor of Philosophy.

Date _____ _____

Professor Arto V. Nurmikko, Advisor

Recommended to the Graduate Council

Date _____ _____

Professor Gregory P. Crawford, Reader

Date _____ _____

Professor Alexander Zaslavsky, Reader

Approved by the Graduate Council

Date _____ _____

Sheila Bonde, Dean of the Graduate School

VITA

Kristina May Davitt was born in Hawkesbury, Canada on July 18th 1978. She received her B.Sc., first class honors, in Engineering Physics from Queen's University, Kingston, Canada in 2001, and subsequently began her studies at Brown University with a fellowship from the Division of Engineering. Since 2002 she has been supported by a research assistantship, and in 2004 she received an Sc.M. in Electrical Engineering. A list of her scientific publications is given below.

Peer-Reviewed Publications

Spectroscopic Sorting of Aerosols by a Compact Sensor Employing UV LEDs
K. Davitt, Y-K. Song, W. R. Patterson III, A.V. Nurmikko, Y-L. Pan, R. K. Chang, J. Han, M. Gherasimova, P. J. Cobler, P. D. Butler, and V. Palermo, in preparation (2006)

290 and 340nm UV LED arrays for fluorescence detection from single airborne particles
K. Davitt, Y-K. Song, A.V. Nurmikko, M. Gherasimova, J. Han, Y-L. Pan, and R.K. Chang, Opt. Exp. **13**(23) p. 9548-9555 (2005)

Compact Semiconductor Light-Emitting Diodes for Dynamic Imaging of Neuronal Circuitry
S. Venkataramani, K. Davitt, J. Zhang, H. Xu, Y-K. Song, B. Connors, and A.V. Nurmikko, J. Selected Topics in Quantum Electronics **11**(4) p. 785-790 (2005)

UV LED arrays for spectroscopic fingerprinting of airborne biological particles
K. Davitt, Y-K. Song, A.V. Nurmikko, S-R. Jeon, M. Gherasimova, J. Han, Y-L. Pan, and R.K. Chang, Phys. Stat. Sol.(c) **2**(7) p. 2878-2881 (2005)

Application of light-emitting diodes for aerosol fluorescence detection
Y-L. Pan, V. Boutou, R.K. Chang, I. Ozden, K. Davitt, and A.V. Nurmikko, Opt. Lett. **28**(18) p. 1707-1709 (2003)

Stability of angular confinement and rotational acceleration of a diatomic molecule in an optical centrifuge
M. Spanner, K. Davitt, M. Ivanov, J. Chem. Phys., **115**(18) p. 8403 (2001)

ACKNOWLEDGEMENTS

I would like to extend my sincere gratitude to Professor Arto Nurmikko whose guidance and encouragement throughout my stay at Brown I have greatly valued – *monet kiitokset*. My thanks also goes to Professor Crawford and Professor Zaslavsky for their support and particularly for taking the time to read this composition.

The device work presented here was done in close cooperation with Prof. J. Han and his group at Yale University, who are credited with all of the nitride epitaxy, and the team of Drs. L. Zhou, W. Goetz and M. Krames at Lumileds LLC. Prof. R. K. Chang and Dr. Y.-L. Pan, also at Yale, have been invaluable mentors in the field of bio-aerosol sensing. These collaborations have all been supported under the DARPA SUVOS program.

At Brown, Bill Patterson and Michael Jibitsky have kindly given me technical help and a great deal of their time, which has not gone unappreciated. Particular recognition must be extended to Dr. Y.-K. Song whose keen scientific interest and limitless patience I have great respect for, and have taken much advantage of. Many thanks to the entire *Nurmikko Group*, you have been the highlight of my experience here. To my friends Sowmya Venkataramani and Yanqiu Li, I adore your excitement for life and new experience.

For my family who is always behind me, thank you for everything. Last, but not least, my dear Andrew, who has laughed with me and cooked for me throughout it all.

For Mummo

TABLE OF CONTENTS

LIST OF TABLES

LIST OF FIGURES

CHAPTER 1

INTRODUCTION

The gallium nitride material system has recently been a subject of considerable research interest with the aim of creating compact ultraviolet optical sources. This wide bandgap semiconductor family yielded high performance visible light emitters in the mid-1990's which have been rapidly commercialized for use in optical data storage. Pushing this system into the ultraviolet (UV) capitalizes on advances in material quality and device fabrication technique made at longer wavelengths and widens the spectrum of potential applications. In the wake of 2001, particular attention has been paid to the development of compact UV sources to enable the design of portable warning systems for detecting the release of biological agents. Nitride-based UV emitters have surfaced in the research community within the timeframe of this thesis, and hence the study presented herein provides a recent chronology of the advancing field. The central theme of this work is the creation of useful instrumentation from emerging semiconductor sources, specifically the integration of early UV devices into a prototype bio-aerosol sensor.

Owing to the native fluorescent molecules present in hazardous bio-aerosols, desirable excitation wavelengths lie well into the UV portion of the spectrum at 340 nm and 280 nm. Achieving these wavelengths from the nitride system requires the use of high aluminum fraction films, a task that represents substantial challenge in epitaxial growth and device fabrication, and is at this stage limited to light emitting diode (LED) structures. **Chapter 2** offers a concise introduction to the difficulties encountered in material synthesis, with added emphasis on the

epitaxial substrate technology as a limiting factor in device performance. A brief survey of UV LED performance reported within the research community is intended to frame the device results presented in **Chapter 4**.

A description of the bio-aerosol detection problem is given in **Chapter 3**, along with the fundamental operational requirements of a warning sensor and reasoning behind the necessity for UV excitation. A flavor of existing laser-based systems is provided by way of a quick summary of notable literature. Following these introductory chapters, **Chapter 4** reports on material characterization and UV LED device performance achieved during this study. Microelectronic fabrication methods are detailed for the processing of test device structures, and preliminary results for a 300 nm LED grown on an alternative substrate, aluminum nitride (AlN), are presented.

In **Chapter 5**, the process of design and implementation of a bio-aerosol system based on arrays of UV LEDs is chronicled. This consists of assembling a packaged LED array, designing compact optics, and employing real-time electronics. In addition, a small particle deflector is integrated into the sensor and used to verify the performance of the entire system. A prototype operating with LED excitation wavelengths of 340 or 290 nm is demonstrated to have promising performance with simulated bio-aerosols. **Chapter 6** extends the optical design to enable the use of semiconductor laser diodes (LDs), and is demonstrated with a 380 nm device.

Although not employing UV wavelengths, the investigation of green LED arrays for dynamic recording from neural cells presented in **Appendix A** benefits from the device packaging and light extraction techniques developed for LED arrays earlier in this work. It also serves as an illustration of the wide application space for nitride LEDs and LED arrays.

CHAPTER 2

STATUS AND DEVELOPMENT OF ULTRAVIOLET LIGHT EMITTING DIODES

Traditional sources of ultraviolet (UV) light consist of solid state lasers and mercury-vapor lamps and more recently include semiconductor heterostructures. The wide bandgap semiconductor gallium nitride and its alloys, which yielded high quality blue light emitters in the last decade, are now being developed for UV light emitting diodes and laser diodes. This chapter provides a brief introduction to the nitride material system and enumerates key issues in the growth of high quality epitaxial films and fabrication of efficient light emitters encountered in later chapters. Particular emphasis is placed on 280 nm wavelength LEDs which have emerged from research laboratories within the past 4 years. The chapter concludes with a summary of published device performances intended to frame the results presented in **Chapter 4**.

2.1. Ultraviolet light

Near ultraviolet light is electromagnetic radiation with a wavelength between 200 and 380 nm. A common classification further divides the near UV by wavelength, denoted by UVA (315-380 nm), UVB (280-315 nm) and UVC (< 280 nm). Historically this division is largely based on the health and environmental affects of a particular photon energy, however, it may be similarly used to categorize the potential application space. We focus exclusively on light emission between 280 and 380 nm owing to its use in the field of bio-aerosol sensing as outlined in **Chapter 3**, and the recent, rapid development of light emitting diodes (LEDs) in this

wavelength. In addition to aerosol sensing, UV LEDs have applications in the study of protein folding, for sterilization (particularly in the so-called germicidal UVC range), as transmitters for short range solar-blind communication systems, and for white-light generation using wavelength conversion phosphor coatings.

2.2. The nitride system

The family of nitride materials consists of aluminum nitride (AlN), gallium nitride (GaN) and indium nitride (InN), and spans the bandgap (E_g) range from 6.2 eV down to 0.7 eV [1]. Thus, this alloy system has the potential to produce light emitters with wavelengths ranging from the infrared to the UV. Furthermore, as illustrated in **Figure 2.1**, the quaternary AlGaInN enables limited bandgap tuning independent of lattice constant. Although electroluminescence from GaN was first demonstrated in 1971 [2], it was not until the late 1980's when advances in p-type doping and defect reduction techniques led to rapid development of viable nitride devices. Light emitting diodes (LEDs) emitting in the blue were first demonstrated in the early 1990's, and blue laser diodes (LDs) pioneered by Nakamura at Nichia Corporation soon followed suit. LDs operating at wavelengths as low as 410 nm are now standard industry-wide commercial products; truly UV LDs operating at 370-380 nm are available from Nichia as evaluation samples, but still suffer from relatively short operating lifetimes [3]. UV LEDs at 340 nm and below are a much more recent advance and remain primarily research-grade devices at this time.

Nitride epitaxy with large aluminum fraction

In the UV, achieving efficient light emission at wavelengths of 340 nm and 280 nm are regarded as particular milestones. This reflects the need for a UV source in many bio-sensing applications at the absorption peaks of key bio-molecules, but also delineates a threshold of difficulty in current material synthesis. Optical devices at these wavelengths consist almost

entirely of the ternary $Al_xGa_{1-x}N$ with aluminum fractions reaching x = 0.65 for the shorter wavelength case. At 340 nm, a small fraction of indium ($Al_xGa_{1-x-y}In_yN$, y ~ 0.02 %) is used in the active region. At longer wavelengths still, an increasing amount of indium is used throughout the device structure. From the growth of high efficiency visible light emitters, indium is known to incorporate in clusters that suppress non-radiative recombination processes [4-6]. On the other hand, high aluminum fraction material poses difficulties in doping, formation of ohmic contacts and growth morphology. Thus, with a reduction in wavelength and the associated decrease in indium and increase in aluminum content, come significant obstacles in device growth and fabrication.

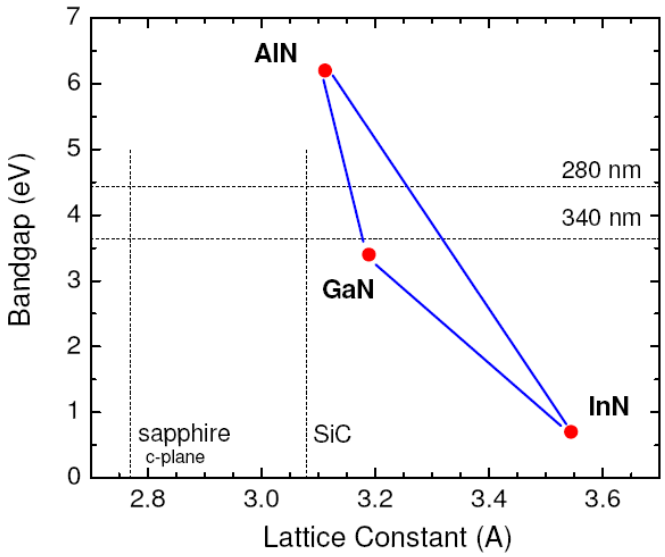

Figure 2.1 : Bandgap and lattice constant for III-V nitrides and common substrates.

Doping nitrides

The most common dopants for p and n-type nitrides are magnesium (Mg) and silicon (Si) respectively. Magnesium atoms are deep acceptors that have a well-documented ability to form complexes with hydrogen present in the growth chamber. Since the discovery that these acceptors could be re-activated [7], it has become a universal procedure to activate Mg-dopants

with a high temperature anneal immediately following epitaxial growth. Due to the high thermal activation energy, ~ 160 meV for GaN and larger for increasing aluminum fractions [8], hole concentrations are typically a small fraction of the dopant density. In addition, there exists a practical window of doping concentration between that required to offset the background of impurities in naturally n-type AlGaN, and below a limit where structural defects occur and material resistivity increases. Thus, hole concentrations in typical UV devices are on the order of 10^{17} cm^{-3} [9]. Silicon donors also exhibit a continuous increase in ionization energy with increasing Al-fraction and thus suffer similar limitations in carrier concentration [10].

Epitaxial substrates

One of the key issues in nitride semiconductor epitaxy in general has been, and remains, the substrate choice. Aluminum nitride (AlN), gallium nitride (GaN), sapphire (Al_2O_3), and silicon carbide (SiC) are potential candidates which are all under investigation. A selection of relevant properties is given in **Table 2.1** [11, 12]. The vast majority of UV emitters have been grown on one of the two latter options, neither of which is ideal; sapphire does not have the same wurtzite crystallographic symmetry as the epitaxial nitride, and although SiC has the advantage of being electrically conductive, it is opaque at wavelengths shorter than 360 nm. Furthermore, the significant lattice mismatch of both choices, illustrated in **Figure 2.1**, results in the growth of strained epi-layers. In spite of strain management and defect reduction techniques, UV devices on these substrates have typical dislocation densities in the range of 10^8 to 10^{10} cm^{-2} [13, 14]. Such exceedingly large dislocation densities are unheard of in more established material systems such as silicon or gallium arsenide. Perhaps due to the strong covalent bond in GaN, it is the only semiconductor material out of which optically active devices with reasonable performance have been made out of material with such large defect densities. Native nitride substrates, such as GaN or AlN, offer clear advantages in crystallographic symmetry, lattice and thermal expansion

matching, and thermal conductivity, but are not widely available. Growth of genuinely *bulk*, or equivalently *single-crystal*, GaN and AlN represents its own significant challenge in material science and is an active area of research. *Quasi*-bulk versions, which are themselves grown on a foreign substrate, are also available but involve a large amount of process overhead as they are produced by hydride vapor phase epitaxy (HVPE) or involve lithographic patterning for epitaxial lateral overgrowth (ELO). Another advantage of native substrates is their well defined cleavage planes which can simplify facet formation in UV laser diode development.

	energy gap (eV)	**lattice constant (Å)**	**refractive index**	**thermal conductivity (W/cm.°C)**	**thermal expansion (x 10^{-6} $°C^{-1}$ ∥ / ⊥)**
GaN	3.4	3.189	2.3	1.3	5.59 / 3.17
AlN	6.2	3.112	2.15	3.2	4.2 / 5.3
SiC	3 - 3.26	3.075	2.5	3 - 4	4.3 / 4.7
Al_2O_3	-	4.759	1.75	0.4	7.3 / 8.5

Table 2.1 : Properties of AlN, GaN, SiC and sapphire

Evaluated on transparency alone, sapphire and AlN are the leading candidates for the growth of high aluminum fraction UV light emitters. In this thesis, devices are grown on sapphire with the exception of results at the end of **Chapter 4** where we present an early investigation of research-grade bulk AlN and compare material and device performance between sub-300 nm LEDs grown on sapphire and bulk AlN.

2.3. Recent history of semiconductor ultraviolet light emitters

Early demonstrations of UV LEDs emitting at 350 nm appeared almost 10 years ago [15], and yet to date, practical electrically-injectable optical devices in the ultraviolet are still limited to wavelengths of 280 nm and above. By 2002, the growth and fabrication of nominally 340 nm LEDs had reached a measure of success and external quantum efficiencies in the range of 0.5 % to 1 % in continuous wave (CW) operation are now routinely achieved [16-18]. The external

quantum efficiency (EQE), defined by the number of emitted photons per number of injected electrons and written in terms of the light output power P_{out} at a particular applied current I,

$$EQE = \frac{eP_{out}}{I \cdot E_g},$$

provides a measure of the electrical to optical conversion which is relatively independent of device geometry and is thus a useful metric for comparison between research groups. The low EQE of current UV LEDs is linked to low internal quantum efficiencies, estimated to be below 10 %, which in turn reflects poor material quality. It is noted that the measured output power, and thus EQE, is highly dependent on current injection conditions (pulsed versus CW) and packaging of the device; for the sake of clarity, we attempt to quote unpackaged, CW results where available. The effect of a particular packaging scheme employed for UV LEDs and arrays of LEDs is examined in portions of **Chapters 4** and **5**. A useful rule of thumb is that the output power of a packaged LED is roughly 3-5 brighter than measured directly off the die.

Sub-300 nm LEDs

Sub-300 nm LEDs of some quality appeared in 2002 [19, 20]. These initial reports clearly showed electroluminescence at 280 nm attributed to carrier recombination in the MQW active region, but also suffered from considerable long-wavelength emission and had CW EQE on the order of 0.01 % [19]. The long-wavelength component around 330 nm has been attributed to radiative recombination of conduction band electrons and holes from Mg-related deep levels [21]. At low injection conditions the integrated output power from this component was as much as 10 times larger than the active region emission, but saturated with increasing current injection. The introduction of an electron blocking layer (EBL) to prevent high-energy electrons from overshooting the active layer and recombining in the high-Mg content p-layers has significantly reduced the long-wavelength '*tail*' and is now a standard feature in UV LEDs.

Two other features which have proved to be significant in the progress of sub-300 nm LEDs are current crowding effects and the creation of electrical contacts. Current crowding, due to the mismatch between lateral (n-type) and vertical (p-type) conductivities [22], was also observed during the development of 340 nm LEDs grown on non-conducting substrates like sapphire [23, 24]. The low conductivity of n-AlGaN, which decreases with increasing aluminum fraction, is particularly troublesome since mesa-etched devices are needed when growth is performed on non-conducting substrates and lateral current conduction across many (10-100s) microns in n-layers is required. This current-spreading problem manifests itself as non-uniform light emission from the optical aperture, and the high series resistance raises the junction temperature. To mitigate this, some groups have adopted an interdigitated finger geometry for n-contacts, or so-called micro-pixel arrangements of interconnected optical apertures [25]. Sub-optimal electrical contacts also contribute to heating, and together these problems require that suitable thermal management techniques are employed in order to lengthen device lifetime [26].

At the 280 nm wavelength, LEDs grown by Khan et al. at the University of South Carolina, and the associated commercial enterprise Sensor Electronic Technology, have shown superior device quality by all measures. Early in 2004, CW EQEs of 0.1 % or greater were achieved by a number of groups [27, 28], but late in that year a phenomenal 0.93 % was reported by the Khan et al. [29]. It is noted that this result is from a so-called *split mesa* device, where there are essentially four separate optical apertures, and it has been packaged for thermal management. The researchers attribute this leap in device performance to improvements in buffer, strain management, and EBL layers. This remains the best performance reported from 280 nm LEDs to date.

Optical devices grown on bulk AlN

A considerably different approach to the UV LED development chronicled above involves the use of native AlN substrates, which are scarcely available, but which are touted as superior candidates for UV LD development in particular. Single crystalline material can be grown by sublimation-recondensation, a high temperature (~ 2200 °C) technique pioneered by Slack et al. in the late 1970's where thermal gradients within a tungsten tube furnace are used to nucleate and grow boules of bulk AlN [30]. A small company based out of Rensselaer Polytechnic Institute, Crystal-IS, has continued to refine this method and subsequent surface preparations, and is the unique supplier of bulk AlN [31]. Aluminum nitride is a useful substrate for growth of a number of devices, including wide-bandgap RF electronics, but in terms of optical devices only a handful of reports have been published [32-34]. In [32] and [34], LEDs operating at 360 nm and 345 nm were described. The former served as a first demonstration of the feasibility of growing high quality optical devices on existing AlN. In the latter, the advantage of AlN is illustrated by a delayed thermal rollover in output power, however the absolute power is modest and shows no advantage over a reference device grown on sapphire. In [33], optical pumping of a MQW structure grown on AlN was used to demonstrate stimulated emission at 258 nm. This illustrates the potential of AlN to serve as a substrate for high quality epitaxial growth of UV LDs. In **Chapter 4** we report on a fully fabricated 300 nm LED grown on AlN emitting through the substrate, and compare its performance to state-of-the-art UV LEDs on sapphire.

In the next chapter, we deviate from the details of material growth and device fabrication and focus on the application of emerging UV light emitters towards a portable bio-aerosol sensor. We return to examine the performance of 340 and 280 nm LEDs in **Chapter 4**, before demonstrating their integration into an optical system for bio-sensing in **Chapter 5**.

References

1. V. Y. Davydov, A. A. Klochikhin, V. V. Emtsev, D. A. Kurdyukov, S. V. Ivanov, V. A. Vekshin, F. Bechstedt, J. Furthmuller, J. Aderhold, J. Graul, A. V. Mudryi, H. Harima, A. Hashimoto, A. Yamamoto and E.E. Haller. Phys. Stat. Sol. (b), 2002. **234**(3): p. 787-795.
2. J. I. Pankove, E. A. Miller, D. Richman and J. E. Berkeyheiser. J. Lumin., 1971. **4**: p. 63-66.
3. Nichia Corporation, *www.nichia.co.jp*.
4. E. S. Jeon, V. Kozlov, Y.-K. Song, A. Vertikov, M. Kuball, A. V. Nurmikko, H. Liu, C. Chen, R. S. Kern, C. P. Kuo and M. G. Craford. Appl. Phys. Lett., 1996. **69**(27): p. 4194-4196.
5. Y. Narukawa, S. Saijou, Y. Kawakami, S. Fujita, T. Mukai and S. Nakamura. Appl. Phys. Lett., 1999. **74**(4): p. 558-560.
6. S. F. Chichibu, K. Wada, J. Mullhauser, O. Brandt, K. H. Ploog, T. Mizutani, A. Setoguchi, R. Nakai, M. Sugiyama, H. Nakanishi, K. Korii, T. Deguchi, T. Sota and S. Nakamura. Appl. Phys. Lett., 2000. **76**(13): p. 1671-1673.
7. H. Amano, M. Kito, K. Hiramatsu and I. Akasaki. Jpn. J. Appl. Phys., 1989. **28**(12): p. L2112-2114.
8. M. A. Khan, M. Shatalov, H. P. Maruska, H. M. Wang and E. Kuokstis. Jpn. J. Appl. Phys., 2005. **44**(10): p. 7191-7206.
9. Z. Ren, S.-R. Jeon, M. Gherasimova, G. Cui, J. Han, H. Peng, Y. K. Song, A. V. Nurmikko, L. Zhou, W. Goetz, M. Krames and H.-K. Cho. Mater. Res. Soc. Symp. Proc., 2005. **831**: p. 21-26.
10. Y. Taniyasu, M. Kasu and N. Kobayashi. Appl. Phys. Lett., 2002. **81**(7): p. 1255-1257.
11. O. Ambacher. J. Phys. D: Appl. Phys., 1998. **31**: p. 2653-2710.

12. M. E. Levinshtein, S. L. Rumyantsev and M. S. Shur, *Properties of Advanced Semiconductor Materials*. 2001, New York: John Wiley & Sons, Inc.

13. M. Iwaya, S. Takanami, A. Miyazaki, T. Kawashima, K. Iida, S. Kamiyama, H. Amano and I. Akasaki. Phys. Stat. Sol. (a), 2003. **200**(1): p. 110-113.

14. Y. S. Park, K. H. Kim, J. J. Lee, H. S. Kim, T. W. Kang, H. X. Jiang and J. Y. Lin. Jpn. J. Appl. Phys., 2003. **42**(3): p. 1231-1232.

15. J. Han, M. H. Crawford, R. J. Shul, J. J. Figiel, M. Banas, L. Zhang, Y. K. Song, H. Zhou and A. V. Nurmikko. Appl. Phys. Lett., 1998. **73**(12): p. 1688-1690.

16. S.-R. Jeon, M. Gherasimova, Z. Ren, J. Su, G. Cui, J. Han, H. Peng, Y.-K. Song, A. V. Nurmikko, L. Zhou, W. Goetz and M. Krames. Jpn. J. Appl. Phys., 2004. **43**(11A): p. L1409-1412.

17. A. Chitnis, V. Adivarahan, J. P. Zhang, M. Shatalov, S. Wu, J. Yang, G. Simin, M. A. Khan, X. Hu, Q. Fareed, R. Gaska and M. S. Shur. Phys. Stat. Sol. (a), 2003. **200**(1): p. 99-101.

18. T. Nishida, N. Kobayashi and T. Ban. Appl. Phys. Lett., 2003. **82**(1): p. 1-3.

19. A. Yasan, R. McClintock, K. Mayes, S. R. Darvish, P. Kung and M. Razeghi. Appl. Phys. Lett., 2002. **81**(5): p. 801-802.

20. V. Adivarahan, J. Zhang, A. Chitnis, W. Shuai, J. Sun, R. Pachipulusu, M. Shatalov and M. A. Khan. Jpn. J. Appl. Phys., 2002. **41**: p. L435-436.

21. M. Shatalov, A. Chitnis, R. Pachipulusu, J. P. Zhang, V. Adivarahan, S. Wu, G. Simin, M. A. Khan, G. Tamulaitis, A. Sereika, I. Yilmaz, M. S. Shur and R. Gaska. Appl. Phys. Lett., 2003. **82**(2): p. 167-169.

22. E. F. Schubert, *Light-Emitting Diodes*. 2005, Cambridge: Cambridge University Press. p.131-135.

23. M. Shatalov, G. Simin, V. Adivarahan, A. Chitnis, S. Wu, R. Pachipulusu, V. Mandavilli, K. Simin, J. P. Zhang, J. W. Yang and M. A. Khan. Jpn. J. Appl. Phys., 2002. **41**(8): p. 5083-5087.

24. M. Gherasimova, J. Su, G. Cui, J. Han, H. Peng, E. Makarona, Y. He, Y.-K. Song and A. V. Nurmikko. Mat. Res. Soc. Symp. Proc., 2004. **798**: p. 17-22.

25. V. Adivarahan, S. Wu, W. H. Sun, V. Mandavilli, M. S. Shatalov, G. Simin, J. W. Yang, H. P. Maruska and M. A. Khan. Appl. Phys. Lett., 2004. **85**(10): p. 1838-1840.

26. M. Shatalov, A. Chitnis, P. Yadav, Md. F. Hasan, J. Khan, V. Adivarahan, H. P. Maruska, W. H. Sun and M. A. Khan. Appl. Phys. Lett., 2005. **86**(20): p. 201109.

27. K. Mayes, A. Yasan, R. McClintock, D. Shiell, S. R. Darvish, P. Kung and M. Razeghi. Appl. Phys. Lett., 2004. **84**(7): p. 1046-1048.

28. W. H. Sun, J. P. Zhang, V. Adivarahan, A. Chitnis, M. Shatalov, S. Wu, V. Mandavilli, J. W. Yang and M. A. Khan. Appl. Phys. Lett., 2004. **85**(4): p. 531-533.

29. W. Sun, V. Adivarahan, M. Shatalov, Y. Lee, S. Wu, J. Yang, J. Zhang and M. A. Khan. Jpn. J. Appl. Phys., 2004. **43**(11A): p. L1419-1421.

30. G. A. Slack and T. F. McNelly. J. Cryst. Growth, 1977. **42**: p. 560-563.

31. L. J. Schowalter, G. A. Slack, J. B. Whitlock, K. Morgan, S. B. Schujman, B. Raghothamachar, M. Dudley and K. R. Evans. Phys. Stat. Sol. (c), 2003. **0**(7): p. 1997-2000.

32. M. Kneissl et al., *Palo Alto Research Center (PARC) and Crystal IS demonstrate the first UV-LED on AlN substrates*. 2002, PARC press release *www.parc.xerox.com*.

33. R. Gaska, C. Chen, J. Yang, E. Kuokstis, A. Khan, G. Tamulaitis, I. Yilmaz, M. S. Shur, J. C. Rojo and L. J. Schowalter. Appl. Phys. Lett., 2002. **81**(24): p. 4658-4660.

34. T. Nishida and T. Makimoto. Appl. Phys. Lett., 2004. **84**(6): p. 1002-1003.

CHAPTER 3

OPTICAL AEROSOL DETECTION

Instruments to detect and classify particles present in the ambient are abundant, examples include air quality monitoring in industrial or medical environments, and liquid treatment in water purification facilities. A particular subset of particle sensors, those employing optical techniques to detect airborne biological matter, have recently received considerable focus due to their potential to serve as portable early-warning sensors in the case of a bio-terrorist attack. This chapter introduces the basic requirements of such a sensor, gives a brief survey of system research and development to date, and explains what semiconductor UV sources offer towards this problem. Our work in this field is performed under the support of the DARPA SUVOS program, a defense department initiative which began in 2001 and is aimed at advancing the development of emerging nitride UV light emitters for the purpose of their application in fluorescence-based bio-agent warning sensors [1].

3.1. The bio-aerosol problem

Bio-aerosols encompass a large class of airborne particles which include viruses, bacteria, fungi and algae. When designing a bio-aerosol sensor, the particles of interest are generally bacteria and bacterial spores. Bacterial spores are a naturally occurring state of relative inactivity generated by certain bacteria when exposed to harsh environments. Spores require few nutrients to survive and can withstand considerable exposure to UV light, some can exist for many years in this state before finally 'reactivating' when the environment becomes suitable. Not all bacteria

are capable of producing spores, a process called sporulation, and spores of different bacteria differ in size, shape and chemical content. They are of particular interest since notoriously harmful bacteria - such as *bacillus anthracis* which causes anthrax, and *clostridium botulinum* which produces the neurotoxin causing botulism - form spores which may be further processed into fine powders that are easily aerosolized, inhaled and able to reach deep within the human respiratory system.

Bacterial spores may be characterized by their physical size or shape and chemical composition. Single spores have lengths that are on the order of 1 – 10 um, and may have many shapes including rod-shaped, spherical, helical or curved. Particles of this size are particularly hazardous to human health since they are lightweight and do not easily settle to the ground, and are capable of being inhaled. A common measure of the size of a particle is its aerodynamic diameter, which is the equivalent diameter of a particle with a density of 1 gm/cm^3 that has the same terminal settling velocity in air. This is a useful quantity as it allows comparison between particles of irregular shapes and various densities to be classified according to their behavior in the atmosphere. Particles with smaller aerodynamic diameter take longer to settle to the ground and hence are available for inhalation for a longer amount of time. For example, a suspension of 2-3 um particles may require several hours for a majority of the particles to settle, in comparison to 10 minutes for 13 um particles [2]. Furthermore, particles only a few microns in diameter are easily inhaled and can pass through the protective mucous membranes in the nose and mouth and settle as far down the respiratory system as the bronchioles and alveoli in the lung.

In order to be effective, a sensor for detecting the presence of bacterial spores must be able to provide a warning signal within a time scale that permits the evacuation or treatment of people in the affected areas. As a matter of balance between the capability to precisely identify a specific particle and the need take preventative measures, a time scale of operation of several

minutes is generally agreed upon for so-called early-warning sensors [3]. Techniques such as micro-biological assays have the capability to identify specific species which great precision, however, hazardous aerosols are usually present as a tiny minority of particles in the air, a condition that renders many bio-chemical analysis methods totally ineffective or too slow. On the other hand, a front-end sensor is one that can rapidly sort a sample of particles from the ambient and provide an early warning signal if potentially suspicious particles are present. It need not have microbiological-level specificity in identifying threats, but instead serve as a trigger to subsequent analyses which take significantly longer, up to hours, but have better identification capabilities.

To test the performance of bio-aerosol sensors, spores of the relatively harmless *bacillus atrophaeus*[1] (BG) are often used as a simulant for anthrax. BG spores are similar in size and composition to anthrax, and we will take them to be representative of spores in general for the purpose of determining the detection capability required for a sensor. Single spores are rod-shaped and nominally 1 x 2.5 um. **Table 3.1** lists the percentage of dry spore weight for molecules which have been used in optical bio-aerosol sensors. Spores are generally dehydrated, and the percentage may be converted to approximate number of molecules using a dry weight of 10^{-12} grams per spore, yielding roughly 10^{8} for the first three amino acids in the table.

molecule	% dry wt.
phenylalanine [4]	5
tyrosine [4]	6
tryptophan [4, 5]	5
dipicolinic acid [4, 5]	6-12
NADH	(see text)

Table 3.1 : Chemical composition of a BG spore.

[1] formerly *b. subtilis* var. *niger* or *b. globigii* and recently reclassified; names are used synonymously here.

3.2. Bio-aerosol fluorescence sensors

Although alternative techniques for bio-particle detection, ranging from PCR (polymerase chain reaction) to Raman spectroscopy, exist and are capable of bio-chemical specificity, we concentrate on fluorescence-based optical sensors here as they enable real-time analysis of single particles. Early bio-aerosol sensors measured a size-related parameter, such as light-scattering amplitude, and essentially counted numbers of particles within certain brackets of aerodynamic diameter. Commercial handheld instruments employing light scattering from a red laser diode are currently on the market[2] and are used in applications such as air quality monitoring in industrial or medical environments.

Fluorescence methods may be used in order to determine the chemical composition of a particle. It is possible to introduce external fluorescence markers which selectively tag a particular bio-particle [6], however, the native fluorescence of proteins in biological matter provide a natural fluorescence signature [7]. The key constituent molecules evident from fluorescence spectra of bacterial spores are the amino acids tryptophan and tyrosine, and nicotinamide adenine dinucleotide (NADH). **Figure 3.1** shows the normalized fluorescence absorbance and emission spectra prepared from solutions of these fluorophores in water. The absorbance lies almost entirely below 300 nm, with the exception of a smaller secondary maximum centered on 340 nm in the case of NADH. Riboflavin is not widely used as a signal from bacteria, although it can be useful in the case where UV sources for fluorescence excitation cannot be found. **Table 3.1** also indicates phenylalanine and dipicolinic acid (DPA) are present in significant quantities in spores. DPA has been found to be an excellent indicator for spores as it not present in significant quantities in active bacteria, however it fluoresces only in the presence of calcium ions [5].

---

[2] eg. Hach Ultra Analytics at *www.particle.com*, and TSI at *www.tsi.com*

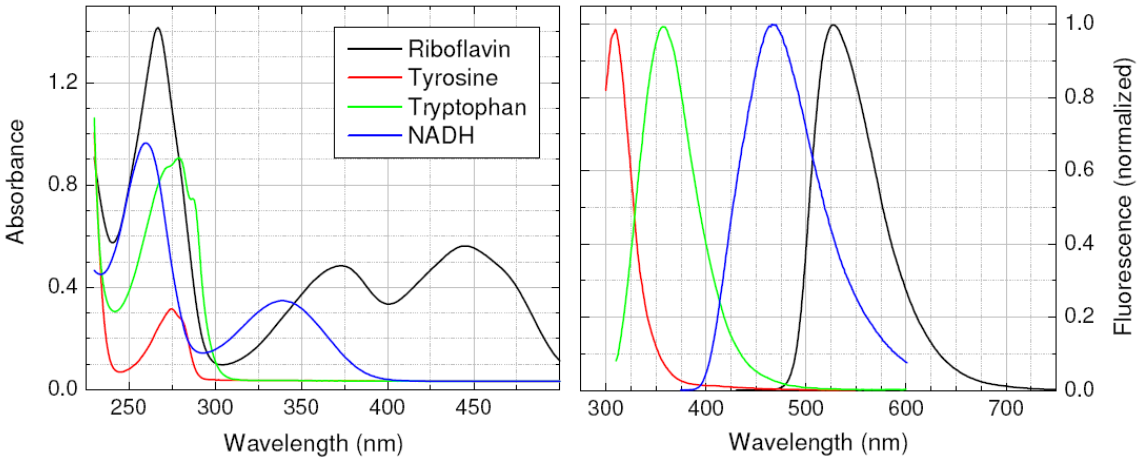

Figure 3.1 : Absorbance and fluorescence spectra of key bio-fluorophores.

The emission spectra shown in **Figure 3.1** are typical of fluorescence signals; relatively broad and lacking any sharp identifying features, compared to the wealth of information in Raman spectra for instance. This raises questions about the capability of fluorescence alone to distinguish between bacterial species. In the language of bio-agent sensing, a clear distinction is made between the ability to identify versus detect-to-warn. Fluorescence-based sensors enable discrimination between particles of biological origin and non-biological origin, but only have limited ability to distinguish between species of the former, and are thus suitable for font-end or detect-to-warn systems. Several studies exist which have attempted to find differences in the fluorescence signatures from spores and common background particles or interferents [8-11]. In general, the spectra are plotted in 2-dimensional wavelength space, that is, as a function of both excitation and emission (EEM spectra). **Figure 3.2** is an example EEM spectrum taken from a particular strain of BG spores which clearly shows tryptophan and NADH related emission peaks. A conclusion from these studies is that the preparation of the spore affects the emission spectra, which greatly complicates any attempt to use fluorescence to distinguish between bacterial species. Regardless of this complication, the dominant emission from bacteria and their spores are from tryptophan and NADH. This study will concentrate exclusively on these two

fluorophores, as is commonly done. It is noted that although we broadly attribute fluorescence emission in the spectral region 425-500 nm to NADH, this is a product of cellular respiration which is not expected in considerable quantities in dormant bacterial spores and thus there remains some debate as to the origin of this emission [12]. For this reason it is difficult to quantify the fraction of NADH in a typical spore as noted in **Table 3.1**.

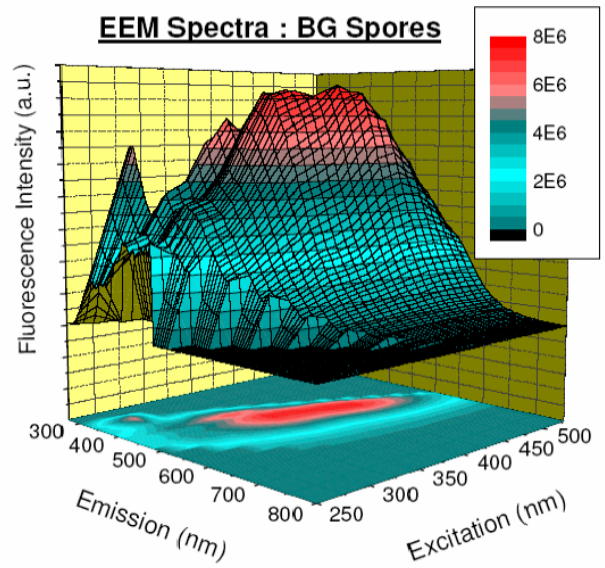

Figure 3.2 : Two-dimensional excitation-emission spectra of BG spores.
(Reproduced from [11] with permission of R. K. Chang.)

3.3. Laser induced fluorescence systems

Laser-induced fluorescence (LIF) has been applied to bio-aerosols using solid state lasers to provide UV excitation. Commonly available wavelengths include 355 and 266 nm, the third and fourth harmonics from a Q-switched Nd:YAG, 488 nm from an argon-ion, or 325 nm from a HeCd laser. The basic optical apparatus consists of simple optics to focus the excitation to a spot size on the order of 1 mm within a jetstream of flowing particles, collection optics with a large numerical aperture, and a fluorescence detector. In the case of a pulsed laser source, more sophisticated electronics and timing may be used in order to ensure that the excitation occurs when a particle is within the illuminated spot and thus maximize the fraction of interrogated

particles [10, 13]. Optical arrangements for collection of the emitted fluorescence are carefully tailored to ensure efficient collection of the relatively weak signal. One early sensor used moulded aspheric lenses [14], which have since been improved upon with elliptical mirrors or pairs of mirrors [15, 16]. Parabolic reflectors have also been used [17], as well as Schwartzchild reflecting objectives [10].

Arguably, the choice of detector provides a clear distinction between different sensors. UV-LIF systems may be broadly characterized as either those that employ an integrated fluorescence intensity measurement [14, 15, 18] using spectral filters to isolate the tryptophan and NADH fluorescence bands, or those that use a spectrometer for more complete spectral data acquisition [10, 19, 20].

UV-LIF sensors have been built and demonstrated to have single particle detection capability, however, in practical use these systems are ultimately limited by the size and cost of the solid state UV source and no widespread commercial instruments are currently available. Only a select set of wavelengths are accessible, and the instrumentation is too bulky to conceive of a portable unit. In a military application, one would like to have a compact system that could be carried by every individual, or in a civilian setting a distributed network of small and inexpensive sensors operating much like smoke alarms.

3.4. LEDs for fluorescence excitation

Until only a few years ago, solid state lasers were the most natural choice for UV excitation. With recent developments in gallium nitride based sources, described in detail in **Chapter 2**, semiconductor light emitting diodes and laser diodes have emerged as potential alternatives. LEDs emitting at 340 nm and 280 nm have ideal wavelengths for excitation of key

biofluorophores but are hindered by output powers that are orders of magnitude less than traditional solid state lasers. The spectral width and spatial incoherence of an LED are additional complications that are not encountered with lasers, and must be accommodated for in the sensor design.

A handful of reports demonstrating the use of UV LEDs in bio-sensing have been published in the last three years [21-23]. [23] and [22] describe bio-aerosol sensors using 345 nm LEDs to excite NADH in bacterial spores, whereas [21] displays an early use of 290 nm LEDs to excite the terbium chelate (complex) of DPA in solution. The latter case, the fluorescence of the rare-earth metal terbium is enhanced by the formation of a complex with DPA, however this is not a method which is suitable to airborne particle detection. These demonstrations use standard LED lamp configurations to deliver the light energy, and optical filters to isolate specific spectral bands associated with the bio-fluorescence. Optical systems originally designed for laser excitation are adapted for delivery of a maximum possible excitation flux from the spatially incoherent LED source to the aerosol target. All published demonstrations to date have used external optics to accomplish this adaptation. On the other hand, LEDs offer the advantage that the device geometry, and hence illumination pattern, can be easily tailored to accommodate a specific task. We propose to use a linear array of UV LEDs whose individual elements may be fired in rapid sequence so as to continuously illuminate a particle during its time-of-flight.

A linear array of separate UV LEDs offers several advantages over a single element device; an increase in the total energy delivered to the particle, which is achieved both by extending the excitation time as well as enabling the use of higher injection currents, and a reduction in the background signal. These advantages are quantified in **Chapter 5**, along with a full description of the sensor operation.

Our proof-of-concept use of linear arrays was performed with 32 individually addressable 470 nm wavelength LEDs to target riboflavin fluorescence [24]. These blue wavelength devices are fabricated from a standard InGaN-GaN multi-quantum-well heterostructure, which was chosen because it is a well-established material with high brightness and excellent operating characteristics. At the time these experiments were performed, 340 and 280 nm LEDs were not yet available in the research community. Each device has a circular aperture with a diameter of 70 um and is equipped with a photoresist microlens formed by a reflow technique. The center-to-center separation between elements is 100 um, as can be seen in **Figure 3.3**. In the demonstration, 50 um diameter water droplets doped with riboflavin are vertically ejected from a nozzle and the individual elements of the LED array are pulsed in sequence at a rate matching the average velocity of a droplet (the control methods for achieving this synchronicity are described in **Chapter 5**). Hence, each droplet is effectively illuminated by a continuous-wave photoexcitation of approximately 1 msec in duration. Single droplet spectra are acquired by a commercial spectrograph and CCD camera; 25 successive spectra from 0.02 % riboflavin (equivalent to 3 um solid particles) are shown in **Figure 3.4**. This result shows promise for the strategy of using linear arrays of LEDs to compensate for the lack of individual brightness, and motivates an investigation of emerging lower wavelength LEDs, which would be able to target tryptophan and NADH and have the potential to displace solid state lasers as the UV source of choice.

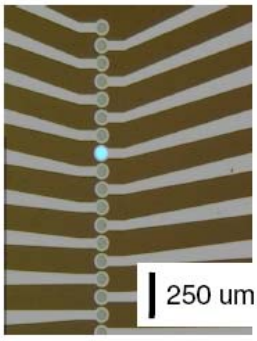

Figure 3.3 : Photograph of a linear array of 470 nm LEDs.

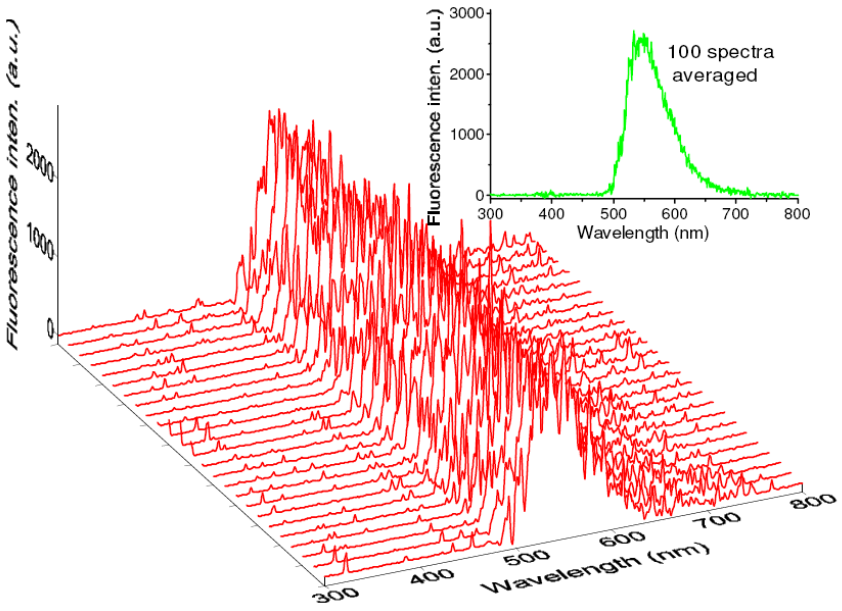

Figure 3.4 : Fluorescence spectra from single flowing 50 um riboflavin droplets.

In order to take full advantage of the small size and potentially lower cost associated with LEDs, the remaining sensor components must also be redesigned so that bio-aerosol sensor applications requiring portable solutions become feasible. In order to provide a truly competitive alternative to solid state laser-based systems, a miniaturized sensor should be capable of performing both simple filter-band fluorescence measurements and full spectroscopic detection. In this thesis, we illustrate the versatility of new UV LEDs under both detection schemes, and submit a novel, compact detector arrangement for the latter. Development of custom real-time electronics and a miniaturized aerodynamic deflector, the function of which is described in **Chapter 5**, is in keeping with the aim of significantly reducing the total size. Thus, by replacing all of the fundamental components with smaller and cost-effective alternatives, we demonstrate the capability of a genuinely portable aerosol particle sensor to perform tasks that are traditionally the realm of table-top size systems.

References

1. J. C. Carrano and A. J. Maltenfort. SPIE Unattended Ground Sensor Technologies and Applications IV, 2002. **4743**: p. 233-238.
2. H. Salem and D. E. Gardner, *Health Aspects of Bioaerosols*, in *Atmospheric Microbial Aerosols*, B. Lighthart and A. J. Mohr, Editors. 1994, Chapman & Hall: London.
3. J. Ho. Anal. Chim. Acta, 2002. **457**: p. 125-148.
4. W. G. Murrell, *Chemical Composition of Spores and Spore Structures*, in *The Bacterial Spore*, G. W. Gould and A. Hurst, Editors. 1969, Academic Press: London.
5. G. W. Faris, R. A. Copeland, K. Mortelmans and B. V. Bronk. Appl. Opt., 1997. **36**(4): p. 958-967.
6. M. Hart, H. Bond-Lin, J. Deich, A. Huston, J. Eversole and S. Knudsen. SPIE Optically Based Biological and Chemical Sensing for Defence, 2004. **5617**: p. 374-381.
7. J. R. Lakowicz, *Principles of Fluorescence Spectroscopy*. 1999, New York, NY: Kluwer Academic / Plenum Publishers.
8. P. C. Gray, I. R. Shokair, S. E. Rosenthal, G. C. Tisone, J. S. Wagner, L. D. Rigdon, G. R. Siragusa and R. J. Heinen. Appl. Opt., 1998. **37**(25): p. 6037-6041.
9. Y. S. Gheng, E. B. Barr, B. J. Fan, P. J. Hargis Jr., D. J. Rader, T. J. O'Hern, J. R. Torczynski, G. C. Tisone, B. L. Preppernau, S. A. Young and R. J. Radloff. Aerosol Sci. Technol., 1999. **30**(2): p. 186-201.
10. S. C. Hill, R. G. Pinnick, S. Niles, Y.-L. Pan, S. Holler, R. K. Chang, J. Bottiger, B. T. Chen, C.-S. Orr and G. Feather. Field Anal. Chem. Technol., 1999. **3**(4-5): p. 221-239.
11. M. W. Mayo, S. C. Hill and R. K. Chang, *Fluorescence of bacteria, pollens and naturally occurring airborne particles: excitation / emission spectra*, Unpublished work.
12. V. Sivaprakasam, A. L. Huston, C. Scotto and J. D. Eversole. Opt. Express, 2004. **12**(19): p. 4457-4466.

13. P. Nachman, G. Chen, R. G. Pinnick, S. C. Hill, R. K. Chang, M. W. Mayo and G. L. Fernandez. Appl. Opt., 1996. **35**(7): p. 1069-1076.

14. P. P. Hairston, J. Ho and F. R. Quant. J. Aerosol Sci., 1997. **28**(3): p. 471-482.

15. L. M. Brosseau, D. Vesley, N. Rice, K. Goodell, M. Nellis and P. Hairston. Aerosol Sci. Technol., 2000. **32**(6): p. 545-558.

16. P. H. Kaye, J. E. Barton, E. Hirst and J. M. Clark. Appl. Opt., 2000. **39**(21): p. 3738-3745.

17. M. Seaver, J. D. Eversole, J. J. Hardgrove, W. K. Cary Jr. and D. C. Roselle. Aerosol Sci. Technol., 1999. **30**(2): p. 174-185.

18. P. H. Kaye, W. R. Stanley, E. Hirst, E. V. Foot, K. L. Baxter and S. J. Barrington. Opt. Express, 2005. **13**(10): p. 3583-3593.

19. Y.-L. Pan, P. Cobler, S. Rhodes, A. Potter, T. Chou, S. Holler, R. K. Chang, R. G. Pinnick and J.-P. Wolf. Rev. Sci. Instrum., 2001. **72**(3): p. 1831-1836.

20. Y.-L. Pan, J. Hartings, R. G. Pinnick, S. C. Hill, J. Halverson and R. K. Chang. Aerosol Sci. Technol., 2003. **37**: p. 628-639.

21. Q. Li, P. K. Dasgupta, H. Temkin, M. H. Crawford, A. J. Fischer, A. A. Allerman, K. H. A. Bogart and S. R. Lee. Appl. Spectrosc., 2004. **58**(11): p. 1360-1363.

22. J. Cabalo, R. Sickenburger, M. De Lucia, J. Briles, A. Poldmae and D. Sickenburger. SPIE Sensors and C3I Technologies for Homeland Security and Homeland Defence IV, 2005. **5778**: p. 293-304.

23. T. H. Jeys, L. Desmarais, E. J. Lynch and J. R. Ochoa. SPIE Sensors, and Command, Control, Communications and Intelligence, 2003. **5071**: p. 234-240.

24. Y.-L. Pan, V. Boutou, R. K. Chang, I. Ozden, K. Davitt and A. V. Nurmikko. Opt. Lett., 2003. **28**(18): p. 1707-1709.

CHAPTER 4

MATERIALS AND DEVICE CHARACTERIZATION

In this chapter we return to the development of UV LEDs at the key wavelengths of excitation for intrinsic bio-fluorescence. Particular attention is paid to sub-300 nm wavelengths which have emerged from the research community within the time frame of this work. Epitaxial growth and layer structure design are briefly reviewed, followed by examples of as-grown material characterization. Microelectronic technique for nitride LED fabrication is detailed, and results from test devices at 340 and 290 nm are summarized with a view towards their utility in optical sensing; a topic which is continued in the next chapter. We conclude with the first demonstration of a 300 nm LED grown on bulk aluminum nitride, and thereby illustrate the potential of this substrate to yield high performance nitride devices.

4.1. Device structure and epitaxial growth.

The device structure of a typical 290 nm LED in this study is shown in **Figure 4.1**. Epitaxial growth of this structure is carried out by metalorganic chemical vapor deposition (MOCVD) performed by Prof. Han's group at Yale University. Details of the growth process are found elsewhere [1-4]. Briefly, nitride growth is performed at high temperature (~ 1000-1100°C) and moderate pressure (~ 60-100 mbar) in the MOCVD reactor. Precursors for group III and group V elements are trimethylgallium (TMGa), trimethylaluminum (TMAl), and ammonia (NH_3), while sources for Mg and Si dopants are bis-magnesium and silane respectively.

Growth is typically performed on a 2" diameter c-plane sapphire wafer, and begins with a high-temperature AlN buffer as the base epilayer. N-type layers include Si-doped superlattices for strain relief and contact formation. Several low temperature aluminum nitride interlayers are inserted to reduce cracking caused by the heavy doping of high aluminum fraction n-AlGaN [5]. The active region consists of 3-5 quantum wells (MQW) with well/barrier dimensions of 30/60Å, and is followed by a high aluminum content p-type EBL whose necessity was mentioned in **Chapter 2**. In order to enhance the conductivity, a short period superlattice is employed for the p-AlGaN [4]. Finally, the structure is capped with a thin (200 Å) p-GaN layer to facilitate the formation of electrical contacts.

A typical 340 nm LED differs from that described above primarily in the reduction of aluminum content by approximately 25 % throughout the structure. In addition, the metalorganic source trimethylindium (TmIn) is used to introduce a low percentage of indium into the quantum well. The table in **Figure 4.1** compares the average composition of n-type, p-type and active layers in 340 and 290 nm LEDs.

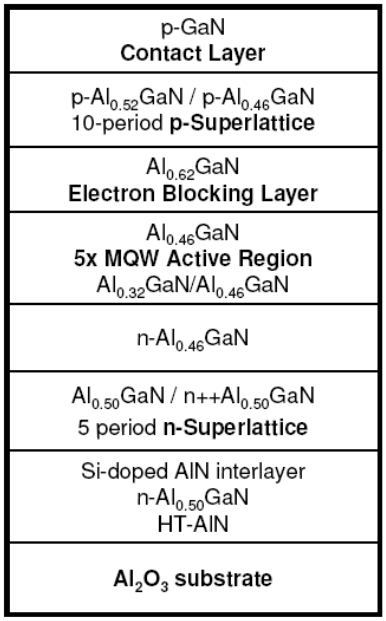

Nominal Al-fraction of AlGaN epi-layers for UV LEDs

layer		340 nm*	290 nm
p – SL		0.27	0.48
p – EBL		0.35	0.62
QW	well	0.16	0.35
	barrier	0.21	0.48
n – contact layer		0.26	0.50

* Quaternary quantum well ~ 0.02 indium.

Figure 4.1 : Epitaxial layer structure of a 290 nm LED.

4.2. Initial materials characterization.

Initial optical characterization of an epitaxial growth is via photoluminescence (PL) spectroscopy. In the simplest form of this technique, a laser of appropriate wavelength is focused onto a small area (< 1mm^2) of the wafer at an oblique angle, and the resulting luminescence is collected and focused onto the entrance slit of a spectrometer. The pump laser provides photons with energy greater than the bandgap of the material under study so as to create electron-hole pairs which can recombine radiatively and thereby yield information about the electronic structure. Primarily we employ PL as a rapid means to evaluate the optical quality of the active region. Measurements of absolute PL intensity can be used to evaluate the material quality, although we commonly use a reference sample to provide an indication of relative material performance between epitaxial growth runs.

For LED structures tailored to emit near 280 nm, we use a 248 nm KrF excimer laser (Lambda Physik, Optex Pro) as the pump source. **Figure 4.2** shows the room temperature PL of a 290 nm LED, clearly demonstrating band-to-band carrier recombination in the MQW active region. The emission peak at 430 nm is attributed to the p-GaN cap layer which, although it is relatively thin, absorbs the pump wavelength and attenuates the UV PL signal from the active region. A small defect emission peak centered on 330 nm is also observed. As discussed in **Chapter 2**, this emission has been observed by a number of groups and may be attributed to Mg-related deep levels, suggesting the need for improvements in electron confinement to the MQW region. From a single 2" diameter sapphire substrate used during each epitaxial growth run, a quarter wafer is used for photoluminescence study and device processing. PL intensity, and consequently device performance, has been found to vary along the radius of the wafer as illustrated by **Figure 4.3**. This variation may be attributed to gas flow characteristics in the

MOCVD reactor, and PL provides a rapid determination of the wafer area best chosen for full device fabrication.

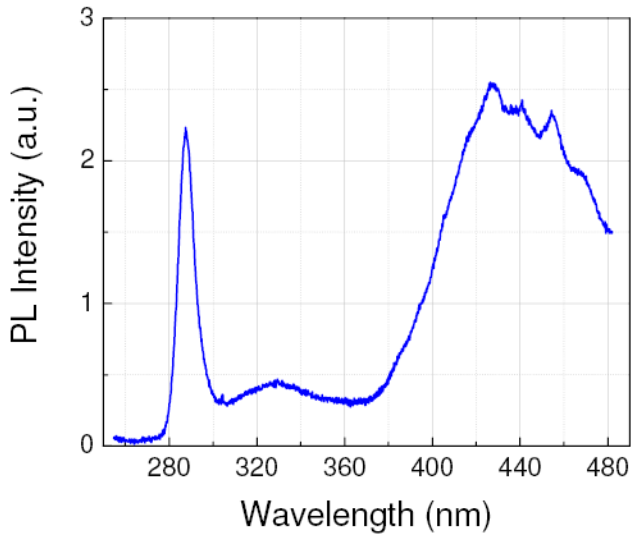

Figure 4.2 : PL spectrum from a 290 nm LED.

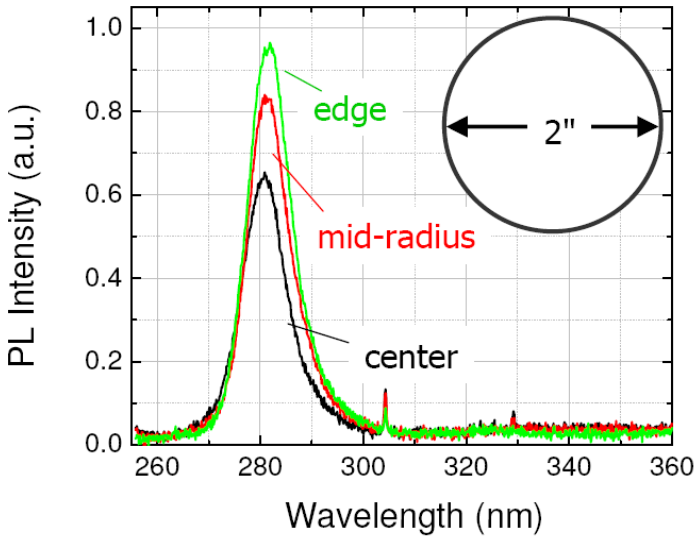

Figure 4.3 : Typical variation in PL across a 2" wafer.

4.3. LED fabrication process

Our nitride LED device fabrication begins with an MOCVD-grown epitaxial thin film on a sapphire substrate. **Figure 4.4** is a schematic illustration of the standard LED device process flow described in this section.

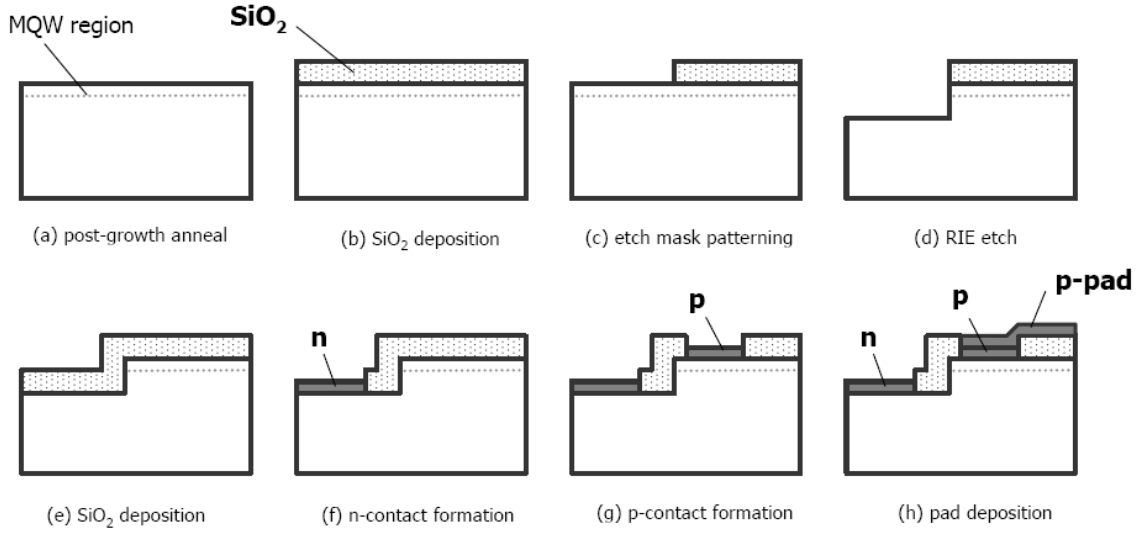

Figure 4.4 : Schematic of the standard nitride LED fabrication process.

The process begins with a high temperature post-growth anneal to activate magnesium dopants in the p-type nitride layers. This step may be performed in-situ after epitaxial growth, although it is often left as initial device processing step. Typically, post-growth annealing is performed at 700 °C for 10 minutes. The anneal conditions are chosen to be sufficiently high so as to activate the p-dopants, while considering the growth temperature of the active region in particular so as not to induce material damage. The required thermal energy is related to the activation energy of the Mg acceptor, which increases with increasing Al fraction [6]. The post-growth anneal, as well as all contact annealing, is performed in a rapid thermal annealer (RTA, RG Associates Heatpulse 610) capable of reaching 1000 °C in under one minute.

For LEDs grown on non-conducting substrates, which includes both sapphire and aluminum nitride, an etch step is required to reach the n-type contact layer. A typical target etch depth is 0.3 um, for which silicon dioxide (SiO_2) is a sufficient etch mask. Based on the etch selectivity of the nitride etch recipe between SiO_2 and AlGaN, a mask thickness of 2500 Å is used. Silicon dioxide is deposited with a plasma enhanced chemical vapor deposition system (PECVD, PlasmaTherm 790 Series) at a rate of 300 nm/minute using silane and nitrous oxide for precursors. The SiO_2 is then patterned using a standard photolithographic technique, employing a positive tone photoresist (PR, Shipley S1818) and the I-line (405nm) of a Karl Suss UV aligner. Following developing and cleaning in oxygen plasma to remove PR residue (PlasmaTherm), the silicon dioxide is etched with a combination of CF_4 dry etch (PlasmaTherm, RIE) and wet chemical etch by buffered hydrofluoric acid (BHF). This portion of the process is illustrated in greater detail in parts (a) through (d) of **Figure 4.5**, followed by a solvent wash to remove the photoresist leaving only the SiO_2 mask prior to the nitride etch step. This brings us to part (c) of **Figure 4.4**. A combination etch is used to maintain vertical sidewalls, particularly in samples with deeper nitride etch depths and/or fine alignment tolerances on the order of a couple of microns.

Nitride etching is performed by chlorine-based reactive ion etching in a load-locked reactive ion etcher (Trion Technologies, Minilock II). **Table 4.1** provides etch recipes developed for nitride films and their etch selectivity compared to the silicon dioxide mask. Also shown for reference is an etch recipe for GaAs used in the same instrument. The remaining SiO_2 is then removed prior to a new PECVD deposition, again SiO_2 of a similar thickness, which serves as a passivation layer in the final device. Following the process to this point we arrive at step (e) of **Figure 4.4**.

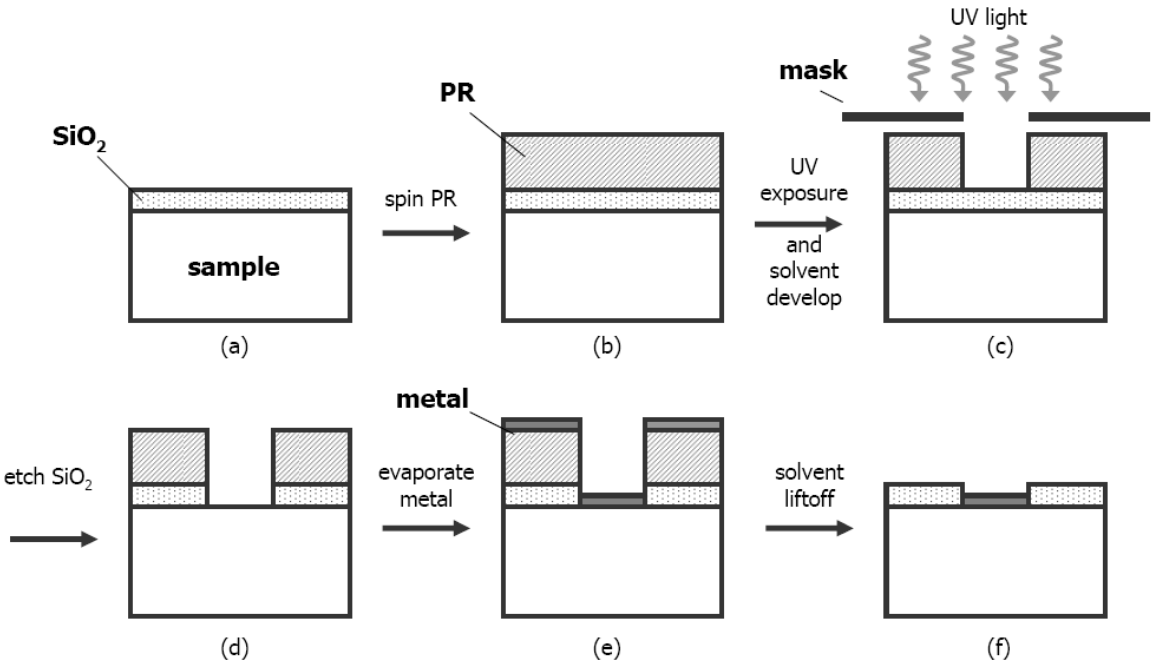

Figure 4.5 : Schematic of the photolithographic liftoff process.

The n-contact is opened by photolithography and wet chemical (BHF) etching of the SiO_2. Due to the high aluminum fraction of the n-contact layer – between 0.25 and 0.5 in the case of 340 nm and 290 nm devices respectively – a further treatment in buffered oxide etchant (BOE) is used immediately prior to metal deposition in order to remove native oxides. A multi-layer metallization is then deposited by electron-beam evaporation, followed by liftoff of the remaining PR to reveal the n-contact pattern. This process is outlined in **Figure 4.5**. All contacts to both n- and p-type nitrides are alloys and require a relatively high temperature anneal (RTA) in nitrogen-rich ambient to achieve ohmic character. The p-contact is formed by a similar sequence of photolithography, wet chemical (BHF) etch, electron-beam evaporation of a multi-layer metallization and a high temperature anneal. **Table 4.2** provides contact schemes to several nitride materials. Metallization schemes for p-GaN have been investigated for violet and blue LEDs for example, and thus a body of literature exists for the Ni/Au contact that we employ [7-9]. On the other hand, development of ohmic contacts to high aluminum fraction n-AlGaN for

290nm LEDs was required for the work presented here. Details of the contact development process and results are provided in next section. In the case of UV LEDs, the required anneal temperatures establish the order of contact deposition to n first followed by p.

A final step for device fabrication is the patterning and deposition of extended contact pads made of Ti/Au (100/1500 Å). In test devices the pads simply enable probing of devices whose apertures are too small (< 20 um) to easily probe alone. However, in LED arrays, the pad layout is designed to distance wiring from the active LED elements and to allow for the flip-chip packaging process described in the next chapter.

	290 nm LED	**340 nm LED**	**GaAs**
etch gases (sccm)	Cl_2 = 60 Ar = 12	Cl_2 = 60 BCl_3 = 12	Cl_2 = 4 BCl_3 = 10
RIE power	250 W	200 W	55 W
chamber pressure	40 mtorr	40 mtorr	5 mtorr
etch rate	45 - 55 Å / sec	35 - 40 Å / sec	~ 45 Å / sec
film : SiO_2 etch selectivity	7 : 1	5 : 1	na

Table 4.1 : Reactive-ion etch recipes for nitride films.

	metallization	**thickness (Å)**	**anneal conditions (in N_2)**
p-GaN	Ni /Au	100 / 400	600°C, 5 min
p-GaN semitransparent	Ni / Au	40 / 60	600°C, 5 min
n-$Al_{0.5}$GaN	V/Al/Ti/Au	150 / 850 / 200 / 950	850°C, 1 min
n-$Al_{0.25}$GaN	Ti/Pd/Al/Ti/Au	200/50/1000/100/900	800°C, 1 min

Table 4.2 : Contact recipes for nitride films.

Figure 4.6 is an optical micrograph and sketch of the standard test device used for UV LEDs in this study. Devices have circular apertures with either 50 or 100 um diameter. There is a pad associated with one of the 50 um devices to facilitate probing during characterization, and

all devices have pads that cover the p-contact aperture and hence are designed for backside light emission. The dimensions of note are the p-to-n and n-to-mesa distances which are 20 um and 12 um in the case of both the 50 and 100 um devices. The p-to-n distance should be minimized in order to alleviate current crowding problems which plagued early material growths. Due to the required BOE surface treatment prior to n-contact evaporation, sufficient distance must be allotted to the n-to-mesa separation to allow for several microns of SiO_2 undercut.

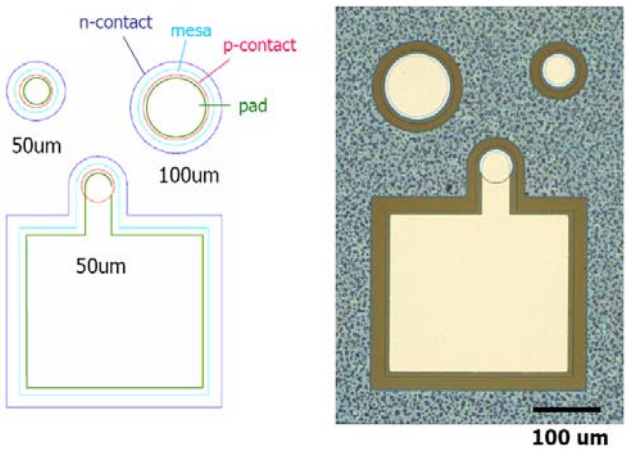

Figure 4.6 : Optical micrograph and dimensions of UV LED test devices.

4.4. Development of ohmic contacts to n-AlGaN

In order to make a nominally 280 nm LED, electrical contact must be made to n-$Al_xGa_{1-x}N$ with x ~ 0.5. Our standard n-contact for 340 nm LEDs, where x ~ 0.27, consists of a titanium-aluminum based metallization and a similar system has been demonstrated with 280 nm LEDs by Khan et al. [10]. Owing to its ability to form stable nitrides and it's close work function (4.3 eV) match to GaN, vanadium (V) has also attracted interest from several groups for making contact to n-type nitrides [11, 12]. Taking cues from these reports we investigated 4 metallizations, the layer sequence and thicknesses of which are given in **Table 4.3**.

	metallization	thickness (Å)
1	Ti/Pd/Al/Ti/Au	200 / 50 / 1000 / 100 / 900
2	Ti/Al/Ti/Au	20 / 100 / 200 / 2000
3	V/Al/V/Au	150 / 850 / 200 / 950
4	V/Al/Pd/Au	150 / 850 / 200 / 950

Table 4.3 : Recipes for contact studies on n-$Al_xGa_{1-x}N$, x = 0.45.

For the purpose of this study, a 1 um thick film of x = 0.45 n-AlGaN was grown. Contact performance was evaluated using the transmission line method (TLM) with rectangular contacts [13]. In this technique a series of equally sized contact pads of width W and length d are patterned on to the n-type semiconductor film. The pads are separated by increasing distance L, and the resistance between adjacent pads is described by

$$R = 2R_c + R_{sc},$$

where R_c is the contribution from each contact and R_{sc} is from the semiconductor. **Figure 4.7** shows the pattern dimensions used in this study. Using the definition of semiconductor sheet resistance, $R_s = R_{sc}\,{}^{W}\!/_{L}$ in Ω/□, and the specific contact resistance derived from TLM analysis, ρ_c in Ω.cm^2, we rewrite this in the form

$$R = \left(2\frac{\sqrt{\rho_c R_s}}{W}\right) + \left(\frac{R_s}{W}\right)L.$$

We can also define a transfer length,

$$L_T = \sqrt{\rho_c R_s},$$

which is a measure of the characteristic distance over which the current changes under the metal, and sets a minimum on the desired contact length. This simple analysis neglects the finite contact length, and in order to simplify the process, no mesa etching was performed on the test structures and hence current flow at the edge of the pad can affect the measured resistance. These

contributions to the measurement error are not critical in this case where to first order some metallizations are not even of ohmic character.

Samples with the desired metallization were prepared by photolithographic patterning, electron-beam evaporation and liftoff, as described in the preceding section. As is the usual procedure for n-type AlGaN, the samples were immersed in BHF for 30 seconds immediately prior to metal deposition. In order to evaluate the effect of etching, a duplicate set of samples were prepared where a shallow (200 nm) RIE etch was performed over the entire nitride surface. All of the as-deposited metallizations illustrated Schottky behavior. Samples underwent a cumulative set of anneals from 600 °C to 900 °C in 50 °C increments, each for 1 minute under N_2 flow in the RTA. TLM measurements were made between each anneal temperature. Titanium-based contacts exhibited Schottky behavior at all temperatures, while the vanadium-based metallizations showed significantly smaller barriers or became ohmic at 700 °C and above. No clear trend was observed between the etched and as-grown surfaces. **Figure 4.7** shows a selection of current-voltage (I-V) traces for each of the contact schemes after annealing at 850 °C, and **Figure 4.8** illustrates the TLM analysis of the V/Al/Pd/Au contact which yielded the lowest specific contact resistance of $\sim 2 \times 10^{-5}\ \Omega.cm^2$. This respectable value is comparable to that achieved in other contact studies.

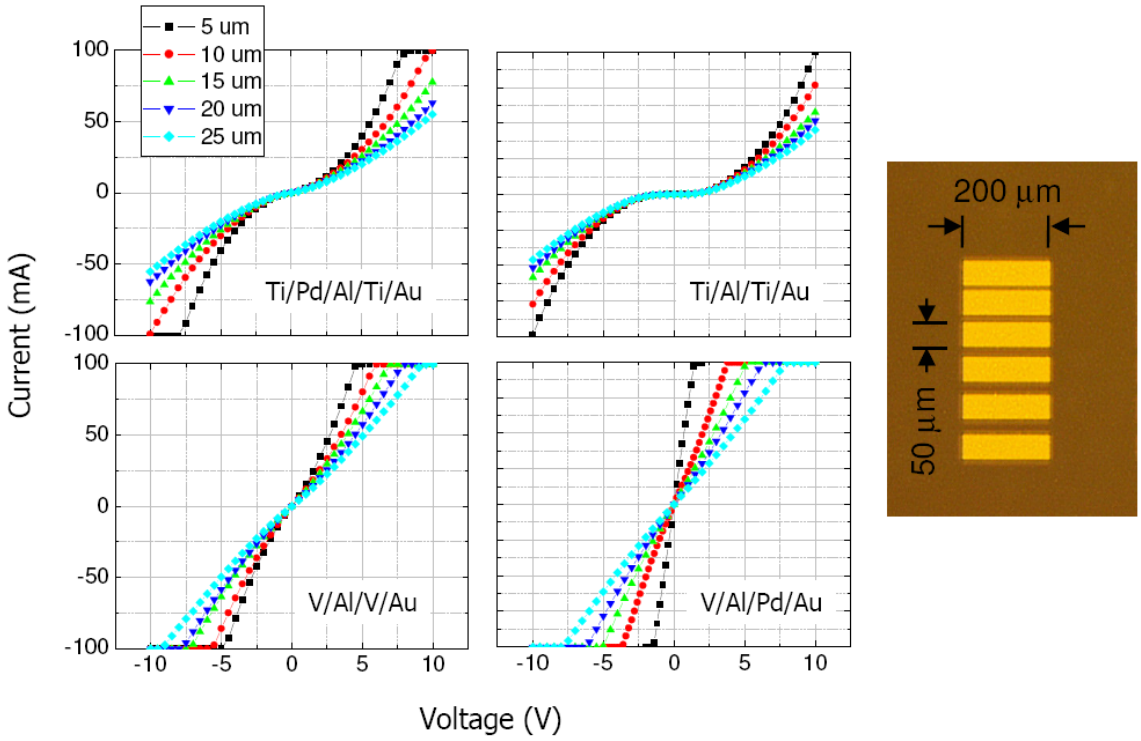

Figure 4.7 : I-V traces of TLM patterns to etched n-AlGaN.

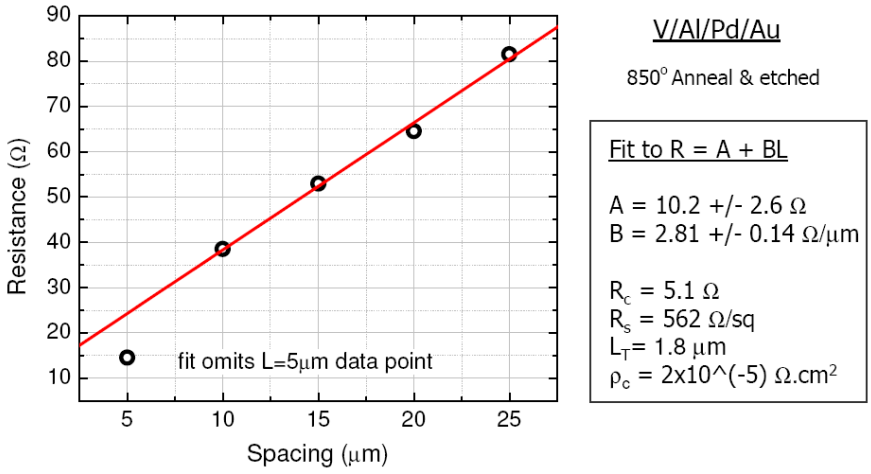

Figure 4.8 : Results of V/Al/Pd/Au n-contact scheme.

4.5. UV LED characterization.

Armed with a set of contact metallizations, LEDs are fabricated following the procedure described above. The electrical and optical characteristics of test devices are reported in this section. Initially, test devices are characterized directly on the chip using a parameter analyzer (HP 4145A) for CW measurements. The light output power is measured by a UV-enhanced Si-photodiode placed directly below the device, as illustrated in **Figure 4.9**. Thus, only light transmitted through the transparent sapphire substrate is collected. This method, in contrast to the use of integrating spheres common in the literature, keeps a view towards the practical application of UV LEDs as it measures only the fraction of useful light output power.

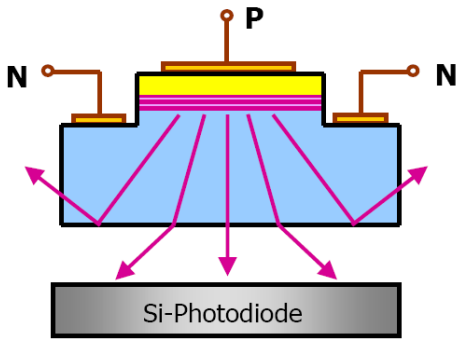

Figure 4.9 : Schematic of an LED output power measurement.

Light-current-voltage (L-I-V) curves measured from 50 and 100 um diameter devices for both 340 and 290 nm LEDs are shown in **Figure 4.10**. The series resistance for 50 um diameter 290 nm LEDs is 107 Ω, compared to 70 Ω in the case of 100 um devices. (For 340 nm LEDs the trend is similar with 70 Ω and 32 Ω respectively.) Both n and p contact resistances, vertical resistance encountered in the p-type layers, and lateral resistance in the n-type contact layer are all contributors to the series resistance. In the case of UV LEDs, the p-contact and lateral resistances due to low n-AlGaN conductivity in particular may cause a difference in series with different aperture size. As the aperture area A is made smaller, the p-contact resistance,

$$R_c = \rho_c / A,$$

increases whereas the lateral resistance (equivalently referred to as current-crowding) penalty is reduced. A typical specific resistance for the Ni/Au p-contact is 10^{-3} $\Omega.cm^2$, giving approximately 50 Ω and 13 Ω for 50 and 100 um devices respectively. This estimated resistance accounts for the majority of the difference between the data plotted in **Figure 4.10**, hence the disparity in electrical properties between the two sizes is generally attributed to p-contact effects and current-crowding does not play a significant role in these high-performance devices. Due to the lack of any packaging or heat dissipation scheme, device self-heating causes a clear thermal rollover in output power at high current densities. Maximum CW output powers in excess of 1 mW [4], and 100 uW have been measured from 100 um devices from 340 and 290 nm LEDs respectively. With the lack of thermal management, pushing to higher CW current densities beyond a point does not produce any increase in output power. However, driving the LEDs under low duty cycle and short pulse width conditions can eliminate transient heating effects and yield larger peak output powers. **Figure 4.11 (a)** shows a series of measurements from a 290 nm LED with modest CW performance, but capable of reaching 425 uW peak output power with 1 usec, 1 % duty cycle operation – corresponding to an increase in maximum output power by a factor of approximately 6. This gives a better measure of the fundamental performance of the epitaxial material, and provides motivation for using the LEDs in pulsed mode.

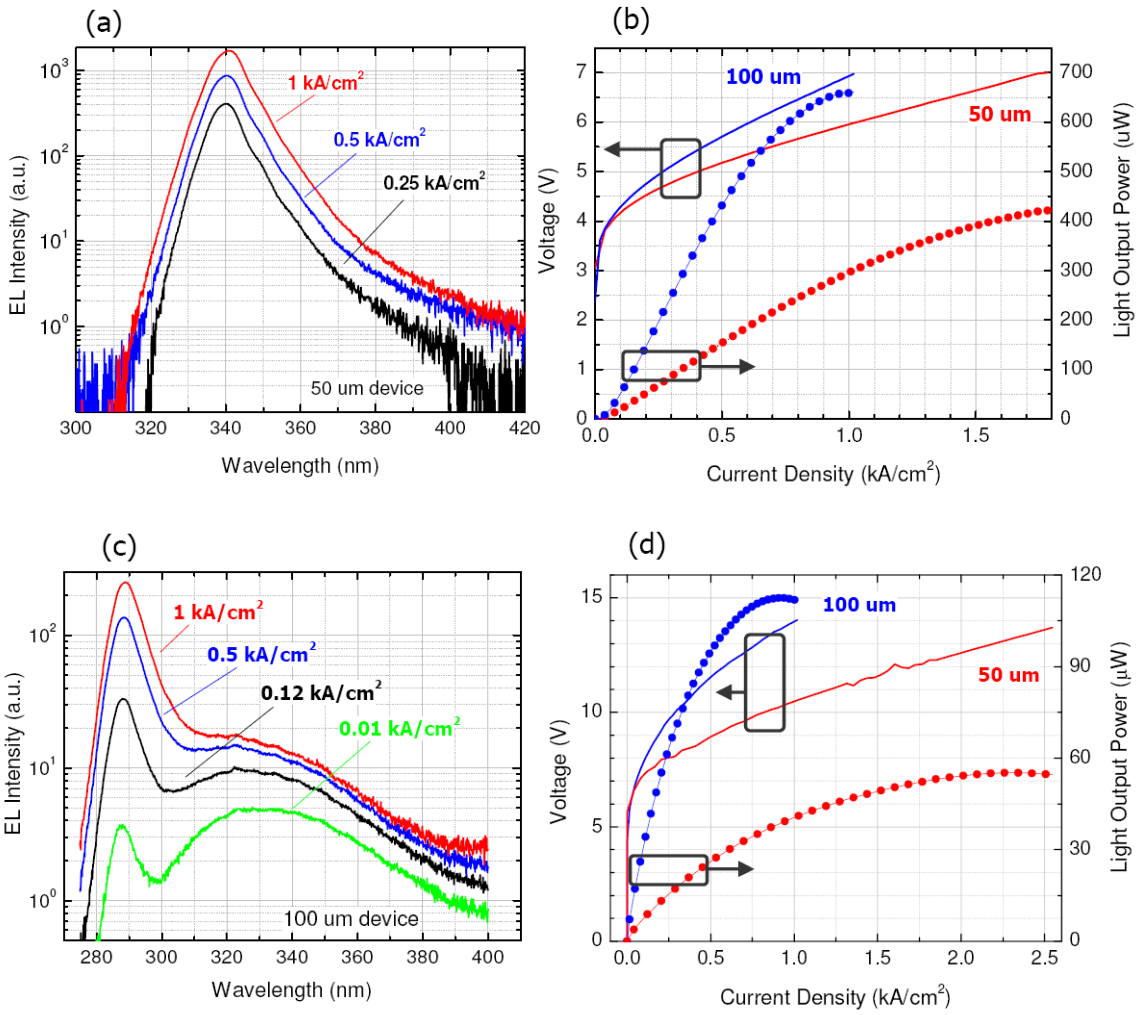

Figure 4.10 : EL spectra and CW L-I-V from a 340 nm (a,b) and 290 nm (c,d) LED.

Electroluminescence (EL) spectra are similarly acquired from the backside of unpackaged test devices. **Figure 4.10** contains EL spectra plotted on a semi-logarithmic scale in order to illustrate the long-wavelength components of the emission. 290 nm LEDs in particular suffer from deep-level associated emission at 330 nm. With increasing current injection the emission shows signs of saturation, and a ratio of 25 : 1 between the peak intensity at 290 and the defect is measured at 1 kA/cm^2. When used as an excitation source for fluorescence detection, the contribution of this long-wavelength component to the LED output power is not useful; it is

unable to excite fluorescence, and leads to confusion in the measured signal as it spectrally overlaps the emission from the fluorophore itself. Although the peak ratio may be quite small, the width of this long-wavelength emission can result in considerable total output power. In many cases this background signal is so large as to completely overwhelm the weak fluorescence signal and make any LED-based sensor useless without a judicious choice of excitation filter. **Figure 4.11 (b)** plots the fraction of integrated output power below a threshold wavelength (300 or 325 nm) as a function of the pulsed current injection. Due to the saturation of the defect emission, operating the LED at higher current densities results in a more efficient use of the generated light. Furthermore, representing the data in this manner illustrates the importance of the cutoff wavelength in a short-pass filter used to block the long-wavelength tail from a UV LED in biosensing applications. **Figure 4.12** plots representative CW EQE from unpackaged 100 um devices at 340 and 290 nm compared to a reference 460 nm LED. (The 460 nm LED has a similar geometry to the UV test devices, and was fabricated for use in neuron imaging as described in **Appendix A**.) The peak EQE for 290 nm (340 nm) is 0.1 % (0.3 %), and is a factor of 30-50 lower than high-efficiency blue LEDs.

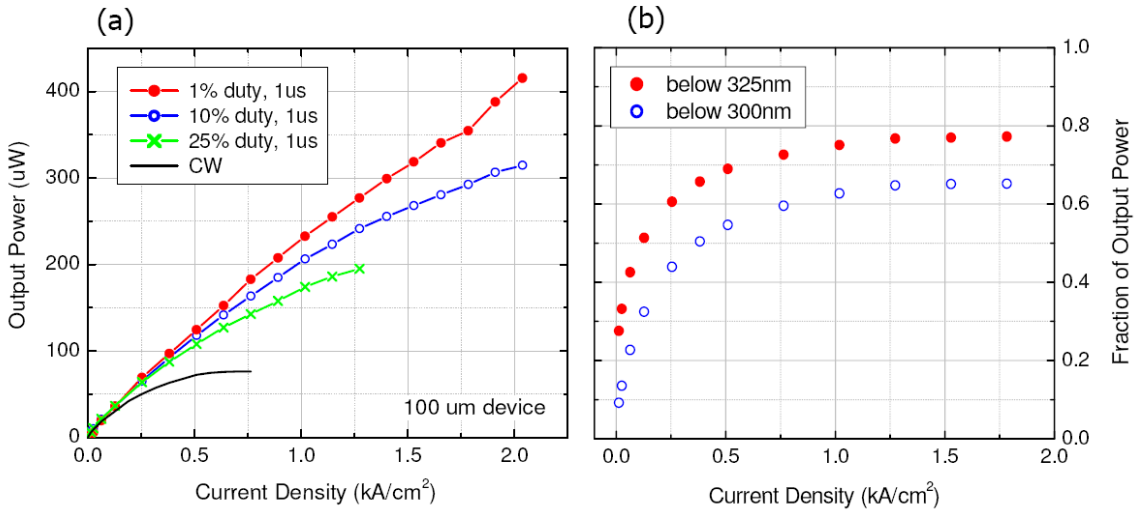

Figure 4.11 : Useful output power from a 290 nm LED.

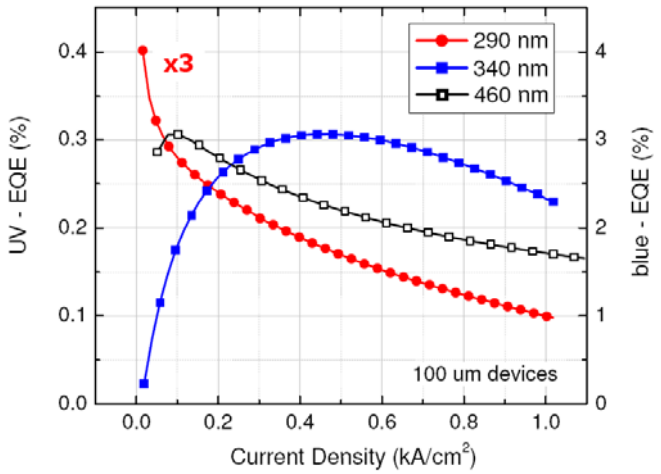

Figure 4.12 : EQE comparison between blue and UV LEDs.

Based on these results, and with the perspective of state-of-the-art UV LED performance provided in **Chapter 2**, a measure of success has been achieved in the growth and fabrication of UV LEDs. Although the efficiencies and output powers are modest by comparison to blue nitride-based LEDs for example, these devices represent the first generation of semiconductor UV light sources. These UV LEDs have sufficient performance to begin to be integrated into prototype optical sensors, as is demonstrated in the following chapter.

While there remains considerable room for improvement in basic material quality, there are clearly also light extraction and thermal management issues which can improve device utility. Together we will refer to these as a packaging issue, which is in itself not unique to wide bandgap semiconductors. However, device heating is particularly problematic for AlGaN-based LEDs. As the bandgap widens, nonradiative processes can become increasingly significant, leading to lower radiative efficiencies and contributing to device self-heating. The larger contact and bulk resistances of high-aluminum fraction devices further increase internal heating. One method to heatsink an LED is by flip-chipping it onto a material with high thermal conductivity. The flip-chip process is explained in **Chapter 5** in conjunction with packaging LED arrays, but for now

we illustrate its effect on CW output power and EQE in **Figure 4.13** (courtesy of Dr. Y.-K. Song). In this case, a 340 nm LED has been mounted onto a patterned silicon substrate using large indium balls. The two data sets (from different devices) show a large increase in maximum output power for the flip-chipped device owing to a delayed thermal rollover. This demonstrates the same thermal effect as **Figure 4.11 (a)** where pulse mode operation was used, but enables high light output powers to be generated in applications requiring longer LED pulse widths. Thus, before integrating UV LEDs into a bioaerosol sensor, we will expend some effort in **Chapter 5** to design a packaging scheme that makes best use of the relatively low output power.

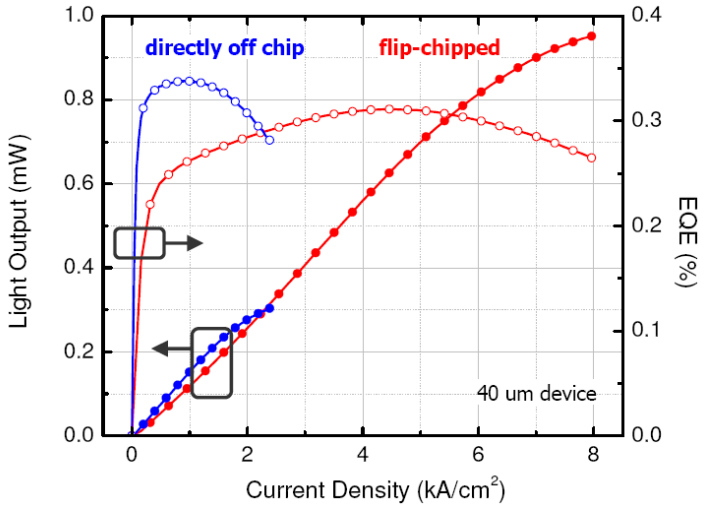

Figure 4.13 : Advantage of flip-chip packaging.

4.6. Demonstration of 300 nm LEDs on AlN

The above discussion concerning heat management in deep UV LEDs serves as a good segue to aluminum nitride substrate technology as a high thermal conductivity is one of its key advantages. Device results presented thus far are from nitride structures grown on sapphire. As enumerated in **Chapter 2**, AlN is superior to sapphire in many ways but is in short availability.

Bulk AlN substrates are attractive for deep UV optoelectronic applications because of the close matches in thermal expansion coefficients and lattice parameters, as well as good thermal conductivity and reasonable UV transparency. In this study, bulk AlN is provided by Crystal-IS and has undergone a proprietary surface preparation prior to epitaxial growth.

Compared to **Figure 4.1**, the LED layer structure has simplified buffer and n-type regions, while the MQW and p-type layers remain unchanged. To accommodate the 1.2% in-plane compressive lattice mismatch between AlN and the n-AlGaN electron transport layer, three superlattices with step-graded average compositions (x ~ 0.9, 0.73, and 0.57) were inserted with the goal of maintaining a constant compressive strain to promote dislocation reduction and strain relaxation. The n-contact is now made to a 1 um thick n-AlGaN layer. Homoepitaxy, the growth of high aluminum fraction AlGaN over AlN, is expected to be an easier process, and the availability of AlN substrates provides a promising platform for the growth of low-dislocation AlGaN even though the compressive mismatch is a source of structural imperfection. Bulk substrates prepared with the same method have shown dislocation densities below 10^3 cm^{-2} [14], and an initial estimate of the dislocations in the epi-layers is 10^7 cm^{-2}. Interrupted growth studies to examine the microstructural quality and growth evolution of AlGaN on AlN were performed, and the smooth background and atomic steps visible under AFM (atomic force microscopy) also suggest a low density of dislocations. The room temperature PL plotted in **Figure 4.14 (a)** shows a 4 times larger peak intensity than from a typical LED on sapphire, confirming that the optical quality of the MQW region is improved simply by changing the growth substrate.

Figure 4.14 (b) shows the CW LIV measured directly off the chip for identical device geometries of 100 um diameter UV LEDs grown on sapphire and AlN. The electrical characteristics are markedly improved on AlN, showing a sharp turn-on and greater than 30 % decrease in series resistance (to 45 Ω). TLM studies on the n-AlGaN contact layer with 50 %

aluminum content indicate a sheet resistance of 160 Ω/□, this in comparison to sheet resistances in the range of 560-840 Ω/□ typically achieved for our UV LEDs grown on sapphire substrates.

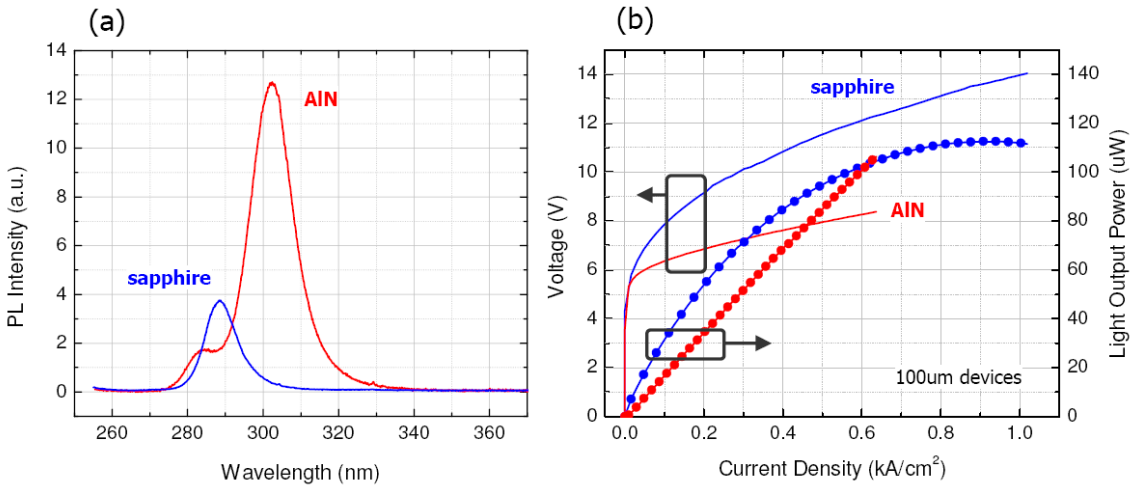

Figure 4.14 : PL and CW L-I-V comparison between UV LEDs on sapphire and AlN.

As before, backside light extraction through the AlN substrate was used to evaluate the light output power. Although pure single-crystalline AlN is intrinsically transparent in the near UV, current state-of-the-art bulk AlN is known to have a non-negligible absorption at these wavelengths and hence a comparison of absolute light output power in **Figure 4.14 (b)** is biased towards devices grown on sapphire. The higher refractive index of AlN also contributes to a smaller critical angle and less light is extracted because of total internal reflection. To compensate for some of this absorption, backside output powers, shown in **Figure 4.15 (b)** for 50um devices**,** are acquired after the substrate has been lapped to 150 um (following device processing). No further accounting for the finite absorption of the substrate was used, hence the extracted UV output power is expected to improve with the synthesis of AlN in addition to further optimization of the device structure and epitaxial growth conditions. A CW light output power of 210 uW is achieved at 2 kA/cm^2, corresponding to a light output power density in excess of 10 W/cm^2, and approximately 4 times larger than the maximum power from an identical device

on sapphire. Furthermore, the light output power shows no thermal rollover. This is attributed to the 10 times increase in thermal conductivity of AlN, reported at 3.2 W/cm.K, over sapphire. Neither of these devices have any additional heat sinking, but the conductivity of copper (4 W/cm.K) provides some perspective.

A series of EL spectra at increasing current injection, plotted on a semi-logarithmic scale in **Figure 4.15 (a)** for a 100 μm diameter device, illustrate a peak emission wavelength of 300 nm and a relatively small long-wavelength contribution. EL spectra are commensurate with PL studies which show a 4-8 times enhancement in intensity compared to devices grown on sapphire. Furthermore, the lack of any red-shift in the peak EL wavelength is another testament to the dissipation of device heating provided by the use of a high thermal conductivity AlN substrate. **Figure 4.16** contrasts the CW EQE of unpackaged devices on both substrates.

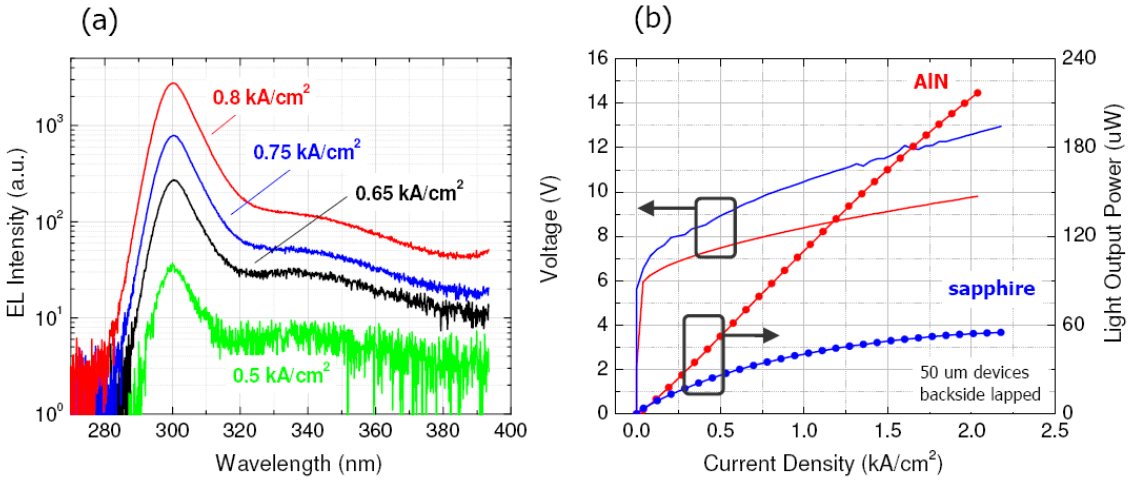

Figure 4.15 : EL spectra and CW L-I-V from a 300 nm LED on AlN.

Maximum EQE of 0.14 % have been achieved for small diameter devices operating under high current densities, compared with nominally 290 nm UV LEDs on sapphire which exhibit a smaller EQE and peak at low injection conditions. Without extensive optimization of growth and device parameters, we observed a distinct improvement in LED performance in light output,

device impedance, and thermal characteristics, indicating a promising new route to high performance UV optoelectronics. A peak EQE approaching 0.14 % is the best achieved in our collaboration to date, and is to my knowledge the first report of an LED grown on AlN emitting at such a short wavelength.

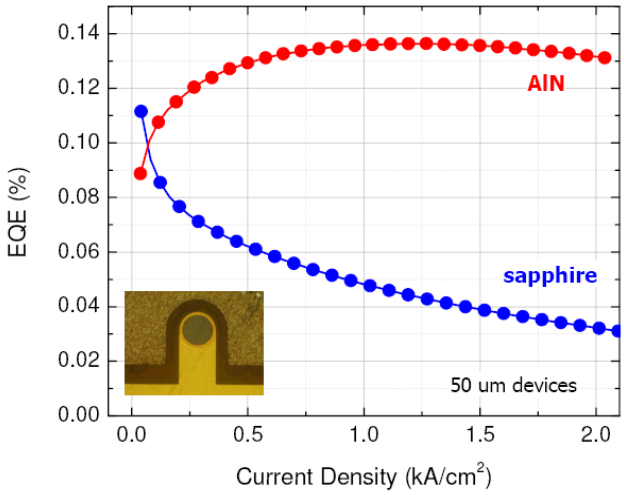

Figure 4.16 : EQE comparison of UV LEDs on sapphire and AlN.

At this time, an explanation is required for why all of the UV LEDs used in experiments described in the following chapters are on sapphire. AlN substrate technology and subsequent epitaxial growth has not yet demonstrated the uniformity and yield demanded by all engineering applications. On the scale of 20 um, AFM profiles indicate a root mean square surface roughness of approximately 35 nm in some areas, however, there is macroscopic surface texture and opacity variation over the nominally 1 cm^2 sample area which are visible to the naked eye. Not unexpectedly, device performance and yield also vary considerably across the substrate. Data presented in here are from select areas of the substrate and do not reflect the average characteristic. Rather, these results demonstrate the potential of high quality native nitride substrates to improve the overall optical and electrical performance of UV light emitters.

References

1. Z. Ren, S.-R. Jeon, M. Gherasimova, G. Cui, J. Han, H. Peng, Y. K. Song, A. V. Nurmikko, L. Zhou, W. Goetz, M. Krames and H.-K. Cho. Mater. Res. Soc. Symp. Proc., 2005. **831**: p. 21-26.
2. J. Han, S.-R. Jeon, M. Gherasimova, J. Su, G. Cui, H. Peng, E. Makarona, Y. He, Y.-K. Song, A. V. Nurmikko, L. Zhou, W. Goetz and M. Krames. SPIE Fourth International Conference on Solid State Lighting, 2004. **5530**: p. 61-68.
3. M. Gherasimova, J. Su, G. Cui, J. Han, H. Peng, E. Makarona, Y. He, Y.-K. Song and A. V. Nurmikko. Mat. Res. Soc. Symp. Proc., 2004. **798**: p. 17-22.
4. S.-R. Jeon, M. Gherasimova, Z. Ren, J. Su, G. Cui, J. Han, H. Peng, Y.-K. Song, A. V. Nurmikko, L. Zhou, W. Goetz and M. Krames. Jpn. J. Appl. Phys., 2004. **43**(11A): p. L1409-1412.
5. J. Han, K. E. Waldrip, S. R. Lee, J. J. Figiel, S. J. Hearne, G. A. Petersen and S. M. Myers. Appl. Phys. Lett., 2001. **78**(1): p. 67-69.
6. O. Ambacher. J. Phys. D: Appl. Phys., 1998. **31**: p. 2653-2710.
7. Y. Koide, T. Maeda, T. Kawakami, S. Fujita, T. Uemura, N. Shibata and M. Murakami. J. Electron. Mater., 1999. **28**(3): p. 341-346.
8. L.-C. Chen, F.-R. Chen, J.-J. Kai, L. Chang, J.-K. Ho, C.-S. Jong, C. C. Chiu, C.-N. Huang, C.-Y. Chen and K.-K. Shih. J. Appl. Phys., 1999. **86**(7): p. 3826-3832.
9. Y.-L. Li, E. F. Schubert, J. W. Graff, A. Osinsky and W. F. Schaff. Appl. Phys. Lett., 2000. **76**(19): p. 2728-2730.
10. V. Adivarahan, S. Wu, A. Chitnis, R. Pachipulusu, V. Mandavilli, M. Shatalov, J. P. Zhang, M. A. Khan, G. Tamulaitis, A. Sereika, I. Yilmaz, M. S. Shur and R. Gaska. Appl. Phys. Lett., 2002. **81**(19): p. 3666-3668.

11. J. O. Song, S.-H. Kim, J. S. Kwak and T.-Y. Seong. Appl. Phys. Lett., 2003. **83**(6): p. 1154-1156.

12. J. H. Wang, S. E. Mohney, S. H. Wang, U. Chowdhury and R. D. Depuis. J. Electron. Mater., 2004. **33**(5): p. 418-421.

13. G. S. Marlow and M. B. Das. Solid-State Electron., 1982. **25**(2): p. 91-94.

14. L. J. Schowalter, G. A. Slack, J. B. Whitlock, K. Morgan, S. B. Schujman, B. Raghothamachar, M. Dudley and K. R. Evans. Phys. Stat. Sol. (c), 2003. **0**(7): p. 1997-2000.

CHAPTER 5

LED ARRAYS FOR BIOAEROSOL SENSING

Moving onward from the evolution of nitride epitaxy and fundamental material performance delineated in the previous chapter, we now proceed to investigate the application of UV LEDs towards the bio-aerosol detection problem. We begin with a proof-of-concept demonstration of UV LEDs to excite bio-fluorescence using the test devices characterized earlier, and then design and implement an LED geometry and packaging scheme specifically tailored to the task at hand. **Figure 5.1** is a "big picture" view of the compact aerosol fluorescence detector system which evolves throughout this chapter [1-3]. The basic idea is to track each particle as it travels within the system; entry of the particle is detected by elastic scatter from a focused red LD, then UV-LEDs are used to excite native fluorescence. Based on the fluorescence signal, the particle is selectively removed from the jetstream by aerodynamic deflection and deposited onto a substrate for further analysis. Here the sensor is designed with the primary objectives of making a *real-time* and *compact* front-end sensor able to classify particles by fluorescence and physically sort a subset of particles from the background. To this end, and in keeping with miniaturization of the UV source, we design a compact optical system, introduce a mini deflector, and employ custom electronics to manage the system and accomplish real-time processing of optical data.

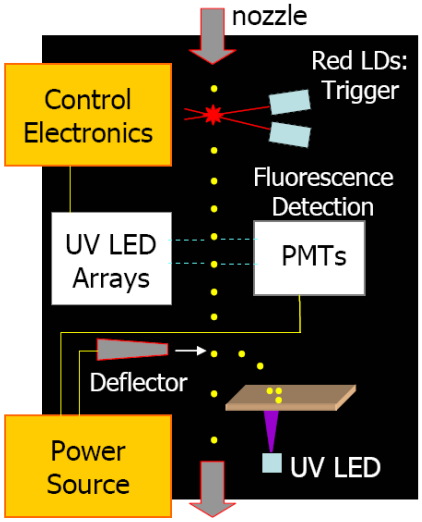

Figure 5.1 : Schematic of a compact aerosol fluorescence sensor.

5.1. Proof-of-concept : UV LEDs to excite bio-fluorescence

Given the performance of state-of-the-art UV LEDs as outlined in the preceding chapter, it is not clear that sufficient output power is generated to excite native fluorescence from bacterial spores. In order to investigate the ability of UV LEDs to serve as the excitation source, a test apparatus employing both 340 and 290 nm devices to excite a static sample is constructed. In the experimental arrangement, illustrated in **Figure 5.2**, two 50 um LEDs are focused to the same location of the sample and fluorescence is collected by two photomultiplier tubes (PMTs). Each of the PMTs is preceded by a bandpass optical filter to isolate either the visible (420 nm) or UV (340 nm) wavelength band, corresponding to NADH and tryptophan respectively. Similarly, the LEDs are each equipped with a filter to block the long wavelength emission. A 50 usec current pulse is applied to the LEDs, and the PMT signal is measured by a digital oscilloscope. **Figure 5.3** shows the dual-wavelength excitation and dual-band emission acquired from a sample of BG spores deposited on a UV-transparent sapphire substrate.

The use of multiple excitation wavelengths is a relatively common practice in aerosol sensors [4-6], and amounts to taking additional slices from the full 2D-EEM spectrum. In particular, 290 nm excites tryptophan more efficiently than NADH, whereas 340 nm excites only NADH. Some sensors operate by taking ratios of this limited set of information to determine the class of a particle. This method is useful in its simplicity, although we note that in any multi-wavelength apparatus care must be taken when some excitation wavelengths overlap a fluorescence band of interest. In this case, a mechanical chopper is used to block the UV PMT when the 340 nm LED is switched on.

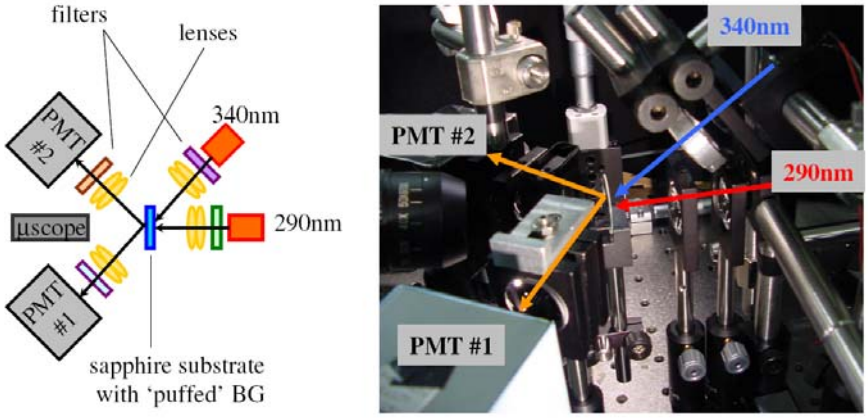

Figure 5.2 : Experimental setup for excitation of a static sample.

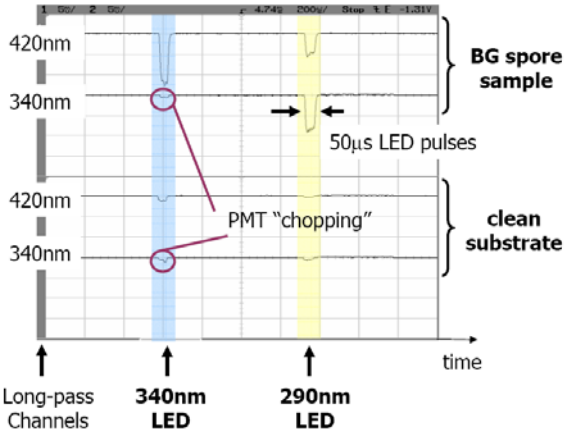

Figure 5.3 : Time-multiplexed, dual-wavelength excitation of static BG spores.

As noted in **Chapter 3**, the filter-band technique for fluorescence detection is common in bio-aerosol sensing – simplicity being its main advantage. As is the case with all sensors based on this technique, although the sample undoubtedly exhibits both visible and UV fluorescence, the origin of the emission is not clear. **Figure 5.4** shows the spectrum of the sample illuminated by a 290 nm LED acquired by replacing one of the PMTs with a commercial spectrometer. Spectral features from both tryptophan and NADH are visible, clearly demonstrating the ability of a UV LED to excite native fluorescence from BG spores. (The feature at 580 nm is the second order diffraction peak from the 290 nm LED.) The difference in relative intensity between the NADH and tryptophan spectral peaks is attributed both to the different excitation wavelengths, which translates to a difference in the relative absorptions, as well as to the observation that under high intensity UV radiation spores can be killed and the tryptophan fluorescence is diminished. The latter addresses the mystery surrounding the presence of NADH in bacterial spores and is consistent with the possibility that NADH is from the growth media and not directly from the spore itself [7].

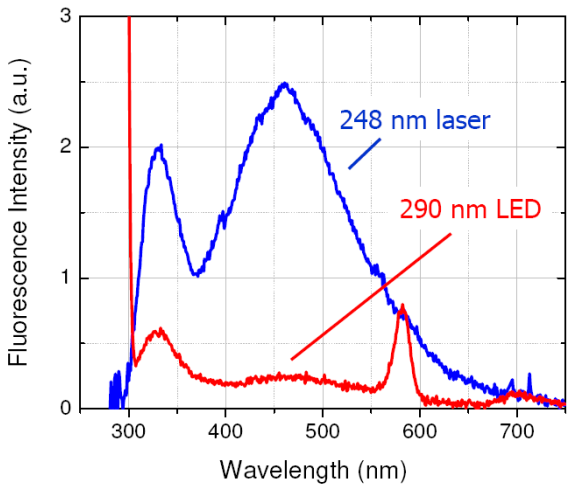

Figure 5.4 : Spectroscopic verification of BG spore excitation. (Intensity scaled.)

Figure 5.5 shows a fluorescence image of this sample of static BG spores taken using both a standard mercury lamp and a 50 um diameter 340 nm LED (50x longer exposure time) as sources of excitation. The LED successfully illuminates spores within a 50 um focused spot with sufficient power to excite native fluorescence. This comparison puts a positive perspective on the ability of a UV LED to target a small collection of spores.

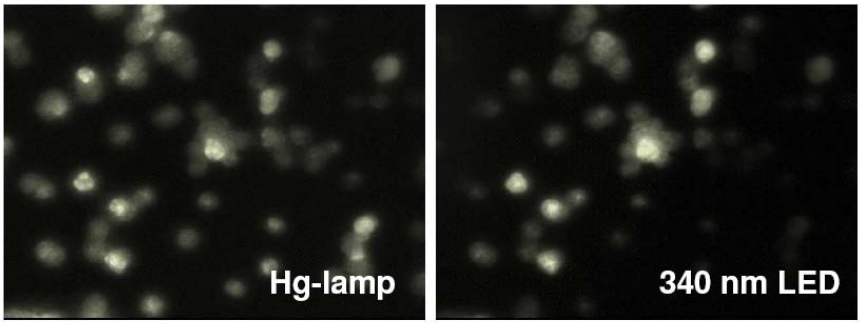

Figure 5.5 : Fluorescence images of static BG spores.

UV LEDs for Time-Resolved Fluorescence

As another illustration of the utility of UV LEDs toward bio-sensing in general, **Figure 5.6 (a)** shows the basic experimental arrangement used to acquire time-resolved fluorescence from a dilute solution of NADH excited by a 340 nm LED [8]. The LED is connected to a microwave stripeline (coplanar probe) for fast pulsed current injection. Pulsed excitation with 100 ps rise and fall times is delivered using the output of a picosecond pulse generator superimposed on a DC bias voltage which is slightly below the device threshold. A quartz cuvette is filled with the dilute solution and the collected fluorescence is filtered with a narrow bandpass optical filter prior to the multi-channel-plate PMT. Time-correlated single photon

counting (TCSPC) electronics are used to measure the sub-nanosecond electroluminescence and fluorescence lifetimes. After deconvolution, the decay time for the EL from the 340 nm LED shown in **Figure 5.6 (b)** is found to be approximately 0.4 nsec. This is sufficiently short so as to allow for discrimination of the fluorescence lifetime of 30 uMol NADH in water (0.45 nsec) and 1,2-propanediol (0.96 nsec). Using a series of narrowband emission filters, the decay times were found to vary over the spectral range of about 410-510 nm (full spectroscopic results are provided in [8]), and correlate with data in the literature acquired using large frame modulated UV lasers [9]. The variation in lifetime for NADH in different solvents speaks to the fact that the fluorescence is sensitive to the microenvironment surrounding the fluorophore, a fact which has been explored for bacterial discrimination but using flash-lamp excitation [10]. TCSPC techniques are not easily portable to on-the-fly aerosol analysis so this method of discrimination is not addressed further here, however, this demonstration illustrates the utility of UV LEDs to bio-fluorescence sensing in general and suggests a potential second-stage analysis using compact semiconductor sources.

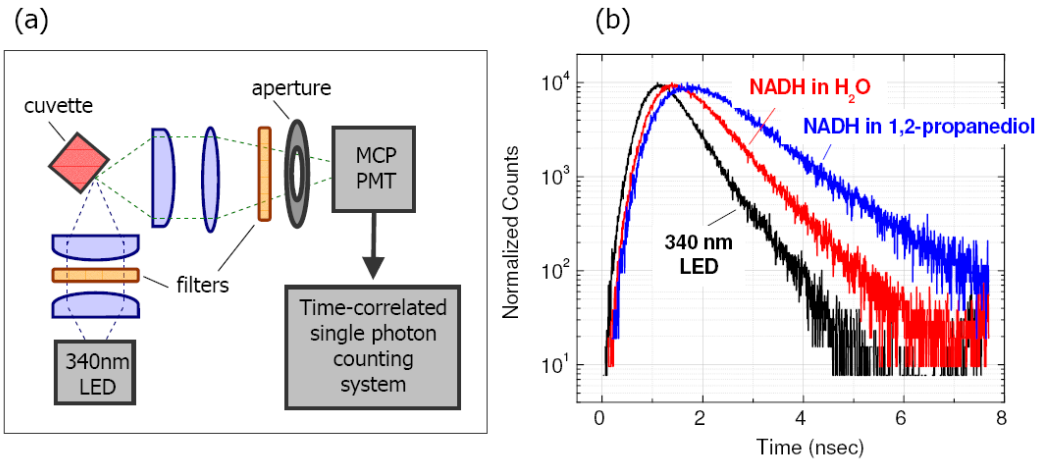

Figure 5.6 : UV LEDs for time-resolved fluorescence spectroscopy.

5.2. LED array design and fabrication

Equipped with proof that UV LEDs are able to excite native fluorescence, we proceed to design an LED geometry and package that is suited to the problem of on-the-fly bio-aerosol fluorescence excitation.

To mitigate for the low individual brightness of UV-LEDs, we design a linear array of individually addressable devices. The elements are fired in rapid sequence so as to continuously illuminate a particle during its time-of-flight, supplying an increase in the total excitation energy. An additional advantage is that pulsing the LEDs enables the use of higher injection currents, and provides a reduction in the background signal since only the element whose focus lies at the particle position is illuminated at any time. The concept of particle tracking with an array was demonstrated in our early work with high-brightness 460 nm LEDs presented in **Chapter 3** [11]. Here we improve on this report with a device geometry fully tailored to targeting airborne particles, and design a package for thermal management and optics for enhanced light extraction. However, the most significant advance remains the move to UV wavelengths. This represents not only a challenge in material epitaxy, but also enables the sensor to target native fluorescence and hence offer a viable alternative to laser-based systems.

Array Dimensions

In an LED-IF apparatus, as in standard LIF systems for aerosol analysis, particles are collected from the ambient air and ejected through a nozzle into the optical cell. The particular nozzle used in our system[3] yields a particle flow which remains laminar for at least 1 cm and

[3] Designed by Dr. Y.-L. Pan at Yale University and EDM-machined at Army Research Labs.

generates a jetstream with a width of approximately 200 um. These dimensions are met by our design of a 32-element linear array of UV LEDs composed of individual elements 200 um wide and 50 um high, illustrated in **Figure 5.7**. In order to accommodate the n-electrodes, the center-to-center separation of adjacent LEDs is 100 um, yielding a total array height of approximately 3.2 mm. The LED width ensures that most particles emerging from the nozzle are illuminated throughout their trajectory; the total array height of 3.2 mm enables it to fit comfortably within the stable jet stream while allowing for further components such as "triggering optics" employing elastic scattering above the fluorescence zone and an aerodynamic deflector following this zone, both of which are described later. Each of the 32-elements of the array is individually addressable while sharing a common n-electrode. The finger-like design of the n-contact between each optical aperture ensures that the lateral n to p distance in these mesa-etched devices is never more than 20 um, mitigating current-crowding effects that challenged early 340 nm LEDs, and which are one important device issue in emerging sub-300 nm semiconductor emitters.

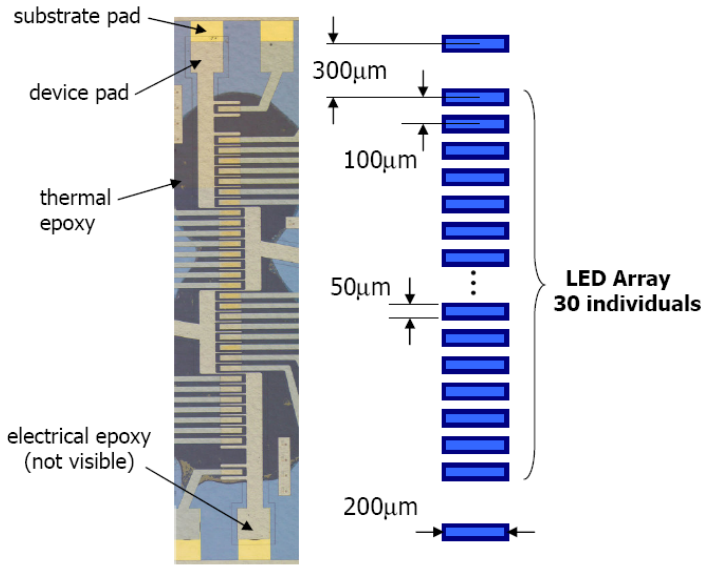

Figure 5.7 : Photographic image and illustration of LED array dimensions.

Optical and Electrical Packaging

As was highlighted in **Chapter 4**, proper management of heat generated by UV LEDs leads to increased output power. This enhances the utility and device lifetime, both important considerations in designing a component for integration into a practical instrument. One common packaging method used for microelectronic components is to flip-chip using solder bumps. This is similar to how the test device in **Figure 4.13** was assembled, and provides good heat dissipation through a large metallic bump. However, the small element-to-element separation of the array makes this process difficult to employ while maintaining the individual addressability. Thus, the array is designed with extended leads for electrical connections and a flip-chip process was devised in order to mount the array onto a patterned silicon substrate using epoxy. The leads are shown in **Figure 5.8 (a)** which is a photograph of the array as seen through the sapphire substrate after the flip-chip process. Electrically conductive silver epoxy (Epotek, H20E-PFC) is used to connect the individual device electrodes to the silicon substrate, and thermally conductive epoxy (Epotek, H70E-4) is applied in the vicinity of the optical apertures to aid in heat dissipation and to provide mechanical stability. **Figure 5.8 (b)** contains photomicrographs of the substrate with 250 um diameter epoxy dots which are deposited using an semiautomatic hybrid epoxy die bonder (K&S Industries, MAT 6495). The substrate and array are aligned using a flip-chip aligner and die bonder with autocollimation (RD Automation, M-9A) and then the epoxies are thermally cured. Finally, the assembly is mounted and wire-bonded to a commercial carrier chip, as shown in **Figure 5.9**.

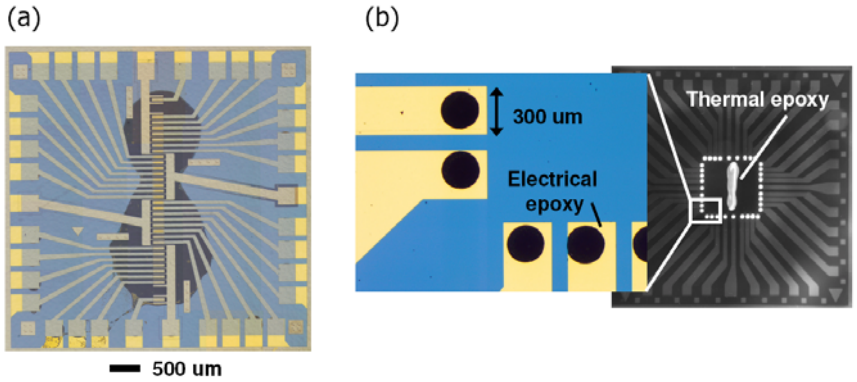

Figure 5.8 : Photomicrograph of (a) an array and (b) the Si-substrate for flip-chip packaging.

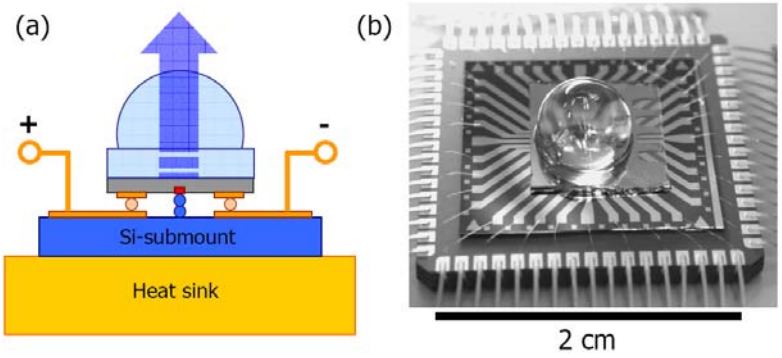

Figure 5.9 : Schematic and photographic image of a flip-chipped LED array package.

Also seen in **Figure 5.9** is a single sapphire lens which is affixed to the polished backside of the array with n = 1.56 UV-transparent epoxy (Epotek, 305/301-2). A simple argument using geometrical optics indicates that a macroscopic hemispherical lens aids in the extraction of light from the LED, and it is an easier to implement than other extraction techniques such as surface texturing or die shaping by anisotropic etching [12, 13]. The indices of refraction of nitride (n_n~*2.3*), sapphire ($n_{sapphire}$~1.75) and air (n_o~*1*) contribute to finite reflection at each boundary and a small critical angle, θ_c. Assuming isotropic radiation, the fraction of light emitted by the active region into the critical angle is

$$\eta_{crit} = \tfrac{1}{2}\left(1 - \cos\theta_c\right),$$

and the total transmission, *T*, through the nitride/sapphire and sapphire/air interfaces is approximated by

$$T \approx \left(\frac{4n_o n_{sapphire}}{\left(n_o + n_{sapphire}\right)^2}\right)\left(\frac{4n_n n_{sapphire}}{\left(n_n + n_{sapphire}\right)^2}\right).$$

The total light extracted from the device is a product of these terms. Without the lens, the bare chip has a critical angle of 26°, a transmission of 91 %, and a resulting extraction of only 4.5 %. With an infinite, perfectly hemispherical lens the critical angle is determined by the nitride/sapphire interface only and is 49.5°, while *T* is approximately the same, yielding a total extraction of 15.9 %. Thus, an LED equipped with this lens is predicted to supply 3.5 times greater output power than without. **Figure 5.10** plots the gain in output power measured from an LED array with a large hyper-hemispherical lens with respect to the power measured before mounting the lens. The gain is roughly 2.8 across the array, and drops off at the edge elements due to the finite size of the lens. Although the fact that the array and lens sizes are comparable leads to a reduction in the gain, sapphire lenses of the dimension indicated in the figure inset are commercially available and are compatible with the flip-chip packaging scheme employed. A hyper-hemispherical lens is chosen as it improves light extraction as well as serves as the first stage in the collection optics. Ray-tracing simulations confirm that the inclusion of the integrated sapphire lens improves the transfer efficiency of light from the array to the 200 um wide particle trajectory by a factor of 3 [14].

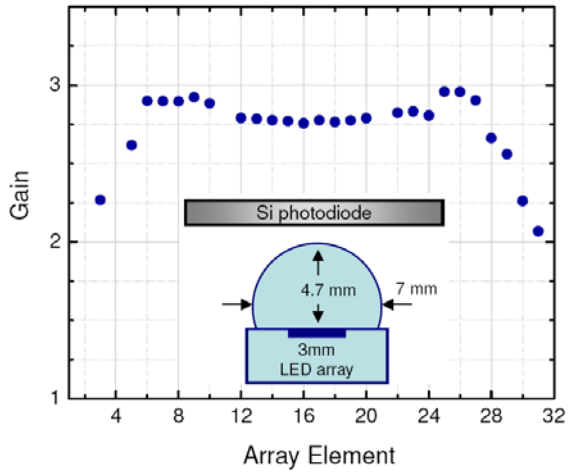

Figure 5.10 : Gain in extracted light output power due to a sapphire lens.

Performance

UV LED arrays are fabricated from the same epitaxial material as test devices which were characterized in **Chapter 4**. As an example, CW LIV measured across the 32 elements of a 290 nm LED array show a variation of about ± 15 % in output power at 0.5 kA/cm^2. This does not affect the function of the array, however it is useful to make note of this variation so that the time change in fluorescence intensity measured by the optical sensor can be correctly interpreted. One issue that does affect the utility of the array is current crowding. Current crowding was briefly mentioned in **Chapter 2** and is the reason behind the use of fingerlike contacts around each element of the array. In deep UV nitride materials it arises from the low conductivity of n-AlGaN. In mesa-etched structures the lateral resistance encountered in the n-type layer causes the current to preferentially pass through vertical layers, hence producing a crowding of current near the mesa. This is manifested as brighter optical output at the edge of the optical aperture. **Figure 5.11** contains close-up photographs of single array elements showing current crowding in an early material growth (upper image) and good current spreading from a device grown after improvements in doping and n-type conductivity (lower image). LEDs exhibiting severe current

crowding are of limited use in the array-based sensor since they deliver fewer photons to the aerosol particle. A more drastic interdigitation of the n-contact may be used to alleviate current crowding problem, however this has a number of significant drawbacks. The total light-emitting area would be reduced in order to accommodate the n-contact 'fingers' and a reduction in the mesa area would lead to an increase in device impedance caused by the p-contact as described in the context of test-device results presented in **Chapter 4**. The choice of a 50 um x 200 um optical aperture with center-to-center device separation of 100 um was chosen as a matter of balance, and improvements in n-type doping of current transport layers has reduced the influence of current crowding.

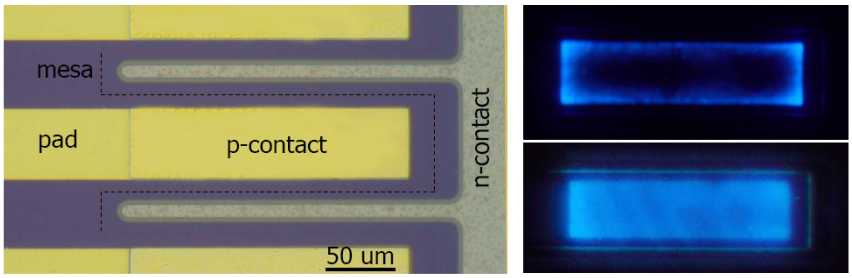

Figure 5.11 : Current spreading in a UV LED array element.

In the interest of being comprehensive, the performance of 340 nm and 290 nm LED arrays used in the fluorescence experiments to follow are given in **Figure 5.12**. The EL spectra are a reminder of the need for suitable filters to block the long wavelength emission, and the CW LIV accentuates the discrepancy between the two materials. In particular, the IV dictates the requirements for the LED array control circuit. In some experiments carried out prior to the development of shorter wavelengths, 370 nm LEDs are used. **Figure 5.13** gives the EL and LIV of this state-of-the-art InGaN material. Despite presently higher quantum efficiencies, this wavelength lies at the edge of the NADH absorption spectrum and as such is less desirable than the more challenging AlGaInN-based 340 nm or AlGaN-based 290 nm devices.

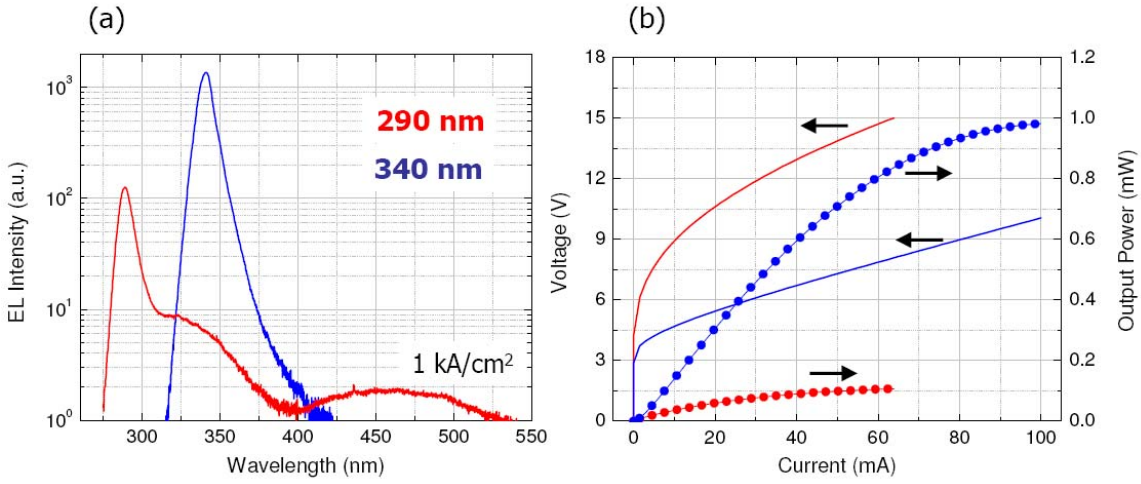

Figure 5.12 : EL spectra and CW L-I-V from 290 and 340 nm LED arrays.

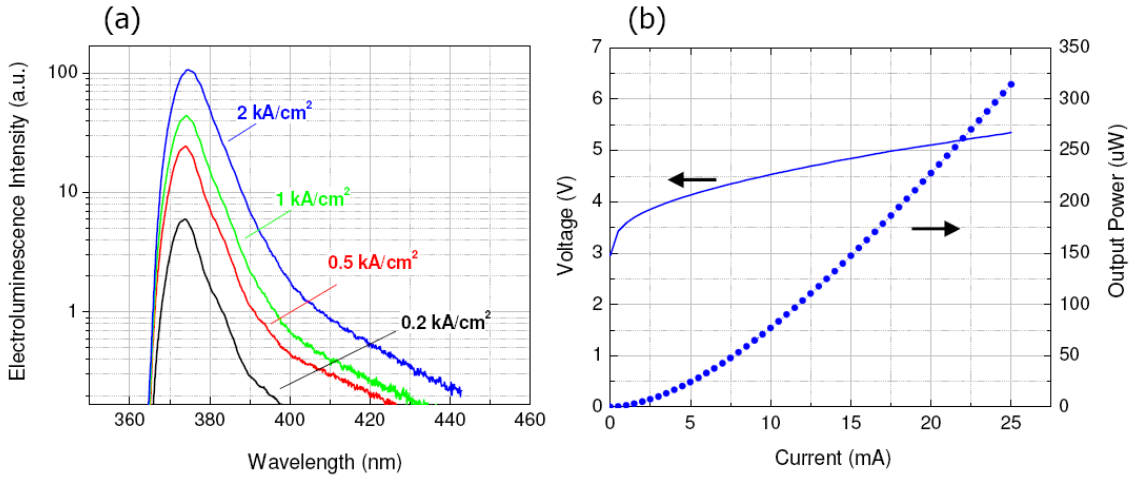

Figure 5.13 : EL spectra and CW LIV from a 370 nm LED array.

5.3. Test-particle generation

In a standalone system, particle collection is usually accomplished with a virtual-impactor particle concentrator, see for example [15]. This is a means to acquire particles from the ambient air and inject them into the optical system for analysis. In this thesis, in order to demonstrate sensor operation and quantify the system response, artificial particles are generated at known times and with known composition. The particles are composed of varying amounts of L-tryptophan (Sigma-Aldrich, T0254) or β-NADH (Sigma-Aldrich, N8129) intended to simulate the fluorescence from a bacterial spore. Two methods are used to create small particles, one in a liquid environment and one which is desiccated.

Wet Particles

In the case of wet particles, a commercial MicroDrop generator (MicroDrop GmbH) is used. This instrument makes use of the acoustic excitation from a piezoelectric transducer to produce small liquid drops on command. Common applications of the MicroDrop include dispensing epoxies to fix small optical assemblies or lubricating small mechanical parts, but in this case we use it to generate water droplets with a volume of approximately 200 nL. Correspondingly, the diameter of a single drop was measured to be roughly 70 um, as shown in the inset of **Figure 5.15**. In order to selectively dope water droplets with a small number of either tryptophan or NADH molecules, a solution of known concentration was supplied to the generator. This is a particularly useful tool as it reproducibly supplies nominally identical single particles for each trigger pulse it receives. An electronic circuit is used to control the delay between particle generation and the firing of the first element of the LED array, as well as the clock determining the sequential LED firing rate in order to synchronize with the particle velocity. Since a single water droplet with fixed delay is created from each trigger to the generator, the subsequent timing

is tied to this trigger and there is no need for other optical signals to determine the arrival of a particle into the system, greatly simplifying the initial testbed. In order to synchronize the LED pulsing with the droplet trajectory, the single droplet velocity must be known. **Figure 5.14** shows a series of time-delayed stroboscopic images of water microdrops. In **Figure 5.15** the distance of the particle from the nozzle opening is plotted as a function of the delay, indicating a constant velocity of 2 m/sec.

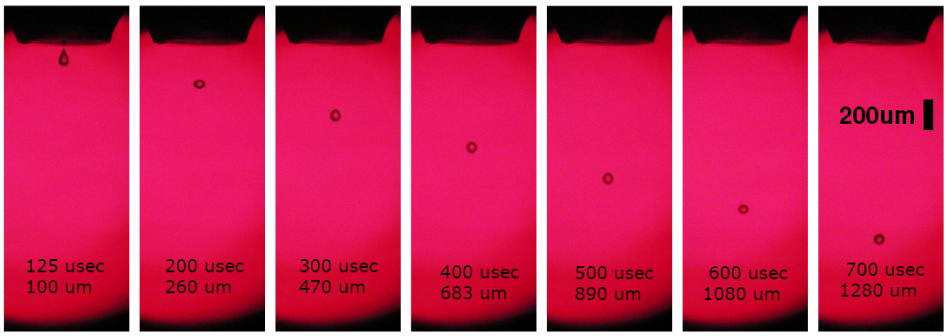

Figure 5.14 : Time-delayed sequence of stroboscopic images of microdrops.

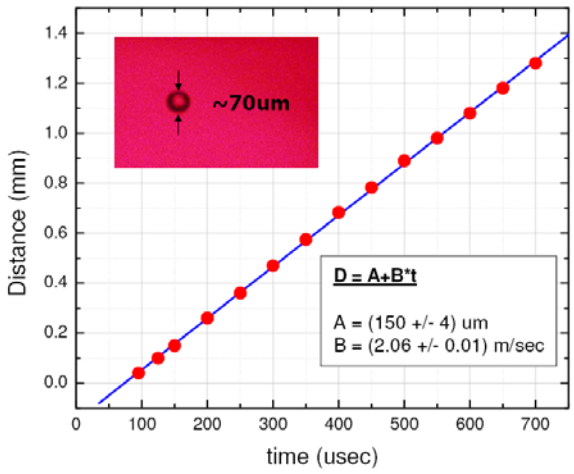

Figure 5.15 : Velocity measurement of water microdrops.

Dry Particles

In a fieldable bio-aerosol fluorescence detector, dry particles are collected from the ambient and passed through the system as collected. For testing purposes, we desiccated wet particles from the MicroDrop generator with a drying column supplied by Dr. J. Bottiger at the US Army's Edgewood Chemical Biological Center. The drying column is essentially an oven with air flow to carry the particles downstream, and is a portion of the Ink Jet Aerosol Generator (IJAG) system developed for producing test aerosols [16]. A nozzle is fixed to the exit from the column in order to further confine the particle stream. Although the MicroDrop generator produces a single particle per trigger with a constant delay and a narrow jetstream, the inclusion of the drying column and nozzle yields a wider jetstream and particles which arrive at irregular times. In this case – which more closely resembles the case of ambient collected particles – additional optical signals are absolutely required for synchronized timing. The average velocity of dry particles was measured using the elastic scatter from two red LDs focused 3 mm apart at the jetstream; **Figure 5.16 (a)** shows the resulting velocities as a function of the air flow rate supplied to the drying column. Part **(b)** contains optical images of 6 um diameter dry tryptophan particles generated from a 0.5 wt % solution and deposited onto a substrate approximately 1 cm below the nozzle tip.

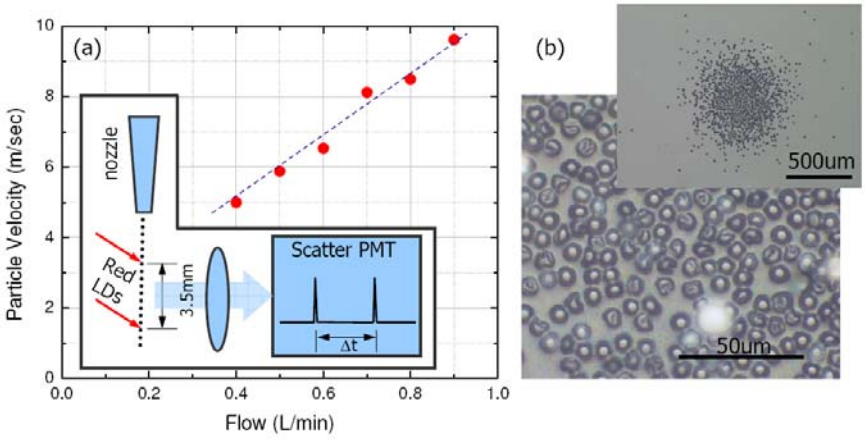

Figure 5.16 : Characterization of dry particles.

5.4. Optical design and testing

The performance and availability of UV LEDs continuously evolved throughout the duration of this work, and as a result the development of the optical system was not sequential in time, particularly with respect to the source wavelength. The organization of this section follows from the simplest optical testbed to the full electronic and optical sensor. Characterization at each stage is shown for both the 340 nm and 290 nm source wavelengths. We begin with a filter-based scheme to detect fluorescence from wet particles. This is followed by the design and implementation of a compact spectroscopic arrangement. At this point, the control electronics become significantly complex that a brief digression is required. The spectroscopic system is demonstrated with wet particles, and subsequently dry tryptophan.

5.4.1. Filter-based fluorescence detection

Figure 5.17 (a) is a schematic of the filter-based optical setup and shows the basic electrical interconnections. Part **(b)** is a photograph of the setup, which occupies a footprint of approximately 20 cm x 13 cm, as viewed from above. A diagram of the trigger and timing circuit which was built to control the sequential firing of the elements of the linear LED array in synchrony with the droplet motion is given in **Appendix B** (this is replaced by commercial electronics in more recent implementations of the system). **Figure 5.18** is a close-up image of the packaged array followed by an excitation filter. Due to the relatively small separation between excitation and emission wavelengths and the weak fluorescence signal, the long-wavelength tail associated with the LED must be blocked with a judicious choice of filter. In the 340 nm LED case, a filter centered at 330nm with a 50% transmission-maximum bandwidth of 75nm, rejects unwanted LED emission to better than OD4.5 (optical density) in the NADH fluorescence band; under 290 nm UV LED excitation the filter is centered at 275nm with a bandwidth of 50nm and

blocks better than OD3 in the tryptophan band. After the filter, a pair of short focal length, high NA (f = 16mm, F# 1.3), sapphire plano-convex lenses image the 32-element UV LED array onto the particle jet stream with a magnification of 1. Thus, the sequential firing of elements of the LED array results in a spatial tracking of the particle during approximately 3.2mm of its trajectory. Based on their high numerical aperture, sapphire ball lenses were also experimented with [14]; however, the extremely short focal length led to large LED background illumination owing to the large divergence angle.

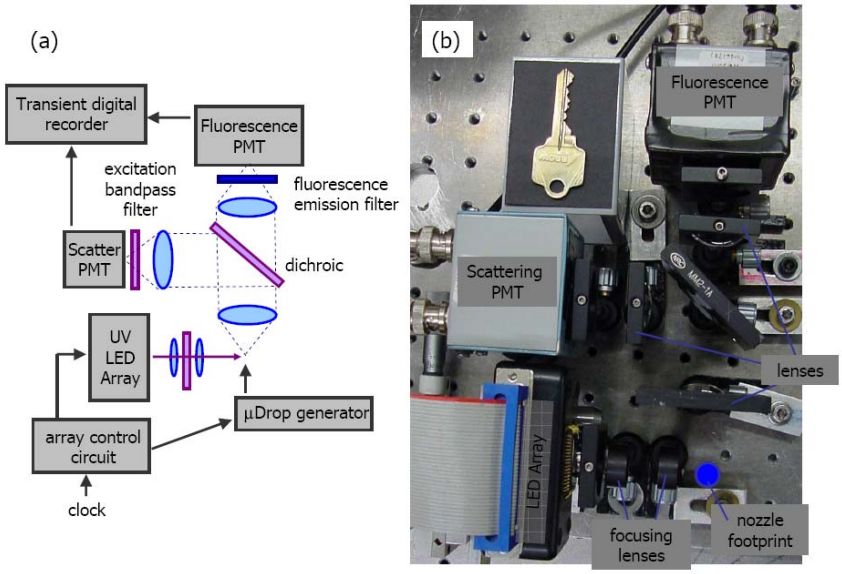

Figure 5.17 : Schematic of a filter-based fluorescence detection apparatus.

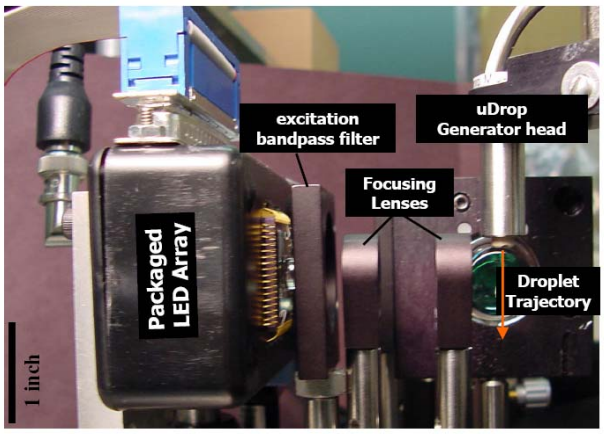

Figure 5.18 : Close-up image of a packaged LED array in the optical setup.

The geometry of light collection is limited due to the large LED background, hence the collection optics are located at right angles to the incident beam. A dichroic filter is used to separate and redirect the scatter and fluorescence signals. Two PMTs, with additional filters to isolate the scatter and fluorescence wavelengths, capture single-particle data. The filter for the scatter channel is a duplicate of the excitation filter, and the fluorescence emission filter corresponds to either NADH (390 nm longpass) or tryptophan (305 nm longpass) emission. **Figure 5.19** contains raw fluorescence channel recordings from *single* wet particles doped with either NADH or tryptophan and acquired under illumination from a 340 nm or 290 nm linear LED array respectively. The sequential flashing of each array element is identifiable; the failure of a 340 nm LED element in **(a)** makes this particularly clear. Scatter data is recorded simultaneously and serves as a means to normalize the fluorescence data by removing particle size dependences and correcting for possible deviations of a particle from the illumination volume during its trajectory. For example, particles may have slightly different velocities or may be traveling in a trajectory that is at the edge of the 200 um illumination width, effects that are aggravated by the long particle tracking distance of approximately 3 mm. Total fluorescence and scatter signals are obtained by integrating the data over the approximately 2.5 msec of illumination time, which corresponds with the wet particle velocity measured above. As a means to characterize the system response, a ratio of the total fluorescence and scattering signals (F/S) is determined as a function of fluorophore concentration in similarly sized doped water droplets; shown in **Figure 5.20**. Part **(a)** is a F/S ratio comparison between systems using 370 and 340 nm LED array excitation; the factor of 2 reduction in response is expected from the NADH absorbance, recall **Figure 3.1**. In part **(b)**, the indicated background level reflects the signal measured from undoped water droplets and represents leakage of light into the fluorescence channel. We note that the fluorescence increases sublinearly with tryptophan concentration above 0.1%, an effect which has been observed by others [17], and which may be attributed to self-quenching as the concentration approaches the solubility limit of tryptophan in water.

In the case of a 290 nm (340 nm) LED array, each element is pulsed for 70 usec with a bias of 20 mA (40 mA), yielding an output power of approximately 45 uW (1 mW) immediately following the hyperhemispherical lens. From the F/S ratios, this spectral-filter based scheme is shown to be capable of detecting NADH concentrations of 0.01 wt % (140 uMolar) and tryptophan concentrations below 0.0025 wt % (125 uMolar) with modestly performing UV LED arrays. A connection between this detection sensitivity and that required *in the field* is addressed at the end of this chapter.

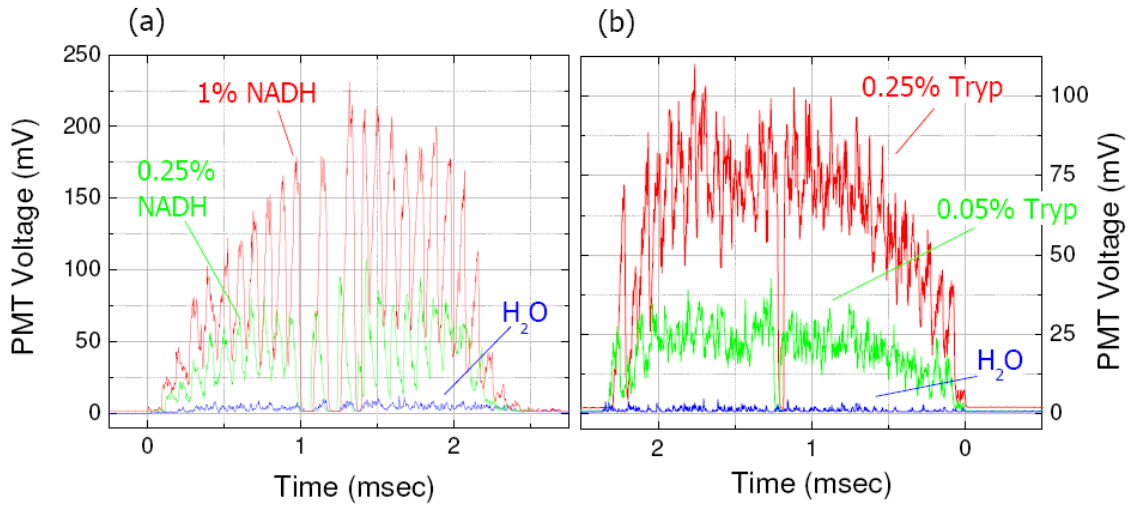

Figure 5.19 : Single-particle fluorescence channel recordings.

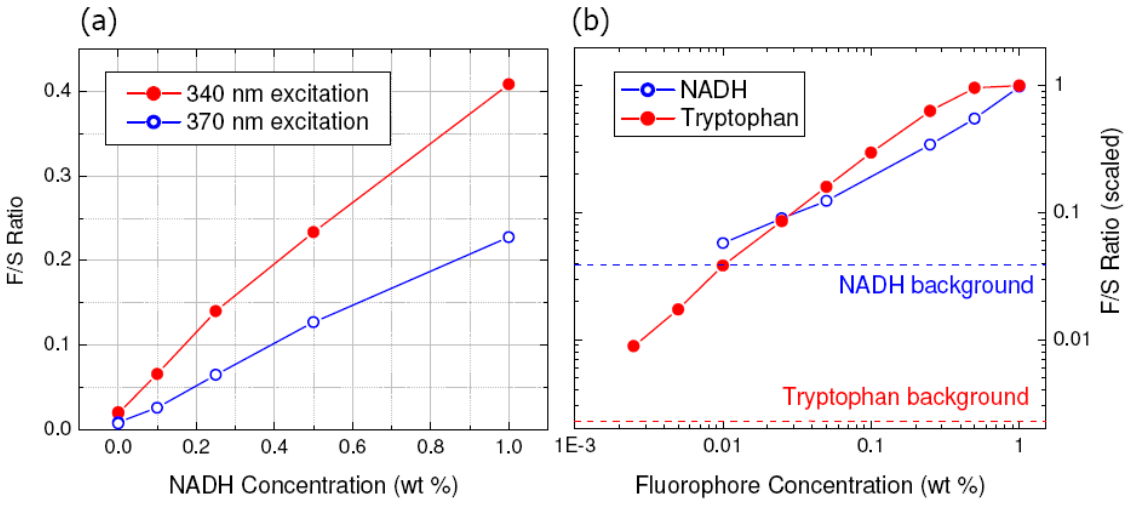

Figure 5.20 : Fluorescence to scatter (F/S) ratios.

5.4.2. Compact spectroscopic apparatus

Figure 5.21 illustrates the optical setup for a 32-point, particle in-flight, spectroscopic fluorescence detection strategy. The array and imaging optics are identical to the filter-based scheme, however, the system has a slightly larger footprint of approximately 25 x 35 cm. Also, in this case a 635 nm LD is focused to the jetstream immediately emerging from the nozzle, and an associated PMT with a red bandpass filter (630nm center, 40nm bandwidth) serves as a trigger to indicate the presence of a particle in the system and cue the timing electronics. This feature anticipates the use of the system with dry particles sampled from the ambient which, unlike the water droplets which are generated on demand and require no additional indication of their presence in the system, are not artificially generated and arrive at random times.

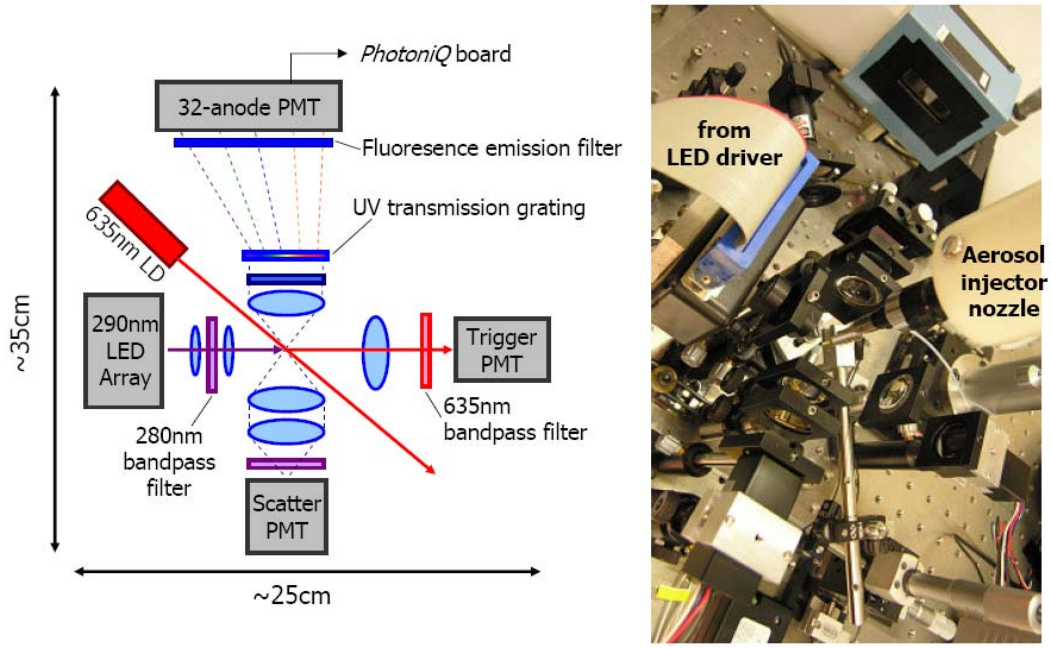

Figure 5.21 : Optical setup for spectroscopic fluorescence detection.

As in the filter-based system, fluorescence collection is at right angles to the incident LED illumination so as to reduce the amount of background light. Scatter at the LED wavelength is collected by a pair of plano-convex lenses and a simple PMT. The fluorescence channel consists of a collection lens, an LED-scatter blocking filter and a fluorescence emission filter; a UV transmission grating (Optometrics LLC, 3-9814) is used to spectrally disperse the light onto a 32-anode PMT (Hamamatsu, H7260). The main advantages of using a PMT are that it has much higher gain and sensitivity compared to other detectors such as CCD cameras or avalanche photodiodes, and in addition, it is capable of operating at high speeds. This specific PMT has a gain of 10^6, a healthy cathode radiant sensitivity at wavelengths as low as 275 nm, and a low dark current (0.5 nA) such that it is capable of single photon detection. Compared to a commercial CCD-based spectrometer for instance, its main disadvantage is the low spectral resolution since each of the 32 channels corresponds to a bandwidth of approximately 10-15 nm. On the other hand, the fluorescence signals of interest are quite broad and 32-point spectra do not lack any critical information, while still providing more spectral data than the simple filter-band approach. It was found that the choice of a transmission grating offers greater flexibility in optical geometry than a concave holographic grating, in part due to the large background LED emission which is avoided by placing the collection optics at a right angle to the LED illumination. Placed directly in front of the multi-channel PMT (MC-PMT), the fluorescence emission filter is used to block scattered 635 nm light from the LD and scattered LED light while passing the fluorophore fluorescence band. In the case of the 340 nm LED, the same filters described above were used, however, in the case of the 290 nm LED, a single commercial filter with this capability could not be found, and an additional LED-scatter blocking filter is required. A piece of filter glass (360 nm center, 160 nm bandwidth) blocks the LD light, followed by a 305 nm longpass filter to block the LED scatter.

The collection lens (focal length *f*) is placed a distance between *f* and 2*f* away from the particle stream. This produces a magnified image of the fluorescence line at the MC-PMT, and the light passing through the transmission grating is therefore not collimated. Due to the large spectral width (~ 10-15 nm) in each channel of the PMT, this arrangement is deemed not to contribute to any significant error and is employed because of its simplicity. As a demonstration of the compact spectrometer alone, **Figure 5.22** shows a series of fluorescence spectra acquired by illuminating NADH and two strains of BG spores located on a static substrate with a single-element 340 nm LED.

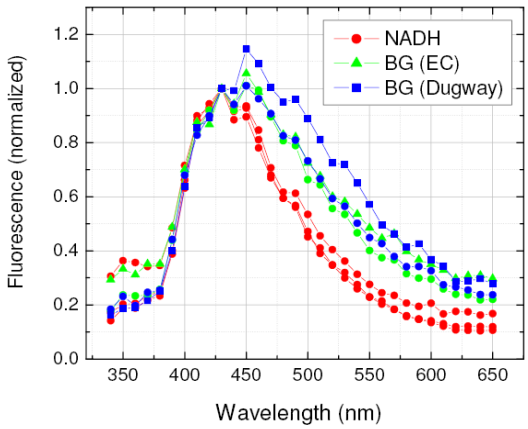

Figure 5.22 : Fluorescence from static BG spores acquired with a compact spectrometer.

At this point it is clear that the LED-based fluorescence system requires considerable control circuitry. A further complication which has not yet been addressed is that the data acquired from each particle must be analyzed on-the-fly so that the particle deflector located downstream can be selectively triggered to remove suspect particles. The details of the deflector itself are reserved for **Section 5.5**, but the control electronics are described here first. **Figure 5.23** illustrates the basic timing sequence of events to be executed upon entry of a particle into the jetstream. The presence of the particle is first detected as a pulse in the red LD scatter PMT, and timing of all subsequent events is tied to this trigger. A trigger is generated with a fixed delay corresponding to the time it takes the particle to travel from the LD focus to the first LED element.

This initiates the sequential firing of the LED array and at the same time starts spectral acquisition from the MC-PMT. The integration window for the MC-PMT is closed after the last LED fires. Finally, based on the results of an algorithm which is applied to the optical data just acquired, a trigger to the deflector may be generated.

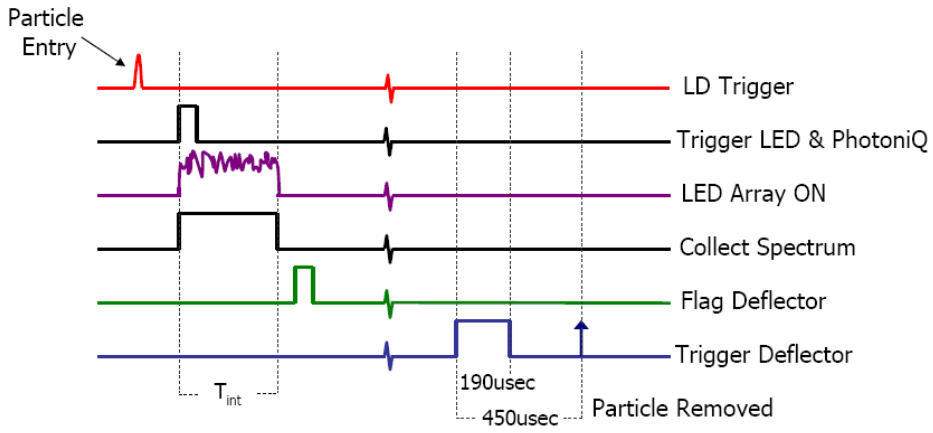

Figure 5.23 : Event sequence in the LED array-based warning system.

To achieve the required timing and control sequence, 3 electronics boards were custom built by Vtech Corporation [18]. The central PhotoniQ-3G iQSP480 board is a commercial product whose primary function is to acquire and process the real-time fluorescence data from the 32-anode MC-PMT and trigger the particle deflector based on a spectral algorithm applied to the fluorescence data [19]. The functionality of the iQSP480 has been expanded for the unique purpose of this system by the integration of two additional boards; one to drive the LED array current pulsing and the other to control and monitor more than a dozen other signals. A tailored PC-based graphical user interface (GUI) gives user control and programmability, particularly useful for testing, however the electronics is designed such that it is capable of standing alone in a portable system. The front panel of the GUI is displayed in **Figure 5.24**. Fluorescence collected by the MC-PMT is evaluated by a spectral algorithm running on the DSP (digital signal processor)

in the iQSP480. Owing to the finite time that the particle is in the jetstream, signal collection and evaluation of the algorithm must be done in real time. This is possible because the decision circuitry resides in the DSP and not in the PC. Furthermore, the DSP may be easily reprogrammed through a USB 2.0 interface to accommodate different spectral algorithms. The electronics is designed with a view towards a standalone sensor and thus supports many more I/O channels than described here or used in the experiments elsewhere in this thesis; for example, additional red LDs and PMTs for monitoring the particle before and after a deflection event, and photodiodes for tracking the health of the UV LEDs.

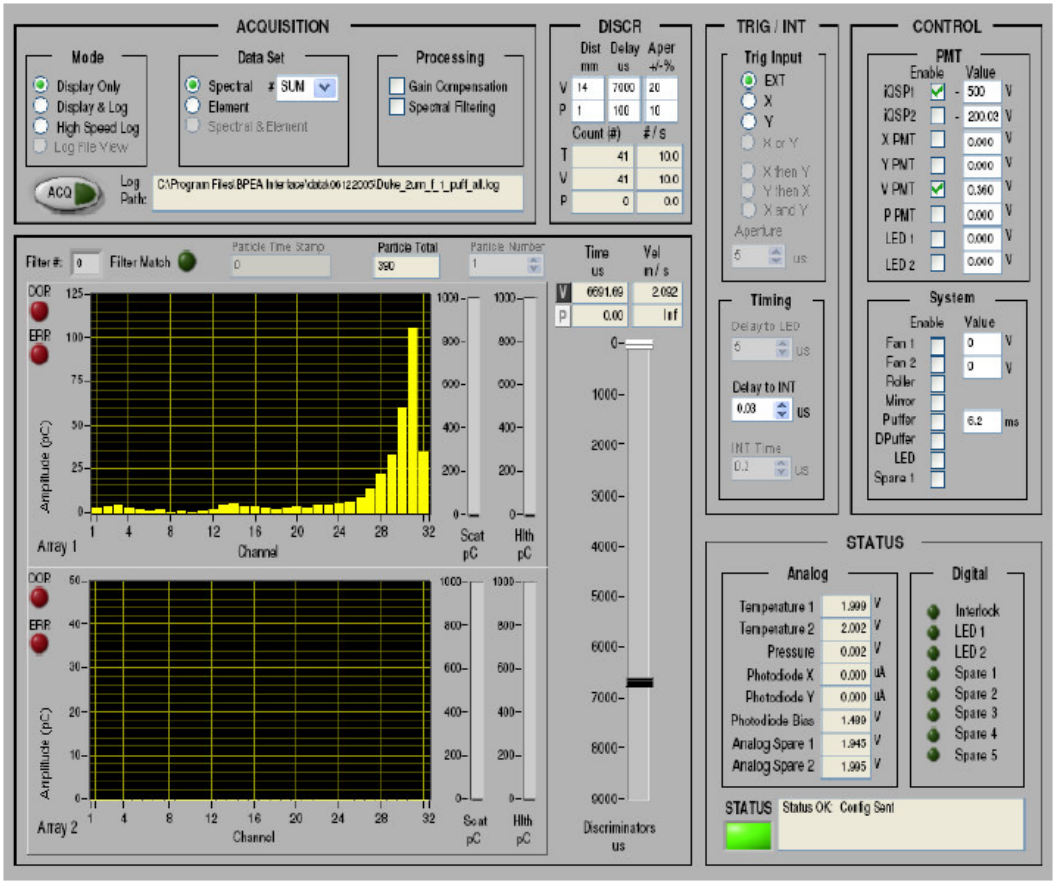

Figure 5.24 : GUI display for control of LED array system electronics.

5.4.3. Real-time fluorescence spectra from wet particles

As with the filter-based experiments, a range of concentration in fluorophore-doped water droplets from the MicroDrop generator was used to test the full spectroscopic system. **Figure 5.25** shows two examples of real-time fluorescence spectra acquired from 10 sequential single drops. Part **(a)**, from 0.05 wt % NADH-doped drops excited with a 340 nm LED array, illustrates the noisiness of the signal as the detection limit is approached. Given the dark current per channel of the photon-counting MC-PMT, a fluctuation of several pC in the charge collected over the 2.5 msec particle fly-by time may be attributed to the detection limit of the PMT. In contrast, part **(b)** shows the relatively bright fluorescence from 0.5 wt % tryptophan-doped drops excited with a 290 nm array. The range of concentrations tested is illustrated in **Figure 5.26 (a)** which shows the fluorescence spectra averaged over 100 sequential drops for various NADH concentrations. In all spectral data presented, wavelength calibration of the 32 MC-PMT channels uses the LED scatter signal acquired by temporarily removing the fluorescence emission filter (black curve). The remaining channels are assigned a wavelength based on a linear interpolation between the first and second order diffraction peaks arising from the transmission grating. **Figure 5.26 (b)** shows averaged spectra from 0.5 wt % tryptophan-doped drops illuminated by a 290 nm LED with (F) and without (F+S) the additional LED-blocking emission filter. Since this is the only filter which has a sharp cutoff near the tryptophan emission band, this plot dispels the possible concern that the resulting fluorescence emission spectrum is distorted by the chosen filter set.

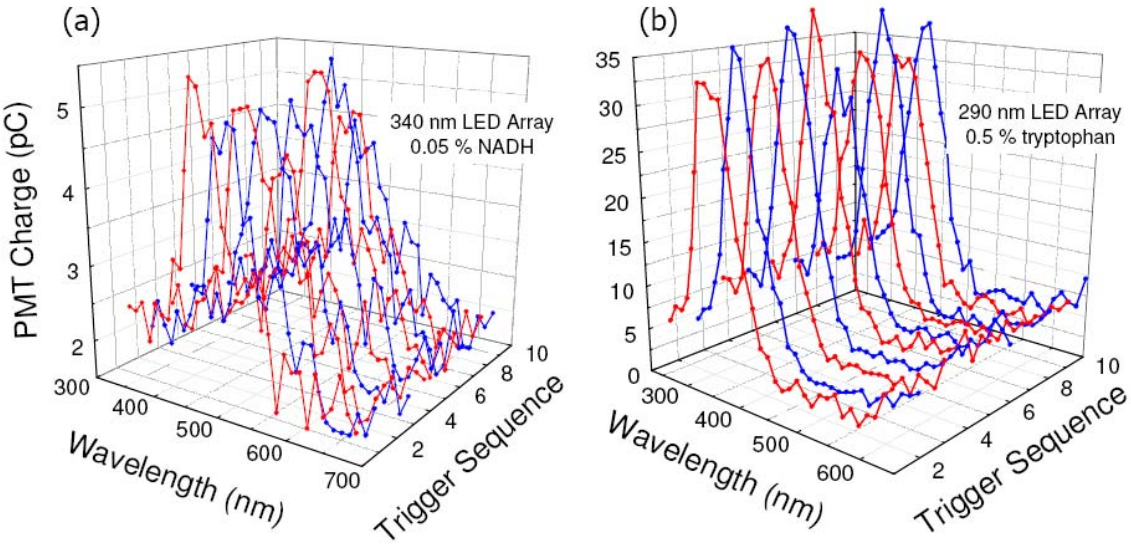

Figure 5.25 : Real-time fluorescence spectra from single particles.

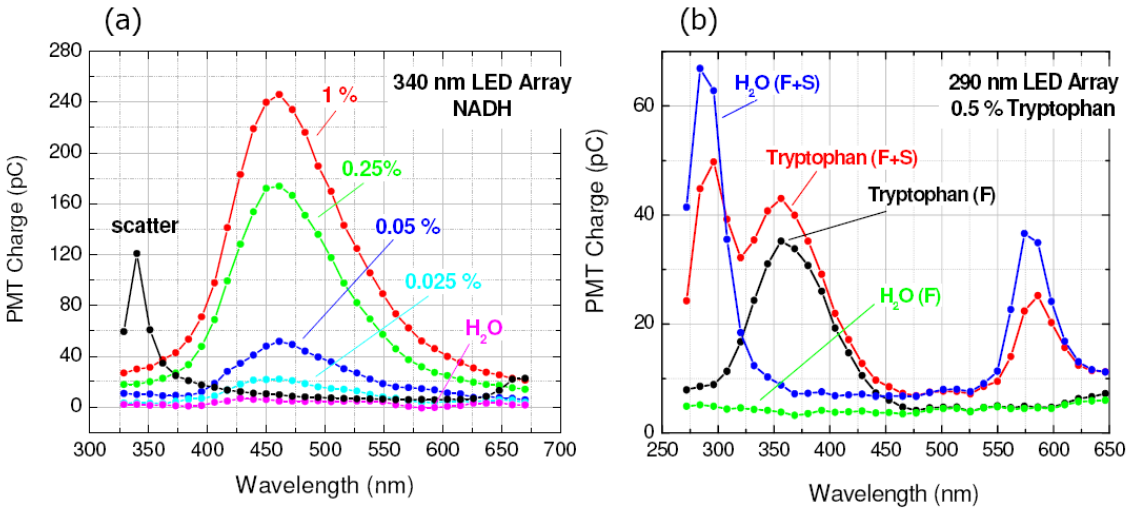

Figure 5.26 : Averaged fluorescence spectra from doped microdrops.

5.4.4. Real-time fluorescence spectra from dry particles

Equipped with evidence of the ability of the compact spectroscopic apparatus to excite and acquire fluorescence from airborne particles in real-time, a more realistic simulation of ambient particles is undertaken. Dry particles with a speed of approximately 9 m/sec are generated using an air flow rate of 0.8 L/min applied to the drying column. Although a slower speed would be advantageous by providing a longer illumination time and hence delivering a larger total excitation energy, when the air speed is reduced the particles begin to be deposited on the walls of the column and the particle flow is no longer stable. **Figure 5.27** contains fluorescence spectra from 10 sequential dry tryptophan particles excited by a 290 nm LED array. These 6 um diameter particles are dried from 0.5 wt % water drops and thus contain the same total number of tryptophan molecules as the spectra shown in **Figure 5.25 (b)**; the peak intensity is reduced by approximately 15-20 times in going from wet to dry particles. This factor is only partially attributed to the reduction in illumination time from just over 2 msec down to 350 usec. Another possible cause is the inner filter effect, or the efficient excitation of tryptophan at the surface of the particle such UV excitation does not penetrate through the dense dry particle and hence not all molecules are fluorescing. **Figure 5.27 (b)** is a scaled cartoon of a single LED element (50 um x 200 um) and the dry particle, emphasizing that only a small fraction of the light from the LED array impinges onto the particle. This is another contributor to the discrepancy between wet and dry particles. Although a narrower LED would be better matched the size of an individual spore, subsequent particles in the jetstream would not be illuminated. An important requirement for an aerosol sensor is that it analyze as many particles as possible, and the 200 um array width is matched to the jetstream emerging from the particular nozzle designed for this sensor. It is feasible to fabricate smaller nozzles which generate more focused jetstreams, however, the particle speed required to sample the same volume of air scales as the inverse of the diameter squared. Hence, the choice of aperture size is another balance between efficient use of

generated photons, total light delivered to the particle and the overall system performance in terms of aerosol particle throughput.

The fluorescence spectrum is not entirely clear from the weak single-particle data, however, an average over 500 sequential dry particles plotted in **Figure 5.28 (a)** shows an unambiguous tryptophan fluorescence signature compared to the background collected with no particle present. Alignment of the optical system and adjustment of the timing electronics is accomplished by maximizing the signal at the scatter PMT, which is much stronger than the fluorescence spectrum. **Figure 5.28 (b)** shows a particle being detected by elastic scatter from a red LD and the LED being fired 150 usec later, corresponding to the first element being located approximately 1 mm downstream. Although the optical hardware exists to collect simultaneous LED-derived scatter with which to normalize out non-uniformities in the fluorescence, as is done in the simple filter-based system, the algorithm to do this is on-the-fly is in development and none of the fluorescence spectra shown have been normalized.

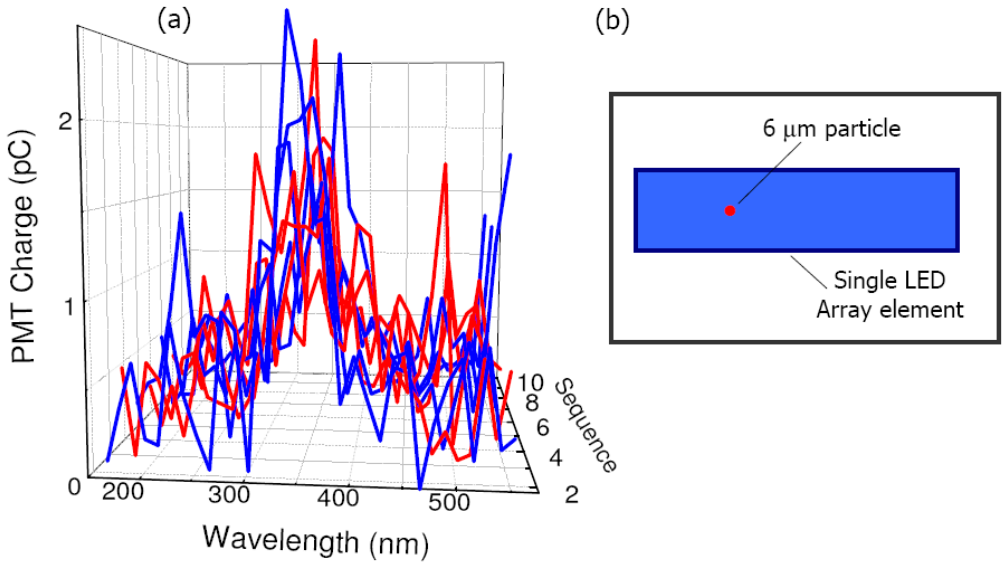

Figure 5.27 : Fluorescence spectra from single 6 um diameter dry tryptophan particles.

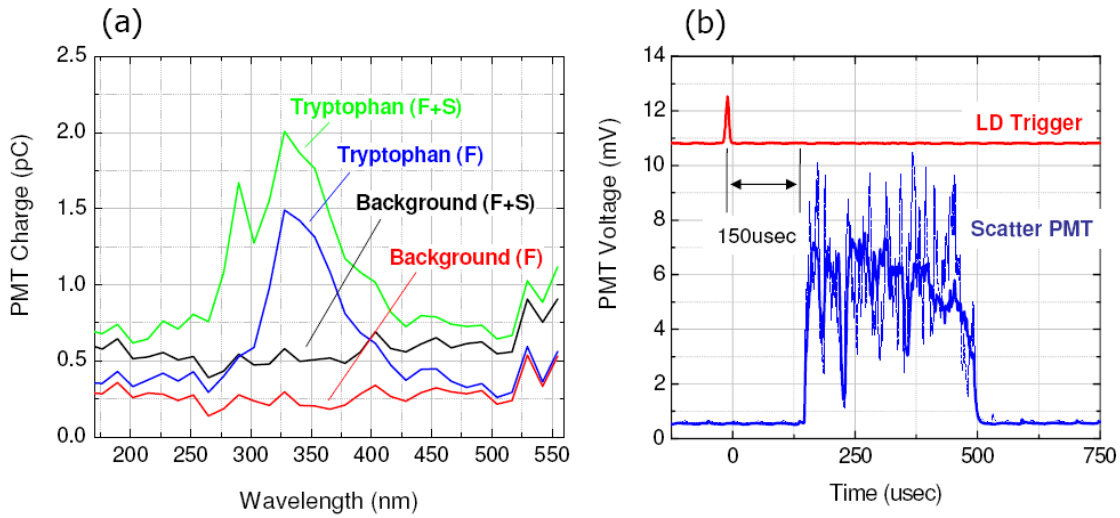

Figure 5.28 : Fluorescence spectra and scatter from dry tryptophan.

As a summary of the spectroscopic detection system, **Figure 5.29** compares the average fluorescence collected from **(a)** wet and **(b)** dry tryptophan illuminated by a 290 nm LED array. In both cases the particles are generated from 0.5 wt % doped drops. The upper trace in part **(a)**, with a visible second-order peak from the diffraction grating arising from elastically scattered light, was acquired without the additional LED-scatter blocking filter. This verifies that the fluorescence lineshape, shown in the lower trace with the filter, is minimally distorted by the chosen emission filters. The error bars show the standard deviation of the signal as measured over 100 nominally identical water droplets. Part **(b)** is an average over 500 sequential dry particles and very clearly exhibits the same fluorescence lineshape as the brighter wet particles.

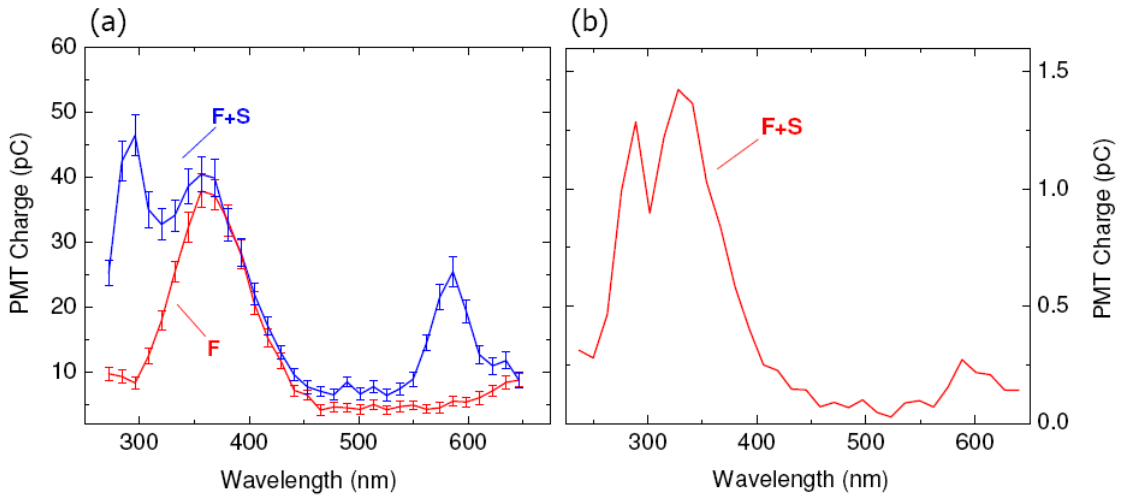

Figure 5.29 : 290 nm LED array excitation of (a) wet (b) dry tryptophan particles.

5.4.5. Connection to bacterial spores

Table 5.1 lists the lowest detected concentration of each fluorophore by the system employing UV LED excitation. Due to the complication of not being certain how many molecules are fluorescently active in the dry particle case, the detection limit is quoted from wet particle results. In order to reconnect with genuine a bio-aerosol, recall from **Chapter 3** that a BG spore contains approximately 10^8 tryptophan molecules. Thus, the detection limit of the current 290 nm LED array-based system corresponds to roughly 50 spores. This is a measure of considerable success for a compact point-sensor based on emerging UV LEDs; for example, in comparison to the number of anthrax cells required for human infection, which is on the order of 10 000 [20]. Although clearly the total system performance is subject to the fraction of air sampled and average spore content per particle among other caveats. In order for the UV LED system to directly compete with high-end solid-state laser-based systems having single spore detection capability, an order of magnitude improvement in detection sensitivity is required. In

the case of the spectroscopic system, the sensitivity is limited by the MC-PMT dark current, hence this requirement translates to an order of magnitude increase in LED output power. Advances in material quality are expected to yield significant improvements in device performance over the next several years. Nonetheless, a direct comparison to laser-based systems is not entirely justified since compact LED sensors offer a unique set of advantages.

LED λ	fluorophore	concentration (wt %)	# of molecules
340 nm	NADH	0.01	~ 10^{10}
290 nm	tryptophan	0.0025	~ $5x10^{9}$

Table 5.1 : Concentration of fluorophores detected using UV LED array excitation.

Firstly, the presence of a single spore is not cause for alarm, but rather an elevated number of spores in the atmosphere compared to that in the typical background. A number of front-end bio-aerosol sensors work on this principle of measuring an overall increase in suspicious fluorescence (for example, see [21]). Clearly, this method is also subject to statistics associated with the fraction of particles within a volume of air that must be sampled and analyzed by the system in order to detect a dangerous number of pathogens. Provided that we average the fluorescence measured over suspicious particles, as was shown for the dry particle case where the individual spectrum was extremely noisy, the LED-based system has the potential to perform much better than suggested by **Table 5.1**. Furthermore, the fundamental advantage of the LED-based system over traditional laser-based systems is its small size and potentially lower cost. This opens the possibility of creating sensor networks to map aerosol dissemination over a larger physical area where the performance of the networked system is improved over the single unit through this increase in information. An investigation of the performance of such a network is beyond the scope of this work, and instead we chose to pursue a method to improve upon the spectroscopic detection of a single particle in an individual sensor.

Limits quoted above are extremely modest for the reason that they were determined essentially by visual appearance of the spectrum of a single event. The development of a spectroscopic sorting algorithm will provide a better determination of the detection limit. Furthermore, to verify that the algorithm is correctly identifying one species versus another, the particles must be separated after identification and checked by other means. To that end, in the following section we integrate a compact particle deflector with the front-end LED system in order to physically sort samples based on the spectra acquired in real-time.

5.5. Particle sorting

In addition to providing a direct measure of the success of the optical system and fluorescence algorithm in identifying classes of particles, physically sorting aerosol particles is a useful capability for a front-end sensor. By reducing the background particle burden and providing a suspicious-particle enriched sample it improves the prospects for many second-stage biochemical analyses. Only one reported LIF bio-aerosol sensor – that pioneered by our colleagues at Yale – has incorporated a particle deflector and has been demonstrated to provide up to 10^3 enrichment in suspect particles with respect to the background [22, 23]. In this case, the instrument to aerodynamically deflect particles is bulky and therefore not amenable to use with our miniaturized sensor design. As an alternative, we employ a solenoid-based aerodynamic deflector. When energized by a current pulse an electromagnetic plunger opens the valve, causing a burst of nitrogen gas which lasts for approximately 250 usec. The response time of the valve, which is returned to the closed position by a spring, means that the deflector may be fired at a rate of up to 1200 Hz. The physical size of the cylindrical deflector, about 0.25” in diameter and 1.5” long, is commensurate with integration into the compact optical and electronic system being developed. **Figure 5.30** shows a close-up of the aerodynamic deflector located in the path of particle jetstream.

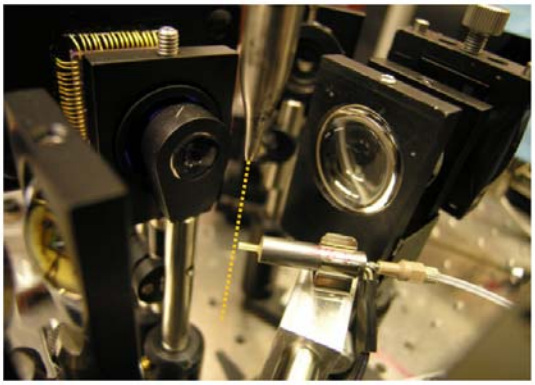

Figure 5.30 : Close-up photograph showing the aerodynamic deflector and nozzle.

For demonstration, dye-filled polystyrene latex spheres (PSL) are used as simulants of bio-fluorescence. Two types of PSL are used, 1 um diameter blue fluorescing (Molecular Probes, F8815) and 2 um green fluorescing (Duke Scientific, XPR-801). Both are readily excited by 340 nm light, hence all experimental data shown use a 340 nm linear array of LEDs as the excitation source. The spheres are diluted to known concentrations in water and the solution is ejected by the MicroDrop generator at a rate of 10 Hz. The concentrations are chosen such that the particles consist of water with statistically less than 1 PSL per drop. PSL spheres, as opposed to amino-acid mixtures such as tryptophan and NADH, are useful characterization tools as they are present in discrete quantities (ie. 0, 1 or 2 PSL per drop) and can be counted on the substrate to verify experimental results. Particles are collected onto a glass structure made from microscope coverslips, which is placed 2 mm below the deflector nozzle as illustrated in **Figure 5.31**. If the fluorescence spectrum is deemed 'suspicious' according to the algorithm in the DSP, the electronics records a flag event and sends a trigger to the aerodynamic deflector in order to remove the particle from the jetstream. Deflected particles are deposited onto the vertical portion of the structure and remain in position by electrostatic force, while the undeflected jetstream accumulates on the horizontal glass.

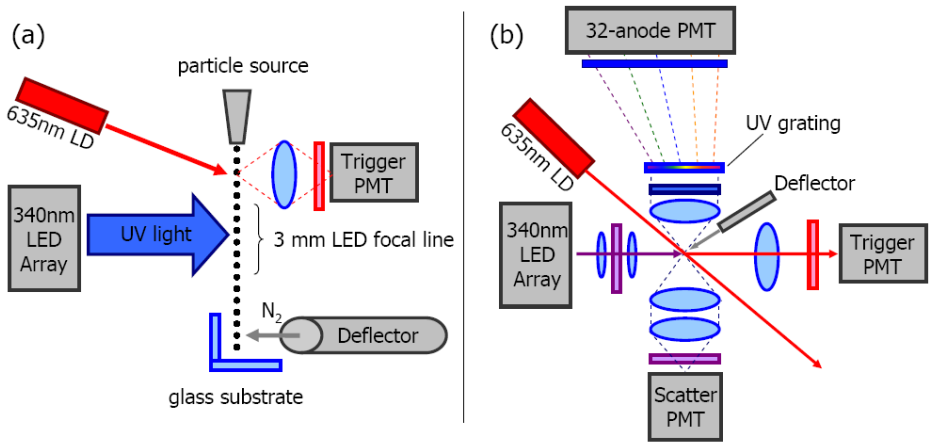

Figure 5.31 : (a) Front and (b) top view illustration of the aerodynamic deflector position.

For the data shown below, the drive current pulse per LED element is a modest 20 mA for a duration of 53 usec corresponding to 0.3 mW output power per element at the source. The control electronics are modified to drive 2 adjacent devices on at any time. The block of 2 LEDs as opposed to a single LED increases the overall light delivered to the particle, and hence the resulting fluorescence, by reducing the in-between time. It also tolerates slight mismatching of the LED firing rate to the particle velocity. **Figure 5.33 (a)** is a portion of the PC display that shows the UV scatter intensity detected per element of the LED array. Intensity differences over the 32 LEDs are due to imaging optics, which contribute to center elements being better focused, and to element-to-element variation in device characteristics. **Figure 5.33 (b)** summarizes a series of demonstrations. Either blue-doped or green-doped PSL were separately passed through the system and a simple one-spectral-band algorithm was used to evaluate whether a particle was present or not. In this case, a flag to the deflector was generated upon the condition that the average charge collected over a 35 nm wide spectral range centered about the peak fluorescence

(525 nm and 435 nm for the green and blue PSL respectively) was greater than a threshold level of 1 pC. The threshold was chosen to lie above the background level - due to detector noise and stray LD light - of roughly 10 photons per PMT channel accumulated during the total 1.6 msec fluorescence collection time, the time during which the particle traverses the LED array focal line. Shown in **(b)** are the average fluorescence spectra of flagged events during a test of 5000 particles; commensurate with the PSL concentration, nearly 200 particles were flagged to create each plot. A solution containing a mixture of both types of PSL was also tested, statistically approximately 0.1 green and 0.05 blue PSL spheres per drop, and a one-band algorithm to isolate the green particles was applied. In addition, a two-band algorithm where the same wavelength bands were used but where a flag was generated only upon the boolean condition (green = true) AND (blue = false) was used in order to eliminate the possibility of highly fluorescent blue particles, or clusters, from tripping the green flag. **Figure 5.32** contains the noisy single-particle fluorescence spectra from the mixture and indicates the particles which have been flagged as green.

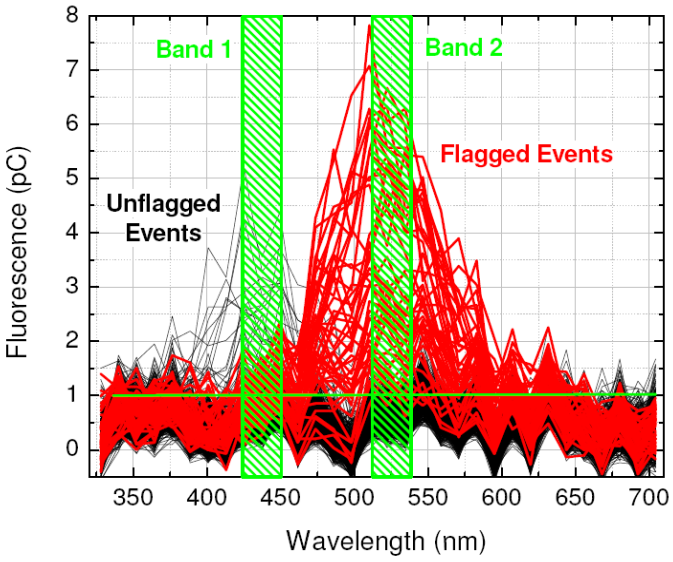

Figure 5.32 : Raw fluorescence spectra from a mixture of PSL-doped particles.

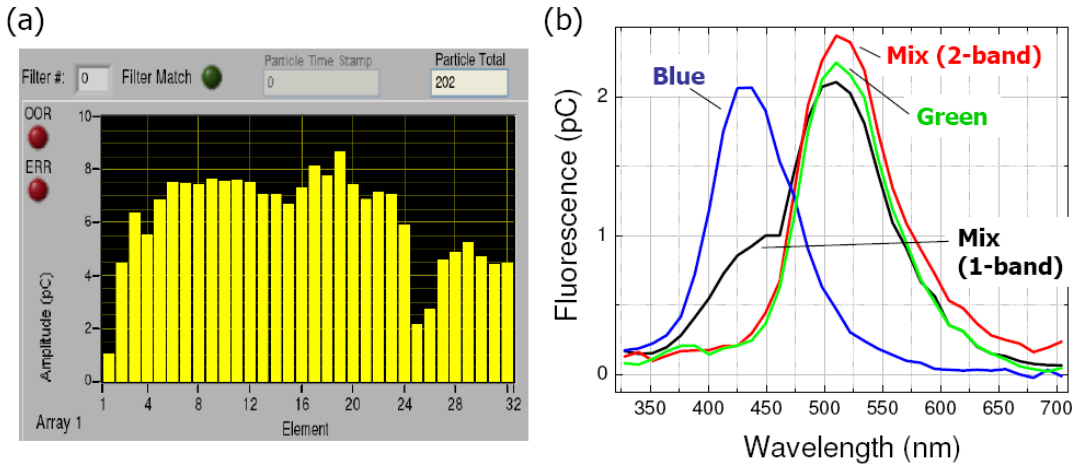

Figure 5.33 : (a) Scatter intensity and (b) fluorescence averaged over flagged PSL.

Results of the algorithm were used to trigger the mini-aerodynamic deflector located downstream from the LED array illumination, a distance corresponding to approximately 6 msec after the particle entered the optical system. **Figure 5.34** is an epi-fluorescence image of the deflected and undeflected aggregates of spheres in the case where green PSL were selected using the two-band algorithm. In this configuration, the area containing deflected particles is smaller than 250 um in diameter. Among 5000 doped water droplets, 185 were flagged as having green fluorescence. Counting deflected particles yields nominally 180 green and 8 mistakenly removed blue ones. The particle generation rate was such that successive water droplets were well separated in space and hence unaffected by gas bursts intended for adjacent particles. Thus, deflected blue particles indicate that the algorithm targeted to green particles yielded a flag for a blue one, or that clusters of multiple PSL were present in a single water drop. However, undeflected particles are exclusively blue, hence no 'suspicious' (green) particles were falsely categorized as 'safe' (blue), indicating that upon receipt of a trigger the deflector is extremely reliable in removing suspect particles from the jetstream. Thus, the implementation of a simple algorithm results in a system which is capable of single-particle identification from extremely weak fluorescence spectra.

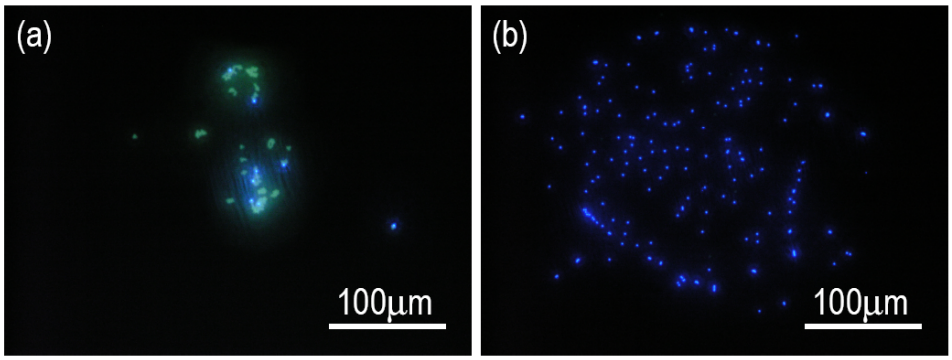

Figure 5.34 : Epi-fluorescence images of (a) deflected and (b) undeflected PSL spheres.

It is expected that further improvement in the particle concentration ratio may be achieved with refined algorithms. At this level, the contribution of UV LEDs has been demonstrated, while what remains is the development of algorithms to discriminate suspicious bio-aerosols from common background interferents using real-time spectroscopic data. The routine will be highly dependent on the particular pathogen and nature of the background particles, and is in fact its own field of study [24-26].

Summary

With the demonstration of a miniaturized aerodynamic deflection technique, we complete the design of compact components for the bio-aerosol sensor illustrated in **Figure 5.1**. All of the fundamental elements in a traditional LIF sensor are replaced with smaller and potentially more cost-effective alternatives; application of emerging UV semiconductor light emitters and use of novel detector arrangements enables compaction of the core optical arrangement, in conjunction with custom-designed real-time electronics and a miniaturized aerodynamic deflector, the entire system is significantly reduced in size. While there remains considerable room – and need – for improvement in UV LED efficiency, the use of both 340 nm and 290 nm LEDs featuring a flexible LED array design, reflects the maturation of the concepts behind a next generation of compact bio-warning systems which access key biological fluorophores.

References

1. K. Davitt, Y.-K. Song, A. V. Nurmikko, S.-R. Jeon, M. Gherasimova, J. Han, Y.-L. Pan and R. K. Chang. Phys. Stat. Sol. (c), 2005. **2**(7): p. 2878-2881.
2. K. Davitt, Y.-K. Song, W. R. Patterson III, A. V. Nurmikko, M. Gherasimova, J. Han, Y.-L. Pan and R. K. Chang. Opt. Express, 2005. **13**(23): p. 9548-9555.
3. K. Davitt, Y.-K. Song, W. R. Patterson III, A. V. Nurmikko, Y.-L. Pan, R. K. Chang, J. Han and M. Gherasimova. In preparation, 2006.
4. P. H. Kaye, W. R. Stanley, E. Hirst, E. V. Foot, K. L. Baxter and S. J. Barrington. Opt. Express, 2005. **13**(10): p. 3583-3593.
5. V. Sivaprakasam, A. L. Huston, C. Scotto and J. D. Eversole. Opt. Express, 2004. **12**(19): p. 4457-4466.
6. R. Defreez. *Ultraviolet Laser Inducted Fluorescence Detection of Biological Aerosol Agents*. in *CLEO*. 2004. San Francisco.
7. S. C. Hill, R. G. Pinnick, S. Niles, Y.-L. Pan, S. Holler, R. K. Chang, J. Bottiger, B. T. Chen, C.-S. Orr and G. Feather. Field Anal. Chem. Technol., 1999. **3**(4-5): p. 221-239.
8. H. Peng, E. Makarona, Y. He, Y.-K. Song, A. V. Nurmikko, J. Su, Z. Ren, M. Gherasimova, S.-R. Jeon, G. Cui and J. Han. App. Phys. Lett., 2004. **85**(8): p. 1436-1438.
9. J. R. Lakowicz, H. Szmacinski, K. Nowaczyk and M. L. Johnson. Proc. Natl. Acad. Sci., 1992. **89**: p. 1271-1275.
10. R. A. Dalterio, W. H. Nelson, D. Britt, J. Sperry, D. Psaras, J. F. Tanguay and S. L. Suib. Appl. Spectrosc., 1986. **40**(1): p. 86-90.
11. Y.-L. Pan, V. Boutou, R. K. Chang, I. Ozden, K. Davitt and A. V. Nurmikko. Opt. Lett., 2003. **28**(18): p. 1707-1709.
12. M. Khizar, Z. Y. Fan, K. H. Kim, J. Y. Lin and H. X. Jiang. Appl. Phys. Lett., 2005. **86**: p. 173504-3.

13. C.-C. Kao, H.-C. Kuo, H.-W. Huang, J.-T. Chu, Y.-C. Peng, Y.-L. Hsieh, C. Y. Luo, S.-C. Wang, C.-C. Yu and C.-F. Lin. IEEE Photon. Tech. Lett., 2005. **17**(1): p. 19-21.

14. J. Mohn, Y.-L. Pan, K. Aptowicz, A. Nurmikko and R. K. Chang, *A Comparison of Optical Systems for Illuminating Flowing Aerosols by a Linear Array of LEDs.*, unpublished work (private communication).

15. Y.-L. Pan, J. Hartings, R. G. Pinnick, S. C. Hill, J. Halverson and R. K. Chang. Aerosol Sci. Technol., 2003. **37**: p. 628-639.

16. J. R. Bottiger and P. J. DeLuca, *Low Concentration Aerosol Generator*. 1999, United States Patent No. 5,918,254.

17. S. C. Hill, R. G. Pinnick, S. Niles, N. J. Fell Jr., Y.-L. Pan, J. Bottiger, B. V. Bronk, S. Holler and R. K. Chang. Appl. Opt., 2001. **40**(18): p. 3005-3013.

18. Vtech Engineering Corporation, *www.vtechcorp.com*.

19. Y.-L. Pan, P. Cobler, S. Rhodes, A. Potter, T. Chou, S. Holler, R. K. Chang, R. G. Pinnick and J.-P. Wolf. Rev. Sci. Instrum., 2001. **72**(3): p. 1831-1836.

20. C. A. Primmerman. Lincoln Lab. J., 2000. **12**(1): p. 3-32.

21. A. Birenzvige, J. Eversole, M. Seaver, S. Francesconi, E. Valdes and H. Kulaga. Aerosol Sci. Technol., 2003. **37**: p. 210-220.

22. Y.-L. Pan, V. Boutou, J. R. Bottiger, S. S. Zhang, J.-P. Wolf and R. K. Chang. Aerosol Sci. Technol., 2004. **38**: p. 598-602.

23. Y.-L. Pan, P. J. Cobler, S. A. Rhodes, J. Halverson and R. K. Chang. SPIE Optically Based Biological and Chemical Sensing, 2005. **5990**: p. 59900Y1-4.

24. P. C. Gray, I. R. Shokair, S. E. Rosenthal, G. C. Tisone, J. S. Wagner, L. D. Rigdon, G. R. Siragusa and R. J. Heinen. Appl. Opt., 1998. **37**(25): p. 6037-6041.

25. Y. S. Gheng, E. B. Barr, B. J. Fan, P. J. Hargis Jr., D. J. Rader, T. J. O'Hern, J. R. Torczynski, G. C. Tisone, B. L. Preppernau, S. A. Young and R. J. Radloff. Aerosol Sci. Technol., 1999. **30**(2): p. 186-201.

26. M. W. Mayo, S. C. Hill and R. K. Chang, *Fluorescence of bacteria, pollens and naturally occurring airborne particles: excitation / emission spectra*, Unpublished work.

CHAPTER 6

UV LDS FOR BIOAEROSOL SENSING

Light-emitting diodes will always be spatially and spectrally incoherent light sources and thus any application must contend with these properties. In the previous chapter, the use of emerging wide bandgap nitride-based LEDs provides access to the UV wavelengths required in a bio-aerosol sensor while reducing the size and potential cost with respect to existing solid-state laser-based systems. Semiconductor laser diodes can also compete on the compact-size front, with the additional advantage of coherence which can simplify the overall optical design. At this time, the fundamental limitation preventing integration of UV LDs into an aerosol sensor is the wavelength. Commercial nitride LDs operating at 410 nm lie beyond the absorption of key bio-fluorophores, although research-grade devices at 380 nm have shown promising performance. In this chapter we begin to investigate the application of the latter into a bio-aerosol system targeting NADH. To mitigate for the low output power in these devices, and as is expected from initial LDs at lower wavelengths, we propose a scheme to track an airborne particle with a moving laser spot. While employing a different method to track the particle, **Figure 6.1** illustrates the use of an acousto-optic modulator (AOM), this scheme is analogous to the UV LED array in many ways.

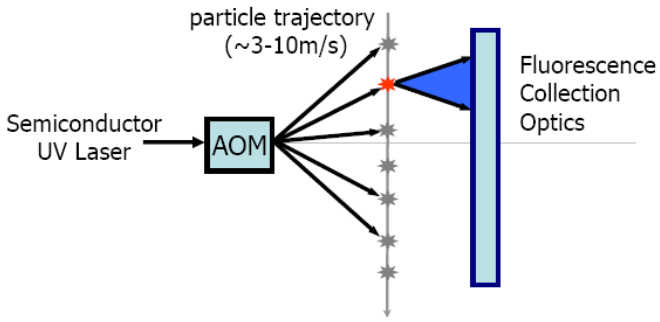

Figure 6.1 : Schematic illustration of particle tracking with an AOM.

6.1. UV LD scanner concept

Figure 6.2 is a schematic of the optical setup incorporating a UV LD and an AOM for particle tracking. The 380 nm LD used in these experiments is provided courtesy of PARC [1], and is capable of yielding CW output powers in excess of 10 mW when operated above threshold at nominally 120 mA. As is the case for emerging devices, the LD has a finite lifetime and thus care is taken to avoid unnecessary heating; it is mounted on the copper heat sink visible in **Figure 6.2 (b)** and kept a few degrees below room temperature using a thermoelectric cooler (TEC).

AOMs are used in telecommunications to modulate signals, as lossy elements in Q-switched lasers, and to deflect laser light. An AOM operates on the principle of diffraction of the incoming light wave with an acoustic wave set up in the crystal using a piezo-electric transducer. The diffraction angle (θ_B) depends on the wavelength of both the light (λ) and sound waves (Λ),

$$\theta_B \approx \frac{m\lambda}{2\Lambda},$$

and the efficiency, or fraction of incoming light diffracted, is dependent upon the intensity of the latter. The wavelength of the acoustic disturbance is adjusted by the driving frequency applied to the piezo-transducer, and thus a stationary input light beam can be scanned by continuously adjusting the drive frequency. The speed at which the beam can be deflected is fundamentally

limited by the time required for the acoustic wave to traverse the crystal. At acoustic velocities of approximately 0.62 mm/usec this corresponds to a few microseconds, which is sufficient for the aerosol speeds under study, and competes with alternative scanning techniques requiring mechanical movement. In these experiments an AOM with a UV-transparent TeO_2 crystal cut for 365 nm is used (Crystal Technology, AODF 4100-2). This instrument is equipped with an RF driver which accepts a tuning voltage to sweep the frequency centered around 100 MHz. The timing electronics to sequence the particle tracking is much the same as the LED array case with the exception that the AOM is supplied with a linear ramp in tuning voltage where the LED array was pulsed. The full range of deflection is approximately 2°, which corresponds to tracking 2mm of the particle trajectory. Following the collimating lens, a quarter-wave plate is used in order to adjust the polarization of the LD to match that yielding the highest deflection efficiency, and a slit is used after the AOM to block higher order deflected beams. Optical design for fluorescence collection is replicated from the LED case, although greater flexibility is imaginable given the beam directionality.

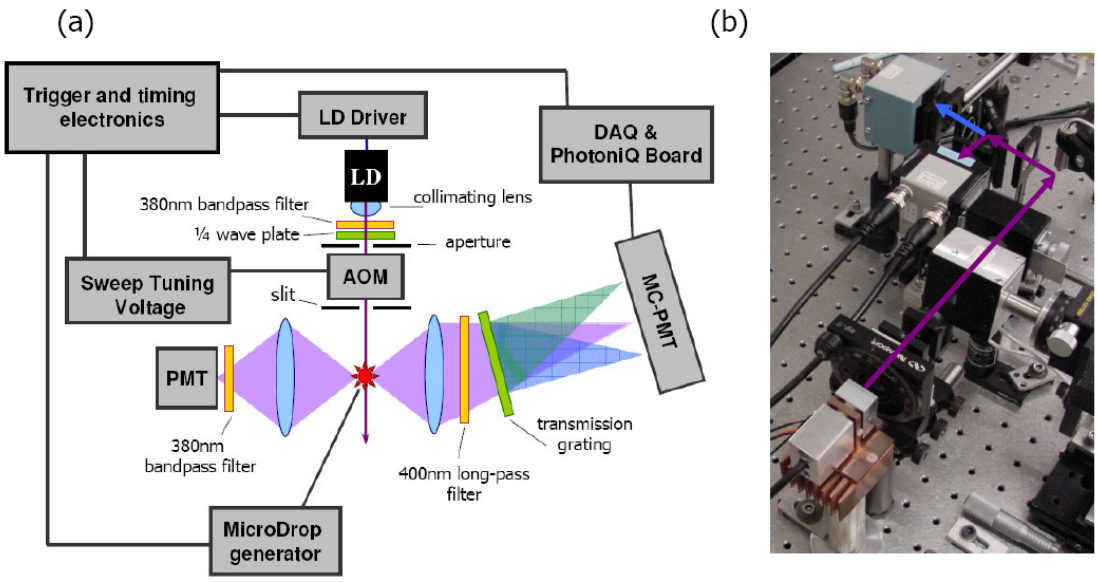

Figure 6.2 : Optical apparatus incorporating a UV LD.

6.2. Initial characterization with NADH

Figure 6.3 (a) contains filter-band fluorescence signals from single NADH-doped water droplets illuminated with a 380 nm LD which is supplied with current for only 1 msec while the particle flies by. Although 1 msec is essentially CW on the timescale of device heating, operating with a low duty cycle minimizes detrimental effects. The droop in fluorescence measured over 1 msec is attributed to several factors including a strong dependence of AOM efficiency on deflection angle and drop in LD output power with long illumination time. Another contribution is the non-linear dependence of the deflection angle on tuning voltage, which could be improved by providing a tailored voltage sweep in favor of the linear ramp used here. The F/S ratios in **Figure 6.3 (b)** suggest that the detection limit of this test system is below 0.005 wt % NADH (70 uMolar). Owing to the larger output power, this initial result compares favorably with the 340 nm LED-based system despite the reduction in absorption of NADH at the longer wavelength. The full real-time spectroscopic system is used to acquire single particle spectra as shown in **Figure 6.4** for 1 wt % NADH-doped particles.

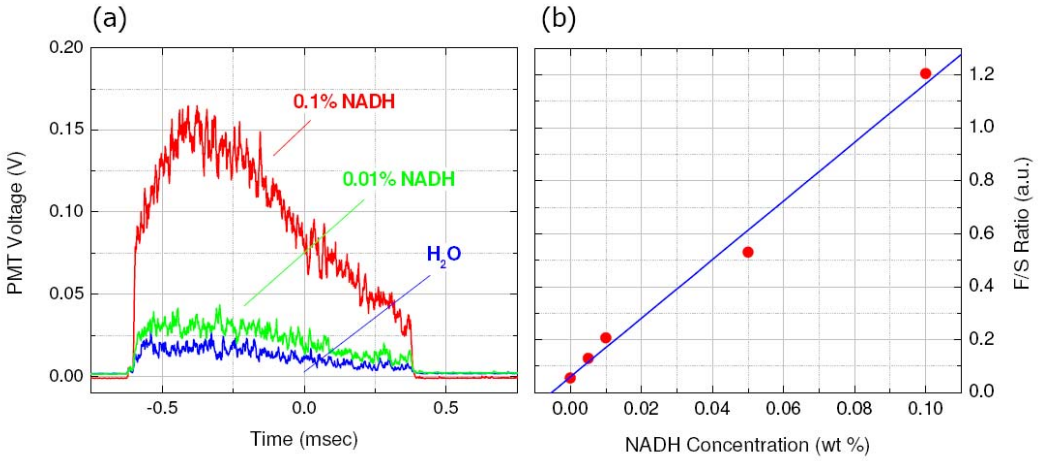

Figure 6.3 : Filter-based detection of NADH excited by a CW 380 nm LD.

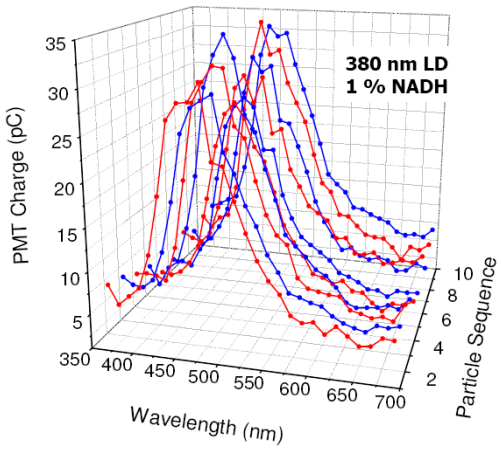

Figure 6.4 : Spectra from single NADH-doped particles.

Summary

With advances in epitaxial quality, and the possibility of AlN as a substrate with well-defined cleavage planes suitable for facet formation, LDs are expected to follow the same progress towards shorter wavelength as UV LEDs have commenced within the past few years. Optically-pumped laser diode structures at the key wavelength of 340 nm have been recently reported [2], and in this chapter we have demonstrated a system into which this material can be integrated once electrically-injectable devices are fabricated.

References

1. M. Kneissl, D. W. Treat, M. Teepe, N. Miyashita and N. M. Johnson. Appl. Phys. Lett., 2003. **82**(15): p. 2386-2388.

2. Y. He, Y.-K. Song, A. V. Nurmikko, J. Su, M. Gherasimova, G. Cui and J. Han. Appl. Phys. Lett., 2004. **84**(4): p. 463-465.

CHAPTER 7

CONCLUDING REMARKS

Recent interest in compact UV light emitters has produced advances in material quality and device performance from aluminum-rich alloys of the nitride semiconductor system. The epitaxial growth of device structures from this material poses remarkable challenges, and state-of-the-art in semiconductor UV light sources at wavelengths shorter than 350 nm is currently limited to LEDs. A portion of the work presented in this thesis involved the design and characterization of UV LED structures, with particular focus on sub-300 nm LEDs which have only been demonstrated within the last four years. Emphasis has been placed on the integration of early devices with modest efficiencies and output powers into a practical bio-sensing instrument.

In **Chapter 4**, the quality of AlGaInN and AlGaN-based materials was characterized by way of the performance of 340 nm and 290 nm LEDs respectively. A level of performance competitive with reports of UV LEDs in recent literature was achieved, although much room remains for improvement in material quality and the resulting device efficiency. To this end, we embarked on a preliminary investigation of 300 nm LEDs grown on AlN. Initial device results show evidence of improved electrical and optical characteristics, and motivate future work in this direction. With its numerous advantages over the more traditional sapphire, this native substrate has the potential to revolutionize the epitaxy of wide bandgap nitride semiconductors, and work in this direction is ongoing with the ultimate goal of creating a UV LD.

The application of UV LEDs to the field of bio-aerosol sensing was pursued in **Chapters 5** and **6**. A linear array of individually addressable UV LEDs was designed and implemented, and the capability of test devices to excite native fluorescence from bacterial spores was established. In order to fully capitalize on the reduction in size afforded by LEDs, effort was invested in re-engineering the remaining sensor components. Operation of a prototype system for physically sorting bio-aerosols based on fluorescence spectra excited using UV-LED arrays was demonstrated using test particles including the biofluorophores NADH and tryptophan. Improvement in the detection limit of this system will come from the development of algorithms to use real-time fluorescence spectra to discriminate bio-aerosols from background particles. Future work is anticipated in this area, however, through the need for more UV excitation power, sensor performance is ultimately linked to the material quality of high aluminum fraction nitrides, and is expected to show progress as this field matures. Along these lines, the groundwork has been laid for the eventual incorporation of a UV laser diode into a bio-sensing instrument.

The instrument developed through the course of this work has remarkable similarity to schemes employed in flow cytometry [1], a relationship that is worthy of future investigation. Another potential application of our UV LED array-based sensor is in a microfluidic environment for studying the kinetics of protein folding [2, 3], which also involves the native fluorescence from tryptophan. In conjunction with our demonstration of patterned LEDs for dynamic imaging of neural cells [4], these examples serve to illustrate the potential application space for UV LEDs and nitride LED arrays in general.

References

1. H. M. Davey and D. B. Kell. Microbiol. Rev., 1996. **60**(4): p. 641-696.

2. O. Bilsel, C. Kayatekin, L. A. Wallace and C. R. Matthews. Rev. Sci. Instrum., 2005. **76**(014302).

3. C. D. McGuinness, K. Sagoo, D. McLoskey and D. J. S. Birch. Appl. Phys. Lett., 2005. **86**(261911).

4. S. Venkataramani, K. Davitt, J. Zhang, H. Xu, Y.-K. Song, B. W. Connors and A. V. Nurmikko. IEEE J. Selected Topics in Quantum Electronics, 2005. **11**(4): p. 785-790.

APPENDIX A

GREEN LED ARRAYS FOR IMAGING PATTERNED NEURONS

A unique aspect of our approach of using UV LEDs in a bioaerosol warning sensor is tailoring of the LED emission pattern to suit the task, specifically into a linear array of individual elements. However, the general idea of modifying the LED geometry has a broader potential to enable the application of LEDs in many fields. In order to widen the scope of prospective applications, we extend our interest to include the smaller bandgap, high efficiency InGaN materials emitting in the blue and green. At these wavelengths, two-dimensional arrays of small aperture LEDs have been reported with matrix-addressable electrical access [1], and later applied for use in blue/green micro-displays [2]. Here we apply the light extraction and packaging procedures developed in **Chapter 5** to the fabrication of small 2-dimensional patterns of blue/green wavelength LEDs for the purpose of dynamic imaging of individual neurons *in vitro*.

Cultured neural cell platform

The details of cell culture and electrophysiology performed by Dr. S. Venkataramani are reported elsewhere [3]. Briefly, hippocampal neurons from embryonic rats are plated onto glass coverslips which have been periodically patterned with poly-L-lysine using the standard photolithographic lift-off technique described in **Chapter 4** in the context of device fabrication. Cells adhere preferentially to the poly-L-lysine surface and hence patterned arrays of neurons are cultivated over several days to weeks of regular feeding and storage in an environmentally

controlled incubator. Two major methods exist to probe the dynamic electrical activity of neural cells; the patch clamp technique, and voltage-sensitive molecular dye (VSD) imaging. The former provides direct electrical access to a single cell using a micrometer-sized pipette and is used both for delivering excitation by injection of a small current, and for measuring cell activity in the form of membrane (action) potentials. On the other hand, VSD imaging requires bathing the culture in a solution of fluorescent dye which adheres to the cell membrane. The fluorescence intensity (and spectrum) of the dye is dependent on the membrane potential [4], and changes sufficiently quickly so as to enable discrimination of action potentials which occur on the time scale of 1 msec. In this technique, the entire culture is normally illuminated with light matching the absorption of the dye and the fluorescence intensity is monitored with a CCD camera of sufficient spatial resolution. This optical method provides access to the dynamic interaction of a population of neurons, but traditionally requires the use of incoherent lamps or large frame lasers and a high-end CCD camera.

Experimental setup with green LED arrays

The VSD (Molecular Probes, di-8-ANEPPS) used in the experiments performed here exhibits the best signal-to-noise ratio under 530 nm illumination, hence green InGaN LEDs are employed as the fluorescence excitation source. Cell cultures are grown on square-grid patterns with center-to-center separations ranging from 100 to 250 um and a node size of 50 um which is slightly larger than the typical dimension of a cell body. LED arrays fabricated with a matching geometry for 1:1 imaging of the cell pattern are shown **Figure A.1**. Using the same procedure developed for UV LEDs in **Chapter 5**, the array is flip-chipped and mounted on a commercial DIP package to facilitate connection to a control circuit and mounting under the Nikon E600FN microscope. A pair of short focal-length aspheric lenses (f = 6 mm, $F\#$ 0.88) to focus the LED emission to the cells with a magnification of 1 is followed by an emission filter to block the

notorious long-wavelength tail. A custom mount was designed and machined to fix the LED assembly below the recording chamber in the position normally occupied by the microscope condenser, as shown in **Figure A.2**. We note that further reduction in size and complication of the experimental apparatus is achieved by integrating all of the excitation optics into a single package. **Figure A.2 (b)** contains images of blue LED arrays that incorporate a multilayer dielectric filter (10 pair SiO_2/HfO_2) deposited on the sapphire backside and a 2 mm diameter hyperhemispherical lens.

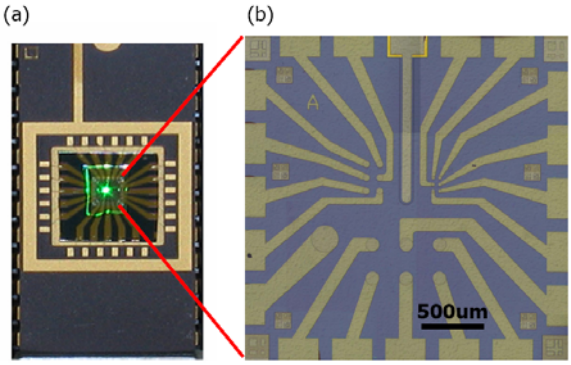

Figure A.1 : Green LED array package and aperture geometry.

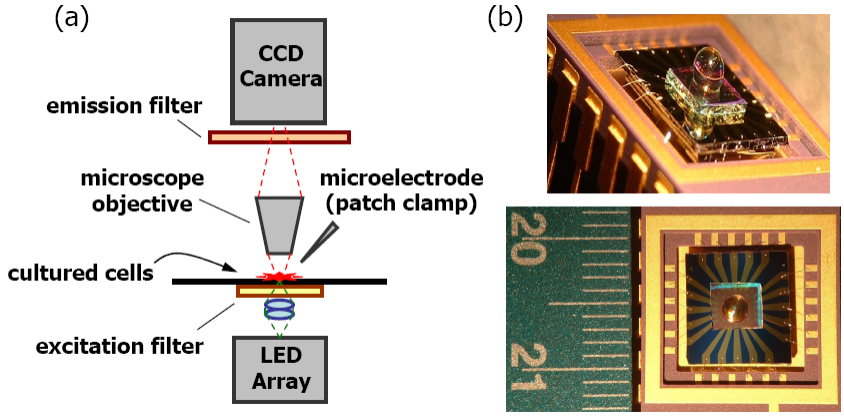

Figure A.2 : Experimental setup for imaging neurons.

Results

As a part of the experimental procedure, the LED array mount is fixed to a 3D micromanipulator and the LED pattern is aligned with the neural cells situated in the microscope recording chamber. **Figure A.3** contains a sequence of images illustrating the ability of an LED excitation source to selectively image a particular cell. Part **(a)** is a DIC (differential interference contrast) picture of two hippocampal cells in culture, and **(b)** is an image taken under illumination from an LED array with two 50 um diameter elements on. Part **(c)** shows fluorescence images of the same cells loaded with VSD and taken with one or both LEDs on at a time. This demonstrates the ability of spatiotemporally patterned LED photoexcitation to isolate individual neurons in culture and hence alleviate the need for a high-end imaging camera.

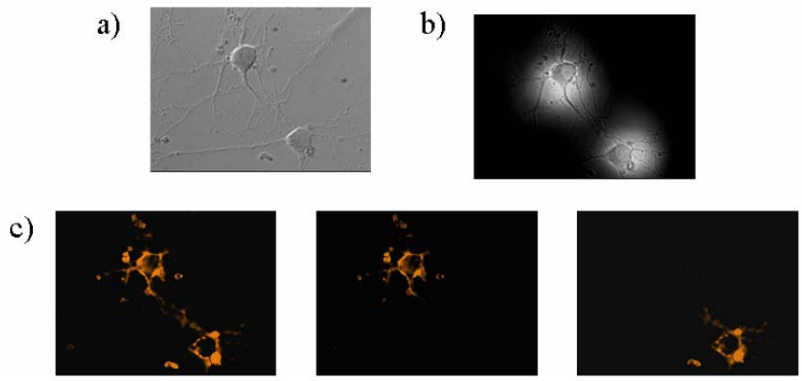

Figure A.3 : Selective imaging of patterned neurons with an LED array.

The change in fluorescence intensity (Δf/f) of the VSD measured using a NeuroCCD imaging camera (RedShirt Imaging) is shown in **Figure A.4**. The upper trace in part **(a)** shows the electrical signal measured via the patch-clamp microelectrode and the lower trace shows the optical signal under LED illumination of approximately 0.16 mW from a 50 um aperture powered by a low-noise current source. Part **(b)** highlights the area of the cell membrane over which the

fluorescence change is averaged to generate the optical signal. This preliminary result exhibits sufficient signal-to-noise to capture the optical indication of an action potential, and considerable improvements are expected with fine-tuning of the optical and electrical subsystems.

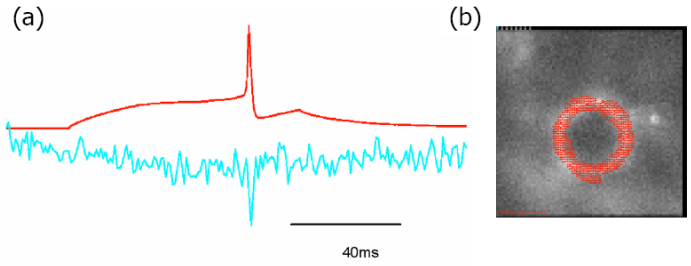

Figure A.4 : Electrical and optical signals from a neuron under LED excitation.

Summary

Thus, we have demonstrated the utility of patterned arrays of LEDs to reduce the complexity of existing instrumentation for dynamic imaging of hippocampal neurons. This represents a part of the longer-term mission to develop a new approach to dynamic imaging with the ultimate goal of investigating the complex routing of information within a population of neural cells. On a similarly expansive note, these experiments serve as an illustration of the flexibility of nitride LEDs and the fabrication techniques developed in this thesis to a broad range of applications.

References

1. I. Ozden, M. Diagne, A. V. Nurmikko, J. Han and T. Takeuchi. Phys. Stat. Sol. (a), 2001. **188**(1): p. 139-142.

2. H. W. Choi, C. W. Jeon and M. D. Dawson. IEEE Electron. Device Lett., 2004. **25**(5): p. 277-279.

3. S. Venkataramani, K. Davitt, J. Zhang, H. Xu, Y.-K. Song, B. W. Connors and A. V. Nurmikko. IEEE J. Selected Topics in Quantum Electronics, 2005. **11**(4): p. 785-790.

4. L. M. Loew. J. Biochem. Biophys. Meth., 1982. **6**: p. 243-260.

APPENDIX B

32-ELEMENT LINEAR LED-ARRAY DRIVER CIRCUIT

In the bio-aerosol warning system developed in this thesis, the elements of an array of LEDs are pulsed in rapid sequence so as to follow a particle during its time of flight. The circuit illustrated in **Figure B.1** accomplishes this for a linear array of UV LEDs connected by a common cathode. The components include a flip-flop, a pair of counters and decoders, and power MOSFETs which can tolerate the relatively high LED bias voltage. The pulse width is set by the *clock* input and the sequence is initiated at the rising edge of the *trigger* input. This simple LED driver is later replaced by custom electronics from Vtech Engineering Corp.

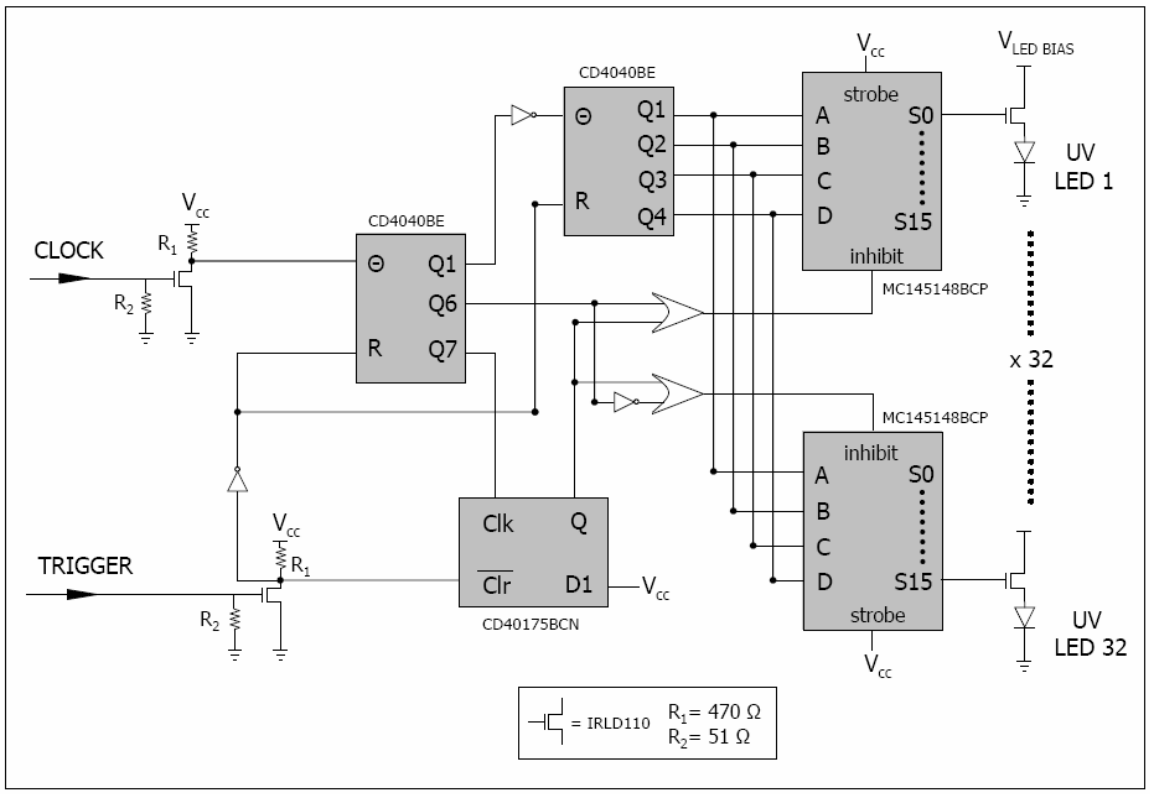

Figure B.1 : Circuit for sequentially firing a 32-element linear array of UV LEDs.